Molecular Dynamics Simulations of Surfactants' Adsorption in Emulsion Polymerizations and of CO_2 Capture by Graphene-Polymer Composites

Giulia Magi Meconi

Supervisor

Prof. Ronen Zangi

Theory and Simulations Group

University of the Basque Country (UPV/EHU)

Donostia-San Sebastiàn

2019

To my parents

Contents

Chapter I

Introduction and objectives

Contents

I.1 Adsorption

Numerous physical, chemical and biological processes take place at the boundary between two phases, while others start at that interface. The change in concentration of a given substance at the interface as compared with the neighbouring phases is referred to as adsorption. The adsorption is a surface phenomenon, which can be defined as either a spontaneous accumulation of a substance (molecules or atoms) at surface or partitioning of chemical species between bulk phase and an interface. The nature of the interface may be solid-liquid, gas-liquid, liquid-liquid or solid-gas. The phenomenon of adsorption is involved in such important practical applications as catalysis, water purification, environmental protection, and materials preparation. The major development of adsorption processes on a large industrial scale deals mainly with the solid-gas [1] and solid-liquid interfaces, [2] but in various laboratory separation techniques all types of interfaces are applied.

Adsorption is a consequence of surface energy. The surface represents the outer or the topmost boundary of a solid (or liquid) phase, where the bulk properties are no longer sufficient to describe the system's properties; in fact the interaction forces for the bulk phase become asymmetric. Due to the disruption (or unsaturation) of intermolecular bonds, the molecules located at an interface have more energy compared with the molecules in the bulk of the materials; thus surface is intrinsically less energetically favourable than the bulk, resulting in a peculiar reactivity. Surface energy is defined as the excess energy at the surface of a material compared to the bulk, or it is the work required to build an area of a particular surface. It is frequently expressed in the S.I. units mN/m. The term surface energy is commonly applied for dealing with the solid surface. In case of liquid surface it is more usual to use the idea of surface

tension. Although defined as a free energy per unit area, surface tension may also be thought of as a force acting normal to the interface per unit length (mN/m). Due to the cohesive forces, a molecule in the bulk is pulled equally in every direction by the neighbouring liquid molecules, resulting in a net force of zero. The molecules at the surface do not have the same molecules on all sides of them, so there is a net inward cohesive force, which tries to minimize the surface area (Figure I.1). For liquid/liquid systems the term used to describe these interfacial forces is "interfacial tension". For liquid/gas systems the term commonly used is "surface tension".

As a consequence, the molecules on the surface become capable of adsorbing foreign atoms or molecules in order to minimize the surface free energy or to reduce the net inward force (surface/interfacial tension).

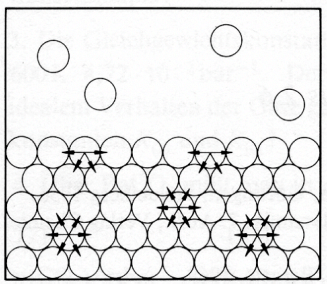

Figure I.1: Schematic representation of the interaction forces of molecules in a liquid.

I.2 Adsorption at liquid interfaces

Different factors at liquid surface may cause changes in the composition of the interface layer [3]. Substances may accumulate at the surface characterizing the phenomena of adsorption. This induces changes in the surface (or interfacial) tension and colloid stability. The adsorption of molecules of liquid phase at an interface occurs when this liquid phase is in contact with other immiscible phases that may be gas, liquid, or solid. [4]

The adsorption phenomena in the aqueous medium may be caused by the hydrophobic effect, which is the tendency of non-polar substances to aggregate in an aqueous solution and exclude water molecules. [5] The term hydrophobic literally means "water-fearing", and it describes the segregation of water and non-polar substances minimizing their contact area. Thus, the driving force of these interactions is the minimization of total interfacial free energy. The hydrophobic effect depends importantly on the length-scale of the solute. Water molecules near small hydrophobic solutes do not sacrifice hydrogen bonds, but adopt orientations that allow hydrogen bonding patterns to go around (or accommodate) the solute. This strain on the hydrogen bonding network is reflected in a large negative entropy ($\Delta S < 0$). The extent to which bonds are broken at any instant is similar to that in the pure liquid.

In contrast, hydrogen bonds are broken in the hydration of large solutes, over areas larger than $1nm^2$, resulting in a negative enthalpic penalty ($\Delta H < 0$). A fraction of hydrogen bond, per water molecule, is lost near the hydrophobic surface, comparing with the bulk. As a results, water tends to move away from the large solute and forms an interface around it, making the process not spontaneous in terms of free energy of the system. This energetically unfavorable scenario, to which a large interfacial tension is associated, drives the

minimization of the contact area. By aggregating together, non-polar solutes reduce the surface area exposed to water and minimize their disruptive effect (hydrophobic interaction). The aggregation is accomplished by brownian motion of the solute and solvent, once hydrophobic molecules are aggregated, it is unfavorable for them to be dissolved again. The presence of hydrophilic groups in the molecules of solute can prevent the phase separation by maintaining the hydrophobic groups in water through formation of hydrogen bonds with water molecules.

Surfactant, whose term is an abbreviation for "surface active agent", is therefore a substance that at low concentrations adsorbs, thereby changing the amount of work required to expand that interface. In particular surfactants can significantly reduce interfacial (surface) tension due to their dual chemical nature. The ability of the surface active agents of altering the physical proprieties of interfaces plays a significant role in several practical applications and products as emulsification, wetting, coating, foaming, inhibitor corrosion, and biological industrial purposes.

I.2.1 Surfactants

Surfactants are amphiphilic compounds, meaning they consist of at least two parts, one which is soluble in water (hydrophilic part) and one which is insoluble (hydrophobic part). The hydrophilic part is referred to as the head group and the hydrophobic part as the tail (see Figure I.2).

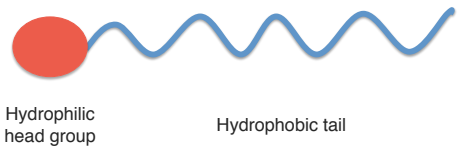

Figure I.2: Schematic illustration of a surfactant.

The hydrophobic part of a surfactant may be branched or linear; it is normally a hydrocarbon (alkyl or alkylaryl) but also may be polydimethylsiloxane or a fluorocarbon. The polar head group is usually, but not always, attached at one end of the alkyl chain. The degree of chain branching, the position of the polar group and the length of the chain are parameters of importance for the physicochemical properties of the surfactant.

The primary classification of surfactants is made on the basis of the charge of the polar head group, which may be **ionic**, **nonionic** and **zwitterionic**. The head of **ionic** surfactant carries a net positive, or negative charge. If the charge is negative, the surfactant is more specifically called **anionic**; if the charge is positive, it is called **cationic**. A nonionic surfactant has no charged groups in its head. For nonionic surfactants the size of the head group can be varied at will; for the ionics, the size is more or less a fixed parameter. **Zwitterionic** active agents contain two charged groups of different sign; the positive charge is almost invariably ammonium, the source of negative charge may vary, although

carboxylate is by far the most common.

Most **ionic** surfactants are monovalent. Carboxylate, sulfate, sulfonate and phosphate are the polar groups found in anionic surfactants. This class of surfactants is used in greater volume than any other surfactants. One main reason for their popularity is the ease and low cost of manufacture. Figure I.3 shows the structure of the most common surfactant types which belong to this class. They include alkylbenzene sulfonates (detergents), dialkyl sulfoccinate (wetting agent), carboxylate salts (soaps) and alkyl sulfates, such as ammonium lauryl sulfate, sodium lauryl sulfate (sodium dodecyl sulfate or SDS) and the related sodium lauryl ether sulfate (SLES), and sodium myreth sulfate.

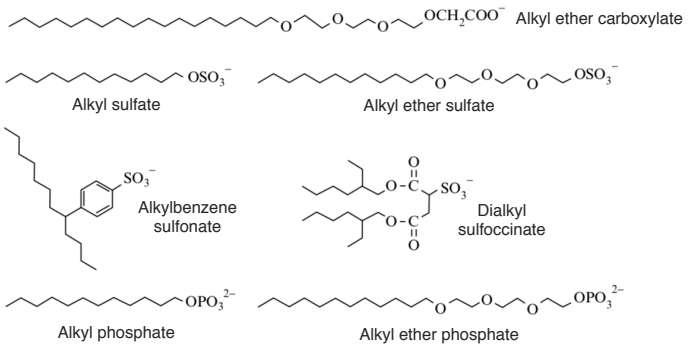

Figure I.3: Structures of some representative anaionic surfactants.

The majority of cataionic surfactants are based on the nitrogen atom carrying the cationic charge; amine salts and quaternary ammonium compounds are the most common. These surfactants are in general more expensive than anionics due to the hydrogenation reaction required during their synthesis. Therefore they are used only in cases in which there is no cheaper substitute, such as bactericide and as positively charged substance which is able to adsorbed on nega-

tively charged substrates to produce antistatic and hydrophobic effect, often of great commercial importance as corrosion inhibition. For the ionic surfactants the choice of counterion plays a role in the physicochemical properties. The counterions most commonly used for the anionic surfactants are sodium, potassium, ammonium, calcium and various protonated alkyl amines. The counterion of cationic surfactants is usually a halide or methyl sulfate.

Nonionic surfactant don't ionize in aqueous solution, because their hydrophilic group is of a non dissociable type, such as alcohol, phenol, ether, ester, or amide. As a consequence, they are excellent solvents and have an high chemical stability. They are not sensitive to hard water as ionic surfactants. In the vast majority of non-ionics (Figure I.4), the polar group is a polyethylene oxide (PEO) chain, obtained by the polycondensation of ethylene oxide.

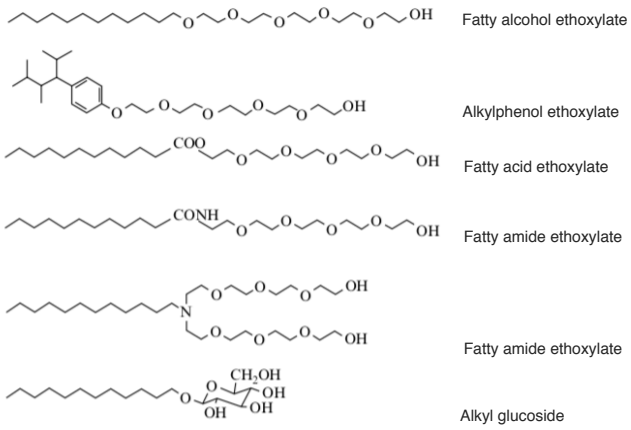

Figure I.4: Structures of some representative nonionic surfactants.

Surfactant aggregation and adsorption at interfaces

Due to their dual nature, surfactants dissolved in aqueous phase are distinguished by the ability to adsorb at the interfaces (surfaces), and to form self-assembly structures (micelles) in aqueous solutions. Both adsorption and aggregation phenomena are associated with a significant reduction of free energy in the system and result from the hydrophobic effect. The hydrogen bonding structure of the water molecules is disrupted by the non-polar groups in dissolved amphiphilic molecules. The hydration waters are able to remain tetrahedrally coordinated forming surrounding structures around the tails of surfactants (hydrophobic effect). This organization apparently increases the free energy of the system. Less work is required to bring a surfactant molecule to the interface (or surface) than a water molecule, so that migration of the amphipilies to the interface is a spontaneous process, and their accumulation results in a decrease of the interfacial (surface) tension. According to this phenomena, the orientation of hydrophobic groups is likely to reduce the water contact, and is determined by the nature of the interface.

As mentioned in the Section I.2, the mixing of large hydrophobes and water molecules is not a spontaneous process, therefore is an endoergonic reaction ($\Delta G > 0$), nevertheless exothermic ($\Delta H < 0$) because water molecules are not able to participate in four hydrogen bonds like their bulk counterparts. Therefore, the accumulation of surfactants is a spontaneous process, which is accompanied by a reduction of the interfacial free energy ($\Delta G < 0$), since the electrostatic interactions and HB interactions with the hydrophilic head groups of the amphiphiles, allow the water molecules to maintain their tetrahedral coordination with the surrounding. When surfactants self-assemble to form micelles in aqueous solutions, the hydrophobic parts of the surfactants are concentrated

towards the center of the aggregate while the hydrophilic parts reside on the surface (Figure I.5).

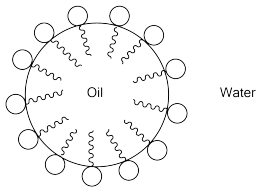

Figure I.5: Schematic representation of spherical surfactant micelle.

As previous mentioned, micelle formation, or micellization, is an alternative mechanism to adsorption at the interfaces for removing hydrophobic groups from contact with water, thereby reducing the free energy of the system. The specific concentration at which micellization occurs is known as the critical micelle concentration (CMC). Below the CMC, surfactants are monomers in solution and interfacial tension follows the Gibbs's isotherm which will be discuss further in this Chapter (see Equation I.5). Above the CMC, the surface tension and the free surfactant concentration become constant because all the additional surfactant molecules aggregate to form the micelle [6]. The size and shape of micelles are governed by the geometry of both hydrophilic and hydrophobic groups as well as the interaction between surfactant molecules [7].

I.2.2 Emulsion

An emulsion is a fluid colloidal system in which of one liquid is dispersed in another liquid. The two liquids are obviously immiscible. Almost all emulsions contain water as one phase and an organic liquid as the other phase. The organic phase is normally referred to as the 'oil' but by no means it needs to be an oil in the normal meaning of the word. Non-aqueous emulsions also exist, such as emulsions of fluorocarbons in hydrocarbon.

There are two main types of emulsions: oil-in-water (o/w) and water-in-oil (w/o). Oil-in-water emulsions are by far the most important and common examples are paints, glues, bitumen emulsions, agrochemical formulations, etc. Spreads (margarines) are well-known examples of w/o emulsions. There also exist so-called double emulsions which may be w/o/w or o/w/o. Such systems are of interest for drug delivery.

The droplets in an emulsions are referred to as the dispersed phase, while the surrounding liquid is the continuous phase. According the size of their droplets, one can distinguish three types of emulsions: [8] (1) macroemulsions, the most well-known type, with droplets $> 400nm$; (2) miniemulsions, with droplets between 100 and 400 nm; (3) microemulsions, with droplets $< 100nm$.

Emulsions are thermodynamically unstable systems and, thus, do not tend to form spontaneously. In order to form a colloidal dispersion, it is required to bring energy into the system through shaking, stirring, homogenizing, [9] or exposure to power ultrasound. [10]

During the emulsification, oil bulk is broken up into small droplets, which try to reduce their free energy by minimizing interfacial area by holding together into one big droplet, due to the interfacial forces. These are opposing to the "distruptive forces", generated by homogenizers.

Droplets are constantly moving (Brownian motion) and the frequency of collision is very high due to the agitation. These collisions, governed by Wan der Waals-London attractive forces, may lead to aggregation, increasing then the droplets size. [11]

The term 'emulsion stability' refers to the ability of an emulsion to keep its proprieties unchanged over a certain period of time. As metion before, emulsions are metastable systems because they are thermodynamically unstable and kinetically stable: that phenomena, responsible for thermodynamically instability, can take place over a long period a time due to the presence of an adsorbed layer at o/w interface which may be electrostatic in nature, or steric.

Thus, the physical degradation of emulsion is prevented by the adsorption of emulsifiers at the oil-water interface. There are many different emulsifiers; surface active agents (surfactants) are the most common. They have two main roles to play: lower the interfacial tension, facilitating droplets break-up, and prevent droplet contact. [9, 12, 13] Due to its amphiphilic character, surfactant has its hydrophilic moiety in water and its hydrophobic moiety in oil, reducing the tension across the interface.

The concentration of surfactant in the system lowers the interfacial tension, affecting the final droplets size and their trend to aggregate. [14] Consider two droplets insufficiently covered by surfactant, moving toward each other. During their approach, more surfactants get adsorbed at the interface of the two droplets. However, the amount of surfactant available for adsorption is the lowest where the film between the droplets is thinnest. The coverage of the droplets is then not uniform; less surfactant molecules are present at the region of the interface where the droplets are closest. This leads to an interfacial tension gradient, which is the highest where the film is the thinnest. The gradient causes surfactants to move at the interface towards the site of lowest surfactant

coverage. This determines the diffusion of water toward the highest interfacial tension which drives the droplets away from each other.

Moreover, surfactants' ability to stabilize emulsions depends on their physical proprieties. It is common practice to distinguish two different modes of emulsion stabilization, although these are often combined: electrostatic and steric.

Electrostatic stabilization by **ionic** (in particular anionic) surfactants is very common. Electrostatic stabilization is based on the repulsive interaction that results when the diffuse double layers around the particles start to overlap. [15, 16]

The **steric** stabilization becomes operative when the interfacial layer consists of **nonionic** emulsifiers. [17] When the layers of two interacting particle overlap, the concentration of the macromolecule (or chains) increases in the overlap region. The increase of the local chain concentration causes the diffusion of the solvent from the continuous phase to the overlapped region. When molecules of the solvent enter the overlapped region, the local chain concentration decreases and consequently the droplets separate from one other. [18]

I.2.3 Surface excess and Gibbs adsorption isotherm

A common thermodynamic treatment of the variation of the surface tension with the adsorption of surfactants at the interface has been derived by Gibbs. [19] An important approximation associated with this Gibbs adsorption equation is the "exact" location of the interface.

Consider two phases (α and β), the surface (interfacial) layer is located in between the phase α and phase β with a thickness τ.

In the system is added n_i moles of the component i (or surfactant). The adsorption of the component at the phase boundary results to a different concentration in the interfacial layer, because it gradually varies from the bulk concentration of α to the bulk concentration of β over the distance τ. In the bulk regions of α and β the concentration of the component is constant.

The adsorbate density and the composition profile within the interface layer cannot be measures by nowadays technology and the amounts of surfactant adsorbed is not a meaningful experimental variable.

To solve this problem Gibbs introduced a mathematical plane (dividing plane), with zero thickness, so that the proprieties of α and β apply right up to that plane positioned at some specific value . The position of the dividing surface is arbitrarily taken as being at the point where there is no net adsorption of solvent (Figure I.6).

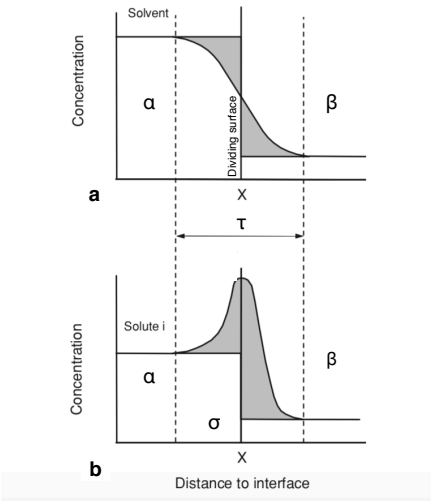

Figure I.6: Schematic representation of the concentration profile of the solvent (a) and solute (b) as a function of the distance.

The surface excess amount n_i^σ of the component i, which may be positive or negative, is defined as the excess of amount of this component present in the system at the surface plane which is given by the difference of the ammount of the component (n_i) in the system and the amount ($n_i(\alpha) + n_i(\beta)$) contained in the two phases inside the interface layer of volume V and divided by the area of the dividing surface (A):

$$\Gamma_i^\sigma = \frac{n_i^\sigma}{A} \quad \text{with} \quad n_i^\sigma = n_i - [n_i(\alpha) + n_i(\beta)] \tag{I.1}$$

The Gibbs adsorption isotherm is a thermodynamic relationship between the variation of interfacial (or surface) tension, γ, with the surface excess concentration of the adsorbed species (moles per unit area).

At the equilibrium the Gibbs free energy $dG^\sigma = 0$ and the Gibbs-Deuhem equa-

tion [20] becomes

$$dG^{\sigma} = -S^{\sigma}dT + Ad\gamma + \sum n_i^{\sigma} d\mu_i = 0 \tag{I.2}$$

μ_i is the chemical potential of the component i. At constant temperature

$$Ad\gamma = -\sum n_i^{\sigma} d\mu_i \tag{I.3}$$

or

$$d\gamma = -\sum \frac{n_i^{\sigma}}{A} d\mu_i = -\sum \Gamma_i^{\sigma} d\mu_i \tag{I.4}$$

Therefore the excess concentration of the adsorbed species is defined as:

$$-\Gamma_i^{\sigma} = \frac{d\gamma}{d\mu_i} \tag{I.5}$$

According to this Equation I.5 for a system involving a solvent and a solute, there is an excess surface concentration of solute if the solute decreases the surface tension and a deficient surface concentration of solute if the solute increases the surface tension. Beside the Gibbs equation, other equations are also used to relate the surfactant (or solute) concentration at interfacial tension and surfactant (or solute) and surfactant equilibrium in the liquid phase. Langmuir isotherm [21] is the most popular model used to quantify the adsorption of substances at solid-liquid phase. The isotherm describes an equilibrium relation between the quantity of the adsorbed material and the concentration in the bulk fluid phase at constant temperature. This model will be discuss further in the Section I.3.1 of this Chapter.

I.2.4 Emulsion polymerization

Water-borne polymer dispersions are polymer particles dispersed in an aqueous medium. These dispersions are commonly synthesized by emulsion polymerization yielding versatile products called latexes. These solvent-free polymer latexes are environmentally friendly fulfilling the increasingly restrictive governmental regulations. There is a wide variety of water-borne polymeric dispersions that are mainly used as paints, coatings and adhesives. [22] They are also used in a broad range of fields such as inks, carpet backing, non-woven fabrics, leather treatment, foam mattresses, drug delivery systems, medical assay kits and other biomedical and pharmaceutical applications [23]. In addition, latexes are also used as impact modifiers in plastic matrices, [24] as additives [25] and as rheological modifiers. [26] By 2016, plastics had a worldwide annual production of 335 million tones, [27] and in a wide variety of applications are substituting other materials such as metal and wood. Waterborne dispersed polymers represent about 10% of worldwide polymer production. [28]

As mention above, emulsion polymerization (EP) is the leading technique to produce such kind of materials. The EP follows the mechanism proposed by W.D. Harkins [29] in 1947 which is schematically represented in the Figure I.7.

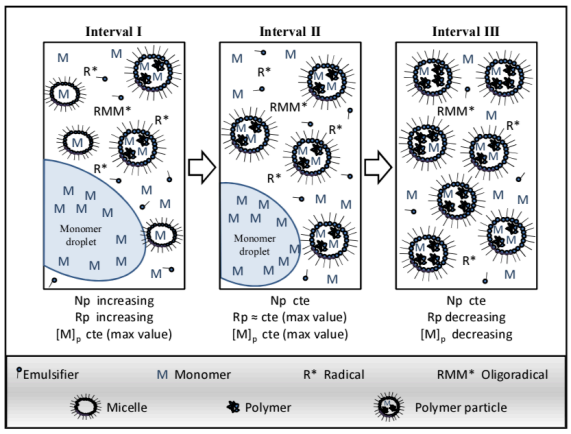

Figure I.7: Schematic representation of emulsion polymerization mechanism by Harkins.

According to this theory, batch EP is divided into three intervals, comprising a particle nucleation stage (**interval I**) and two particle growth stages (**intervals II and III**).

At the beggining of the **interval I** the emulsion polymerization systems consist of monomer (oil phase), emulsifier, initiator and, if necessary, modifiers. Since monomers, are only slightly soluble in water, they are partitioned between large dispersion of droplets stabilized by surfactants, micelles containing small amounts of monomer and free dispersed monomers in continuous phase. [8] Surfactants form micelles and adsorb on the surface of monomer droplets beyond the CMC. The micelles are in a dynamic equilibrium with the dissolved emulsifier molecules.

Free-radical initiators are water-soluble and can be produced via thermal decomposition, redox reactions, or by gamma radiation, depending on the type of latex being synthesized and hence the reaction temperature. As the initiator decomposes, the radicals formed react with monomer dissolved in aqueous phase forming oligoradicals. In the Harkins model of **micellar (or heterogeneous)**

nucleation, [29] the insoluble oligoradicals enter into the micelles containing dissolved monomer and immediately begin to polymerize and converts the micelle into actively growing latex particle.The entry of radicals into the micelles is more likely if the total area of the micelles is about three orders of magnitude greater than that of the droplets. During the nucleation, the monomer that is consumed in the polymer particle, is replaced by the monomer that diffuses from the monomer droplets. Consequently, the size of the polymer particle increases and the size of monomer droplets decreases. All the micelles that did not encounter a radical during the earlier stage of conversion disappear, losing their monomer and surfactant to growing the particles.The nucleation continues until all of the micelles are consumed. The disappearance of micelles is considered to be the end of the nucleation and marks the end of Interval I.

In parallel, new polymer particles can also be formed by **homogenous nucleation** [30] which occurs when the initiator does not enter a micelle but rather initiates polymerization within the aqueous medium when an initiator radical adds to a monomer. The radical then propagates in the aqueous phase until the chain reaches a critical length where the oligomer is no longer soluble in water. At this point, the chain is thermodynamically unstable and collapses on itself or onto dead oligomers found in the aqueous phase to form latex particles. Simultaneously, surfactant molecules may desorbed from the existing particles (formed by micellar nucleation) and adsorb on the surface of the new particles to impart stability by lowering the interfacial energy. If surfactants are absent, or are not fast enough to adsorb onto the surface of the growing latex particles, then some coagulation may occur. [8, 31–33] The kinetics of the surfactants desorption is critical for the stabilization of the newly formed particles. [34]

If we can neglect homogenous nucleation, the number of polymer particles will ideally remain fixed during intervals II and III. In the **interval II**, the system is

composed of monomer droplets and polymer particles.The monomer consumed by polymerization in the polymer particles is replaced by monomer that diffuses from the monomer droplets through the aqueous phase. In the presence of monomer droplets, the concentration of the monomer in the polymer particles reaches a maximum value and remains constant. The transport of reactants with low water solubility from monomer droplets to polymer particles may be diffusionally limited. Stage II terminates when all monomer droplets have been consumed. [8, 31–33]

In the **Intervall III**, only polymer particles exist. During this stage, the concentration of monomer in polymer particles continues to decrease as conversion increases. A polymer colloid will include a number of polymer chains within the particle that can be arranged in a crystalline, amorphous, rubbery or glassy state. Monomer is also retained in the particle and is the solvent of the particles. Particle size is constant by this stage. [8, 31–33]

I.2.5 Role of surfactants in emulsion polymerization

Surfactant (also refered as emulsier or stabilizer) is a key component of the formulation of polymerization in dispersed media. [22, 35–37] The surfactants useful for emulsion polymerization should meet the following requirements:

- have a specific structure with polar and no-polar groups;
- be more soluble in aqueous phase so as to be readily available for adsorption on the droplets/particle surface;
- adsorb strongly and not be easily displaced when two droplets/particles collide;
- reduce the interfacial tension;

- stabilize the colloidal dispersion by providing repulsive electrostatic and/or steric interactions which prevent aggregation;
- work in small concentration;
- be relatively inexpensive, non-toxic and safe to handle.

A wide variety of commercial surfactants fulfils these requirements. It must be stressed that the role of emulsifier is crucial since it facilitates the formation of monomer droplets of the initial emulsion, contributes decisively in nucleation process and imparts colloidal stability to polymer particles in the final latex. [38] As it was discussed in the previous part of this chapter, the chemical identity of the surfactant head group, which provides colloidal stability, predominantly determines the surfactant properties and its classification. The most commonly used surfactant in emulsion polymerization can be classified in two groups; on the one hand ionic surfactant such as sodium dodecyl sulfate (SDS), and on the other nonionic surfactants, most of which are fatty alcohol ethoxylates.

While significant steps have been made in the fundamental understanding of this process and its use in producing high quality materials, the underlying formulation, consisting of water, oil soluble monomer(s), initiator and surfactant remains the same as that applied 70 years ago. [29] The presence of surfactant is often considered a necessary evil in that it tends to affect negatively the physical performance of the final polymer and, its use must therefore be carefully regulated. For example, in adhesive films cast from polymer dispersions the surfactant tends to migrate towards to the polymer–air interface, resulting in increased water sensitivity and poor substrate adhesion. [39]

Nevertheless, its presence in the formulation is vital in order to prevent particle aggregation and coagulation in the reactor, and also, plays a defining role in the kinetics of particle nucleation during the polymerization process heavily affect-

ing the rate of polymerization. [40, 41] Despite the importance of surfactants in the emulsion polymerization process, they are still largely employed based on empirical observations of their behavior.

Ionic surfactants are known to nucleate particle very efficiently and stabilize the latex via electrostatic repulsion mechanism. However, latexes stabilized with this type of emulsifiers are often unstable upon the addition of electrolytes and in freeze-thaw cycles. Furthermore, these emulsifier have limited stabilizing effectiveness at the polymer dispersion and their films present high water sensitivity. Conversely, **nonionic** surfactants provide good colloidal stability with regards to high ionic strength media and freeze-thaw cycles. However, they are less efficient than ionic surfactants in particle nucleation because of their slow desorption. [34]

Therefore, in order to optimize the properties of the surfactant in both the reactor and in the final product it is common to use a mixture of ionic and nonionic surfactants.

Moreover, the nucleation behavior in emulsion polymerization using ionic surfactants is generally well described by the theory of Smith and Ewart, [42] the particle nucleation behavior of nonionic surfactants shows substantial deviations from this fundamental work and the origin of these differences has been scarcely explored.

Piirma and coworkers were among the first to undertake a comprehensive study of emulsion polymerization in the presence of nonionic surfactants. [43] Using the emulsifier Emulphogene BC-840 (with a 13 carbon hydrophobic chain and 15 ethylene oxide units) in the emulsion polymerization of styrene, they observed two distinct rate regimes in the time-conversion plot as well as bimodal molecular weight distribution and bimodal particle size distribution.

Later, these authors demonstrated experimental evidence to suggest that the

cause of the bimodality was a change in the nature of the emulsion. They proposed that in the early stages of the reaction a water-in-oil emulsion was formed and a large fraction of the emulsifier was present in the monomer phase. As the amount on monomer decreased a phase inversion occurred and an oil in water emulsion was formed which marked the onset of the second rate regime and the generation of a crop of new particles. [44]

Using Triton X-405 (with an octyl phenyl hydrophobic chain and 40 ethylene oxide units) as nonionic surfactant in the emulsion polymerization of styrene, Özdeğer et al. observed similar experimental results of two kinetic regimes and a bimodal particle size distribution, but offered a different explanation for the underlying cause for this phenomenon. [45]

They proposed that the surfactant partitioned/absorbed into the organic phase and attributed the second nucleation period to the release of surfactant from monomer droplets as the reaction progressed. Based on results with varying concentrations of surfactant, it was suggested that the latest secondary nucleation occurred at the point at which monomer droplets disappeared ($\sim$ 40% conversion in the emulsion polymerization of styrene), thus assuming no absorption of the surfactant into the polymer particles.

Later, Okubo and coworkers showed that absorption of the surfactant into polymer particles is often of great importance, even at high conversion, [46] and have used this advantageously in the synthesis of hollow particles, which can form as a result of surfactant induced absorption of water into polymer particles. [47, 48]

I.3 Adsorption at solid interfaces

Adsorption on solid surface is the phenomenon of solute(s) in a bulk fluid phase attaching onto an interface or surface. Adsorption can be classified as gas adsorption and liquid adsorption based on the initial state of the solute(s). The solute in the adsorbed state is defined as the 'adsorbate', but in the bulk, before being adsorbed, is called the 'adsorptive'. The 'adsorbent' is the solid surface on which the adsorption occurs. Desorption is the opposite mechanism of adsorption. The penetration by the adsorbate molecules into the bulk solid (or liquid) phase is defined as 'absorption'. [49]

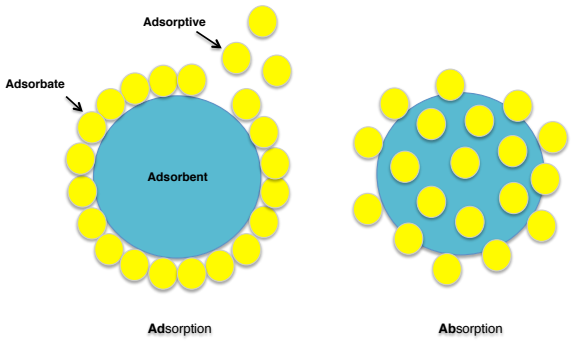

Figure I.8: Schematic representation of adsorption and absorption.

How do molecules adsorbed? Adsorption is governed by either physical or chemical forces. These forces depend on the nature of both adsorbent and adsorptive. They are distinguished in: (i) van der Waals/London dispersion forces; (ii) H–bonding interactions; (iii) chemical (covalent) forces which lead to the formation of a true chemical bond between the adsorbate and surface atoms. In the first two cases the process is classified as physical adsorption (**physisorption**), in the latter case chemical adsorption (**chemisorption**).

I.3.1 Adsorption isotherms

It is convenient to consider the adsorption as chemical reaction or surface reaction. That is,

$$A_g + S \underset{k_{des}}{\overset{k_{ads}}{\rightleftharpoons}} AS_{ads} \tag{I.6}$$

where A_g is the gas molecule and S is the adsorption site. The equation I.6 indicates that the adsorption process is reversible: k_{ads} and k_{des} are the adsorption and desorption rate constants. It is the nature of reversibility that made adsorption an effective separation technique for liquids and gases. The Gibbs free energy for the adsorption process is given by

$$\Delta G = \Delta H - T\Delta S \tag{I.7}$$

where ΔH is the enthalpy change due to adsorption of the molecule on the solid surface or heat of adsorption, ΔS is the entropy change from the the bulk phase (more random) to the adsorbed phase (more orderly), T is the temperature, and ΔG is the Gibbs free energy change due to adsorption. For the adsorption to occur, $\Delta G < 0$, therefore $\Delta H = \Delta G + T\Delta S < 0$ or the adsorption is exothermic. This condition holds because $\Delta S < 0$ for the adsorption process if the adsorption does not involve the breaking apart of the adsorbate molecule, as opposes to that in dissociative adsorption. The decrease in entropy is because of the change from a disorderly state (in fluid state) to an ordery state ("fixed" on the interface).

The adsorption isotherm is defined as the equilibrium relation between the quantity of the adsorbed material and the partial pressure (gases) or concentration (liquids) in the bulk fluid phase at constant temperature. That is a fundamental concept in the adsorption science because it is a primary source of information on the adsorption process.

There are many studies aimed at describing adsorption isotherm processes. [50] Irving Langmuir was the first to derive a scientifically based adsorption isotherm in 1918. [21] The Langmuir model was initially developed to describe gases adsorbed on solid surfaces, but it has been widely used to quantify the sorption of molecules from liquid phases. First, the model assumes that all of the adsorption sites of the surface are energetically identical (equal binding strengths with a given sorbate). Second, only a monolayer of sorbate can be adsorbed to the solid and, no interactions are presented among the adsorbates; once all sites are occupied by sorbate molecules, no more adsorption can occur.

Considering the adsorption mechanism I.6, the rate of adsorption of the gas A to a surface will be proportional to the product of P_A multiply by the fraction of the surface available for sorption:

$$R_{ads} = k_{ads} P_A (1 - \theta_A) \tag{I.8}$$

Θ_A is the surface coverage, defined as is the fractional occupancy of the adsorption sites. It can be expressed by the ratio of the concentrations of the adsorbed gas at the surface Γ, in $molecules/m^2$, to the total number of adsorption sites per unit area, Γ_∞, in $number/m^2$:

$$\Theta_A = \frac{\Gamma}{\Gamma_\infty} \tag{I.9}$$

Therefore, the quantity $(1 - \Theta_A)$ is the fraction not covered by the gas. The rate of desorption depends on the concentration or number of gas molecules adsorbed to the surface:

$$R_{des} = k_{des} \theta_A \tag{I.10}$$

Thus, for a gas containing a single adsorbate, the adsorption equilibrium constant is:

$$K = \frac{k_{ads}}{k_{des}} = \frac{\Theta_A}{(1 - \Theta_A) P_A} \tag{I.11}$$

from which the Langumir isotherm is:

$$\Theta_A = \frac{KP_A}{1 + KP_A} \tag{I.12}$$

At low partial pressures, the denominator of the Equation I.12 approaches 1, and the fraction adsorbed varies linearly with the partial pressure of the adsorptive gas (Henry's adsorption isotherm). [51] This suggests that, at higher partial pressure the tendency toward the adsorption increases. However, as the pressure increases, the number of available adsorption sites decreases, and further adsorption becomes increasingly difficult. At high pressures, the denominator of the Equation I.12 approaches KP_A, and the fraction of occupied sites increases asymptotically to 1.

The Langmuir isotherm may be applied to liquids, with the partial pressure replaced by concentration. [52] Thus, the adsorption or desorption of a surfactant molecule (S) at solid surface is an exchange between a solvent molecule (W) and the surfactant at the adsorption site X:

$$S_{bulk} + X - W \underset{k_{des}}{\overset{k_{ads}}{\rightleftharpoons}} X - S + W \tag{I.13}$$

and the relative isotherm Langmuir is:

$$\Gamma = \Gamma_\infty \frac{K[S]_{bulk}}{1 + K[S]_{bulk}} \tag{I.14}$$

where $[S]_{bulk}$ is the surfactant concentration in the bulk, Γ the amount of surfactant adsorbed per unit area and Γ_∞ the maximum quantity of surfactant that can be adsorbed.

Since the pioneering work of Langmuir, a variety of classical models have been proposed for modelling equilibrium adsorption phenomena [53–63], such as the Freundlich [64] for heterogeneous surfaces and the BET [65] for a multilayer adsorption. Frumkin isotherm is typically used for systems with adsorbate-adsorbate interaction at the interfaces [66, 67]. This model can be appropriate

to describe the adsorption of ionic surfactant at solid surface: the shortage of polar groups on hydrophobic alkyl chain of surfactants, results in more impacted contact between surfactant molecules.

Although the increasing number for modeling equilibrium adsorption phenomena give better correlation with the experimental data, they are only applicable for a specified system and extra fitting parameters need to be determined before they apply. So, in spite of the several approximations contained in the model, Langmuir isotherm remains the most popular and reported method in numerous studies.

I.3.2 Molecular modelling and its relevance to adsorption phenomena

With the fast development of computer science, many techniques have been introduced for the study of adsorption theory, such as the Density Functional Theory (DFT) [68, 69] and Molecular Dynamics (MD) simulations. These methods can construct the adsorption system in the conditions that are hard to achieve by experiment study, and more importantly, they can probe into microscopic properties of the system. The comprehension of adsorption mechanism can be promoted by reconciliation of simulation results with reliable experimental data and the development of molecular models to prediction the microscopic physics. The combination of material synthesis, characterization, and computation requires a significant critical mass of expertise of a scope only afforded through extensive scientific collaborations. Molecular modelling may be a very promising method for the fast development of industrial processes, such as in gas separation and emulsion polymerization. Among these techniques, MD simulation is the most widely applied. In principle, if the interaction potentials of the system are correctly described, all the thermodynamic properties of the adsorption system, as well as the orientation of the adsorbed molecules, can be determined. Molecular Dynamics simulations solve the equations of motion of molecules, and the fluid properties are calculated as a time average.

I.3.3 Methods for gas carbon dioxide separation and capture

The rapid economic growth of the last century has been accompanied by a dramatic increase in the demand for energy and, as a consequence, by an increase in the use of fossil fuels. The combustion of these fossil fuels, which emits to the atmosphere carbon dioxide (CO_2), is probably the single most important factor in the human influence on climate change. [70] For example in the last sixty years, the concentration of CO_2 in the atmosphere has increased from 314 ppm (parts per million) to a record high level of 410 ppm, [71] leading to an increment of 1.0 °C in the temperature of the earth's surface. [72] Therefore, there is an urgent need to reduce the level of carbon dioxide in the atmosphere. The challenge of reducing CO_2 emissions has been tackled from different perspectives. These include, improving energy efficiency and conservation, developing clean coal and natural gas technologies [73], and using alternative energy sources such as solar, wind, hydro, and nuclear power. [74] Despite their advantages, all these strategies have limitations which compromise their applications, and as of yet, can not substantially replace the use of fossil fuel. In fact, fossil fuel is predicted to remain the main energy source for at least the next two decades. [75]

As a short-term solution, CO_2 capture and storage (CCS) is an imperative approach for reducing atmospheric CO_2 concentration. Three different CCS strategies are employed in large-scale production plants: pre-combustion, post-combustion and oxy-fuel combustion. Post-combustion is the most widely used technology because it can be retrofitted into existing power plants. In this case, there are many technologies for separating carbon dioxide from the flue gas stream: solvent absorption, physical adsorption, membrane separation and cryogenic distillation. [76–81] From these methods, solvent absorption with amine

is currently the dominant separation approach employed, but it presents various disadvantages, such as amine degradation and the energy required for the absorbent regenerations. [70] In contrast to solvent absorption, a solid sorbent forms weak physical interactions with CO_2, therefore its regeneration can be easily accomplished by swigging the pressure (PSA) or the temperature (TSA). [82] Large specific surface area, high selectivity and pore structure are the general characteristics for selecting good solid sorbents. However, the choice of which sorbent material to use depends on the type of combustion strategy (pre-, post- or oxy-fuel combustion) used for the formation of CO_2. [70] Each strategy creates different conditions (e.g., temperature, pressure, CO_2 content and presence of other type of gases), which influence the carbon dioxide adsorption. For example, in the case of post-combustion the separation of the coal-fired flue gas involves CO_2/N_2, whose pressure is normally at 1 bar and the operating temperature is between 40 °C and 80 °C. In pre-combustion, the separation of CO_2 is from either H_2 or CH_4 at 30 bar and 40 °C. [82] Moreover, the flue gas resulting from the post-combustion process contains 10-15% of CO_2, whereas the pre-combustion technology produces a gas mixture composed of the 38% of CO_2. [75] Obviously, an ideal adsorbent should have good stability and adsorption efficiency under a wide range of process conditions. Currently, typical materials for a solid sorbent include activated carbon, silica, aerogels, zeolites, metal-organic frameworks and porous materials like amine-based sorbents. [83]. Nonetheless despite the variety of porous solids available, there is a need for better sorbents because they do suffer from several drawbacks: difficulty to handle the solids, slow adsorption rate, low CO_2 selectivity, as well as chemical, thermal and mechanical instability during the processing cycles. [75]

Recently, graphene has attracted considerable amount of attention due to its single-atom thickness coupled to impressive thermal, electrical, optical, and me-

chanical proprieties. [84] Graphene is a two-dimensional material, which consists of a single atomic layer of sp^2-hybridized carbon atoms arranged in a hexagonal (honeycomb) lattice. This cyclic configuration gives a large and easy accessible surface area ($\approx 2630 mg^2 g^{-1}$) [85] accompanied by an incredible flexibility and excellent mechanical proprieties. The atoms of the lattice are covalently bound to three adjacent carbon atoms, in the xy-plane, and are also sandwiched between two π-electron clouds, along z-axis. [86] These electron clouds are responsible for the good thermal, electrical and optical properties of graphene [87]. It is also recognized as a powerful adsorbent because its electronic structure is additionally responsible for establishing London dispersion forces with molecules situated at its surface. [88] More specifically, graphene exhibits a good adsorption strength for CO_2, stronger than for CH_4 and N_2. [89] A graphene sheet is essentially a two-dimensional (2D) material, and while this geometry offers a large and easily-accessed surface area, the amount of active material per projected area is low.

This ratio can be increased substantially by constructing three-dimensional (3D) graphene-based architectures. Such a structure can be obtained by self-assembly of graphene nano-sheets in solution followed by drying-out the aqueous phase. [90] The resulting structure is 3D porous and have been explored in many applications such as batteries, sensors, catalysts, and absorbents. [91] Nevertheless, adsorption of polymer nanoparticles on the graphene surface was found to be necessary to improve consistency, durability and mechanical resistance. [92] The properties of these graphene-polymer composites depend on the type of polymer adsorbed.

Incorporating different functional groups into the polymer can modulate the interaction of the polymer with graphene or with external molecules. [92] It has been demonstrated that the presence of functional groups containing het-

eroatoms, in particular nitrogen and oxygen, in the polymer composition led to a superior CO_2-polymer interaction energy via either dipole-quadrupole or hydrogen-bonding interactions, or both. [82] This strategy has often been exploited to improve the gas sorption of materials for low pressure capture applications, such as those relevant in flue streams and for capture from ambient air. [89, 93] In recent years various computational studies addressed the capture of CO_2 gas, alone or in a mixture, by different type of sorbents. [94–103]

I.4 Main motivation and objectives

As described above, adsorption is an increase in the concentration of a dissolved substance at the interface of a solid and a liquid phase due to the operation of surface forces. Adsorption has emerged as an important process for various industrial applications, such as emulsion polymerization and gas separation.

Surfactants have a crucial role in emulsion polymerization due to their inward properties; namely, they affect the polymer particles nucleation and prevent them from the coagulation by the reduction of surface tension. However, many aspects of their use are poorly understood and cause significant problems. In this thesis the combination of experimental and computational studies will be reported with the aim to elucidate the adsorption properties of ionic and non-ionic surfactants on hydrophobic polymer surface such as poly(styrene). Also, since the particle nucleation behavior of nonionic surfactants exhibits deviations from the Smith-Ewart model [42], which described the kinetic mechanism of the particle nucleation typical for ionic surfactant, we seek to take a deeper look of the behavior of these two classes of surfactants at monomer/polymer-water interface during the emulsion polymerization of styrene.

Three-dimensional graphene-polymer porous materials have been proposed recently as potential adsorbents for carbon dioxide capture. Owing to their mechanical stability and ease of regeneration they can potentially alleviate shortcoming encountered by other sorbents. Molecular dynamics simulation will be performed to study the adsorption of carbon dioxide by different graphene-polymer composite systems. Additionally an estimation of the CO_2 selectivity respect to N_2 and CH_4 will be examined to prove the ability of the composite materials to discriminate against these competing gasses.

I.5 Thesis outline

Chapter I provides the necessary background to understand the remainder of the thesis. A general introduction of adsorption process at liquid and solid interfaces is given, including the most common theories for the thermodynamic of adsorption. In addition, the contribution of atomistic simulations as a promising method for the study of adsorption phenomena is considered. In the section which regards the adsorption phenomena at liquid interface, a brief explanation of surfactants and emulsion systems is necessary to understand the emulsion polymerization process whose mechanism is subsequently summarize. Finally the role of surfactants in emulsion polymerization and their problematics are discussed. Concerning the adsorption at solid interface, recent strategies for the separation and capture of CO_2 used in power plants and other industrial processes are concisely described. Specifically, graphene-polymer composite materials are promising adsorbents for the carbon dioxide sorption, due to the unique proprieties of graphene combining with the polymer adsorbed. Moreover, the main motivation and objectives of the thesis are specified.

Chapter II details the computational method performed in the work of this thesis.

Chapter III reports experimental and computational studies on the adsorption properties of ionic and nonionic surfactants at polymer surface, demonstrating the clear differences in behavior of this two types of surfactants in emulsion polymerization. MD simulations are useful to explain the interactions which occur between the polar group of the surfactants with the solvent at various surfactant densities adsorbed at the polymer surface.

Chapter IV will experimentally and computationally focus on the the behavior of ionic and nonionic surfactants during the polymerization process of styrene, where the organic phase gradually changes from a monomer-rich liquid to a polymeric solid. In particular atomistic simulations will demonstrate in details the different partition of nonionic surfactants between oil and water phases with varying the composition of styrene and polystyrene.

Chapter V presents a comprehensive MD study of the selective adsorption of carbon dioxide for several graphene-polymer composites. Furthermore, the effect of protic groups of the polymers on the CO_2 capture ability of the composites, and on the morphology of the polymers at graphene surface, is analyzed.

Chapter VI summarizes the most relevant conclusions of this thesis.

In order to avoid too elaborate representations and discussions in the individual chapters, the Supporting Information of Chapter III-V is represented in **Appendixes I-III** respectively, while the **Abbreviations and acronyms** used in the thesis are listed at the very end.

References

[1] Yang, R. T. *Gas separation by adsorption processes;* Butterworth-Heinemann, 2013.

[2] Parfitt, G. D.; Rochester, C. H. *Adsorption from solution at the solid/liquid interface*, Vol. 3; Academic press London, 1983.

[3] Shchukin, E. D.; Pertsov, A. V.; Amelina, E. A.; Zelenev, A. S. *Colloid and surface chemistry*, Vol. 12; Elsevier, 2001.

[4] Chattoraj, D. *Adsorption and the Gibbs surface excess;* Springer Science & Business Media, 2012.

[5] Chandler, D. Interfaces and the driving force of hydrophobic assembly, *Nature* 2005, *437*, 640–647.

[6] Eastoe, J. *Colloid science: Principles, methods and applications;* Wiley Online Library, 2005.

[7] Rosen, M. J.; Kunjappu, J. T. *Surfactants and interfacial phenomena;* John Wiley & Sons, 2012.

[8] Anderson, C. D.; Daniels, E. S. *Emulsion polymerisation and latex applications*, Vol. 14; iSmithers Rapra Publishing, 2003.

[9] Walstra, P. Principles of emulsion formation, *Chem. Eng. Sci.* 1993, *48*(2), 333–349.

[10] Kentish, S.; Wooster, T.; Ashokkumar, M.; Balachandran, S.; Mawson, R.; Simons, L. The use of ultrasonics for nanoemulsion preparation, *Innov. Food Sci. Emerg. Technol.* 2008, *9*(2), 170–175.

[11] Leal-Calderon, F.; Poulin, P. Progress in understanding emulsion metastability and surface forces, *Curr. Opin. Colloid Interface Sci.* 1999, *4*(3), 223–230.

[12] Bancroft, W. D. The theory of emulsification, i, *J. Phys. Chem.* 1912, *16*(3), 177–233.

[13] Finkle, P.; Draper, H. D.; Hildebrand, J. H. The theory of emulsification1, *J. Am. Chem. Soc.* 1923, *45*(12), 2780–2788.

[14] Wilde, P.; Mackie, A.; Husband, F.; Gunning, P.; Morris, V. Proteins and emulsifiers at liquid interfaces, *Adv. Colloid Interface Sci.* 2004, *108*, 63–71.

[15] Verwey, E. J. W.; Overbeek, J. T. G.; Overbeek, J. T. G. *Theory of the stability of lyophobic colloids;* Courier Corporation, 1999.

[16] Deraguin, B.; Landau, L. Theory of the stability of strongly charged lyophobic sols and of the adhesion of strongly charged particles in solution of electrolytes, *Acta Physicochim. USSR* 1941, *14*, 633–662.

[17] Evans, R.; Napper, D.-H. Steric stabilization ii, *Kolloid Z. Z. Polym.* 1973, *251*(5), 329–336.

[18] Capek, I. Degradation of kinetically-stable o/w emulsions, *Adv. Colloid Interface Sci.* 2004, *107*(2-3), 125–155.

[19] Gibbs, J. *The collected work of JW Gibbs;* 1931.

[20] Perrot, P. *A to Z of Thermodynamics;* Oxford University Press on Demand, 1998.

[21] Langmuir, I. The adsorption of gases on plane surfaces of glass, mica and platinum., *J. Am. Chem. Soc.* 1918, *40*(9), 1361–1403.

[22] Asua, J. M. *Polymeric dispersions: principles and applications*, Vol. 335; Springer Science & Business Media, 2012.

[23] Urban, D.; Takamura, K. *Polymer dispersions and their industrial applications*, Vol. 13; Wiley Online Library, 2002.

[24] Gharieh, A.; Mahdavian, A. R.; Salehi-Mobarakeh, H. Preparation of core–shell impact modifier particles for pvc with nanometric shell thickness through seeded emulsion polymerization, *Iran. Polym. J.* 2014, *23*(1), 27–35.

[25] Vincent, B. The effect of adsorbed polymers on dispersion stability, *Adv. Colloid Interface Sci.* 1974, *4*(2-3), 193–277.

[26] Kästner, U. The impact of rheological modifiers on water-borne coatings, *Colloids Surf. A: Physicochemical and Engineering Aspects* 2001, *183*, 805–821.

[27] Plastics—the facts 2016 an analysis of european plastics production, demand and waste data. Europe, P. 2016.

[28] Bandiera, M.; Balk, R.; Barandiaran, M. J. One-pot synthesis of water-borne polymeric dispersions stabilized with alkali-soluble resins, *Polym. J.* 2018, *10*(1), 88.

[29] Harkins, W. D. A General Theory of the Mechanism of Emulsion Polymerization, *J. Am. Chem. Soc.* 1947, *69*, 1428–1444.

[30] Priest, W. Partice growth in the aqueous polymerization of vinyl acetate, *J. Phys. Chem. A* 1952, *56*(9), 1077–1082.

[31] Asua, J. M. Emulsion polymerization: from fundamental mechanisms to process developments, *J. Polym. Sci. A: Polymer Chemistry* 2004, *42*(5), 1025–1041.

[32] van Herk, A. M. *Chemistry and technology of emulsion polymerisation;* John Wiley & Sons, 2013.

[33] Bassett, D. R.; Hamielec, A. E.; others. *Emulsion polymers and emulsion polymerization;* American Chemical Society, 1981.

[34] Ballard, N.; Urrutia, J.; Eizagirre, S.; Schäfer, T.; Diaconu, G.; de la Cal, J. C.; Asua, J. M. Surfactant Kinetics and Their Importance in Nucleation Events in (Mini)emulsion Polymerization Revealed by Quartz Crystal Microbalance with Dissipation Monitoring, *Langmuir* 2014, *30*, 9053–9062.

[35] Masa, J. A.; De Arbina, L. L.; Asua, J. M. A comparison between miniemulsion and conventional emulsion terpolymerization of styrene, 2-ethylhexyl acrylate and methacrylic acid, *J. Appl. Polym. Sci.* 1993, *48*(2), 205–213.

[36] Becher, P.; Hamor, W. A. *Emulsions: theory and practice*, Vol. 135; Reinhold New York, 1957.

[37] Unzué, M. J.; Asua, J. M. Semicontinuous miniemulsion terpolymerization: Effect of the operation conditions, *J. Appl. Polym. Sci.* 1993, *49*(1), 81–90.

[38] Hansen, F. In *Acs Symposium Series*, Vol. 492, pages 12–27. AMER CHEMICAL SOC 1155 16TH ST, NW, WASHINGTON, DC 20036, 1992.

[39] Keddie, J. L. Film formation of latex, *Mater. Sci. Eng. R-Rep.* 1997, *21*, 101–170.

[40] Gilbert, R. G. *Emulsion Polymerization: A Mechanistic Approach*, Colloid Science; Academic Press: London, 1995.

[41] Thickett, S. C.; Gilbert, R. G. Emulsion polymerization: State of the art in kinetics and mechanisms, *Polymer* 2007, *48*, 6965–6991.

[42] Smith, W. V.; Ewart, R. H. Kinetics of Emulsion Polymerization, *J. Chem. Phys.* 1948, *16*, 592–599.

[43] Piirma, I.; Chang, M. Emulsion polymerization of styrene: Nucleation studies with nonionic emulsifier, *J. Polym. Sci., Polym. Chem. Ed.* 1982, *20*, 489–498.

[44] Piirma, I.; Maw, T. S. Emulsion polymerization: some nonionic emulsifier effects, *Polym. Bull.* 1984, *11*, 497–504.

[45] Özdeğer, E.; Sudol, E. D.; El-Aasser, M. S.; Klein, A. Role of the nonionic surfactant Triton X-405 in emulsion polymerization. I. Homopolymerization of styrene, *J. Polym. Sci. A Polym. Chem.* 1997, *35*, 3813–3825.

[46] Okubo, M.; Kobayashi, H.; Matoba, T.; Oshima, Y. Incorporation of Nonionic Emulsifiers Inside Particles in Emulsion Polymerization: Mechanism and Methods of Suppression, *Langmuir* 2006, *22*, 8727–8731.

[47] Kobayashi, H.; Miyanaga, E.; Okubo, M. Preparation of Multihollow Polymer Particles by Seeded Emulsion Polymerization Using Seed Particles with Incorporated Nonionic Emulsifier, *Langmuir* 2007, *23*, 8703–8708.

[48] Okubo, M.; Kobayashi, H.; Huang, C.; Miyanaga, E.; Suzuki, T. Water Absorption Behavior of Polystyrene Particles Prepared by Emulsion Polymerization with Nonionic Emulsifiers and Innovative Easy Synthesis of Hollow Particles, *Langmuir* 2017, *33*, 3468–3475.

[49] Dabrowski, A. Adsorption—from theory to practice, *Adv. Colloid Interface Sci.* 2001, *93*(1-3), 135–224.

[50] Foo, K. Y.; Hameed, B. H. Insights into the modeling of adsorption isotherm systems, *Chem. Eng. J.* 2010, *156*(1), 2–10.

[51] Erbil, H. *Surface Chemistry of Solid and Liquid Interfaces;* Wiley, 2006.

[52] Masel, R. I.; Masel, R. I. *Principles of adsorption and reaction on solid surfaces*, Vol. 3; John Wiley & Sons, 1996.

[53] Sips, R. On the structure of a catalyst surface, *J. Chem. Phys.* 1948, *16*(5), 490–495.

[54] Koble, R. A.; Corrigan, T. E. Adsorption isotherms for pure hydrocarbons, *Industrial & Engineering Chemistry* 1952, *44*(2), 383–387.

[55] Toth, J. State equation of the solid-gas interface layers, *Acta Chim. Hung.* 1971, *69*, 311–328.

[56] Rudzinski, W.; Lee, S.-L.; Panczyk, T.; Yan, C.-C. S. A fractal approach to adsorption on heterogeneous solids surfaces. 2. thermodynamic analysis of experimental adsorption data, *J. Phys. Chem. B* 2001, *105*(44), 10857–10866.

[57] Zhou, L.; Zhang, J.; Zhou, Y. A simple isotherm equation for modeling the adsorption equilibria on porous solids over wide temperature ranges, *Langmuir* 2001, *17*(18), 5503–5507.

[58] Al-Duri, B.; Mckay, G. Prediction of binary systems for kinetics of batch adsorption using basic dyes onto activated carbon, *Chem. Eng. Sci.* 1991, *46*(1), 193–204.

[59] Kumar, K. V.; de Castro, M. M.; Martinez-Escandell, M.; Molina-Sabio, M.; Rodriguez-Reinoso, F. A site energy distribution function from toth isotherm for adsorption of gases on heterogeneous surfaces, *Phys. Chem. Chem. Phys.* 2011, *13*(13), 5753–5759.

[60] Azizian, S.; Volkov, A. G. A new isotherm for nondissociative gas adsorption with two different states of an adsorbate, *Chem. Phys. Lett.* 2008, *454*(4-6), 409–414.

[61] Azizian, S.; Bashiri, H.; Volkov, A. G. Derivation of azizian–volkov (av)-isotherm based on statistical thermodynamics, *Colloids Surf. A: Physicochemical and Engineering Aspects* 2009, *335*(1-3), 28–32.

[62] Azizian, S.; Bashiri, H. A new isotherm for multisite occupancy adsorption of binary gaseous mixtures, *Langmuir* 2009, *25*(4), 2309–2312.

[63] Bashiri, H.; Orouji, S. A new isotherm for multilayer gas adsorption on heterogeneous solid surfaces, *Theor. Chem. Acc.* 2015, *134*(1), 1594.

[64] Freundlich, H.; Hatfield, H. S. *Colloid and capillary chemistry;* Methuen And Co. Ltd; London, 1926.

[65] Sing, K. S. Adsorption methods for the characterization of porous materials, *Adv. Colloid Interface Sci.* 1998, *76*, 3–11.

[66] Frumkin, A. Die kapillarkurve der höheren fettsäuren und die zustandsgleichung der oberflächenschicht, *Z. Phys. Chem.* 1925, *116*(1), 466–484.

[67] Volkova-Gugeshashvili, M. I.; Volkov, A. G.; Markin, V. S. Adsorption at Liquid Interfaces: The Generalized Frumkin Isotherm and Interfacial Structure, *Russ. J. Electrochem.* 2006, *42*, 1073–1078.

[68] Evans, R. The nature of the liquid-vapour interface and other topics in the statistical mechanics of non-uniform, classical fluids, *Adv. Phys.* 1979, *28*(2), 143–200.

[69] Tarazona, P.; Marconi, U. M. B.; Evans, R. Phase equilibria of fluid interfaces and confined fluids: non-local versus local density functionals, *Mol. Phys.* 1987, *60*(3), 573–595.

[70] Leung, D. Y.; Caramanna, G.; Maroto-Valer, M. M. An overview of current status of carbon dioxide capture and storage technologies, *Renew. Sust. Energ. Rev.* 2014, *39*, 426–443.

[71] Scripps Keeling Curve Website: `https://www.co2.earth`, measured at Mauna Loa Observatory, Hawaii. 2018.

[72] National Centers for Environmental Information: `https://www.ncei.noaa.gov` . 2018.

[73] Kinnon, M. A. M.; Brouwer, J.; Samuelsen, S. The role of natural gas and its infrastructure in mitigating greenhouse gas emissions, improving regional air quality, and renewable resource integration, *Prog. Energy Combust. Sci.* 2018, *64*, 62–92.

[74] Jacobson, M. Z. Review of solutions to global warming, air pollution, and energy security, *Energy Environ. Sci.* 2009, *2*, 148–173.

[75] Kenarsari, S. D.; Yang, D.; Jiang, G.; Zhang, S.; Wang, J.; Russell, A. G.; Wei, Q.; Fan, M. Review of recent advances in carbon dioxide separation and capture, *RSC Adv.* 2013, *3*, 22739–22773.

[76] Göttlicher, G.; Pruschek, R. Comparison of CO_2 removal systems for fossil-fuelled power plant processes, *Energy Convers. Manag.* 1997, *38*, S173–S178.

[77] Takamura, Y.; Aoki, J.; Uchida, S.; Narita, S. Application of high-pressure swing adsorption process for improvement of CO_2 recovery system from flue gas, *Can. J. Chem. Eng.* 2001, *79*, 812–816.

[78] Aaron, D.; Tsouris, C. Separation of CO_2 from Flue Gas: A Review, *Sep. Sci. Technol.* 2005, *402*, 321–348.

[79] Tuinier, M. J.; van Sint Annaland, M.; Kramer, G. J.; Kuipers, J. A. M. Cryogenic CO_2 capture using dynamically operated packed beds, *Chem. Eng. Sci.* 2010, *65*, 114–119.

[80] Bhown, A. S.; Freeman, B. C. Analysis and Status of Post-Combustion Carbon Dioxide Capture Technologies, *Environ. Sci. Technol.* 2011, *45*, 8624–8632.

[81] Clausse, M.; Merel, J.; Meunier, F. Numerical parametric study on CO_2 capture by indirect thermal swing adsorption, *Int. J. of Greenh. Gas Con.* 2011, *5*, 1206–1213.

[82] Dawson, R.; Cooper, A. I.; Adams, D. Chemical functionalization strategies for carbon dioxide capture in microporous organic polymers, *Polym. Int.* 2013, *62*, 345–352.

[83] Zulfiqar, S.; Mantione, D.; El Tall, O.; Sarwar, M. I.; Ruipérez, F.; Rothenberger, A.; Mecerreyes, D. Nanoporous amide networks based on tetraphenyladamantane for selective CO_2 capture, *J. Mater. Chem. A* 2016, *4*, 8190–8197.

[84] Meyer, J. C.; Geim, A. K.; Katsnelson, M. I.; Novoselov, K. S.; Booth, T. J.; Roth, S. The structure of suspended graphene sheets, *Nature* 2007, *446*, 60–63.

[85] Matharu, R. K.; Porwal, H.; Ciric, L.; Edirisinghe, M. The effect of graphene–poly(methyl methacrylate) fibres on microbial growth, *Interface Focus* 2018, *8*.

[86] Scida, K.; Stege, P. W.; Haby, G.; Messina, G. A.; García, C. D. Recent applications of carbon-based nanomaterials in analytical chemistry: Critical review, *Anal. Chim. Acta* 2011, *691*, 6–17.

[87] Wang, J.; Ma, F.; Liang, W.; Sun, M. Electrical properties and applications of graphene, hexagonal boron nitride (h-BN), and graphene/h-BN heterostructures, *Mater. Today Phys.* 2017, *2*, 6–34.

[88] Pykal, M.; Jurečka, P.; Karlický, F.; Otyepka, M. Modelling of graphene functionalization, *Phys. Chem. Chem. Phys.* 2016, *18*, 6351–6372.

[89] D'Alessandro, D.; Smit, B.; Long, J. Carbon dioxide capture: Prospects for new materials, *Angewandte Chemie International Edition* 2010, *49*, 6058–6082.

[90] Rodriguez-Couto, S.; Arzac, A.; Leal, G. P.; Tomovska, R. Reduced graphene oxide hydrogels and xerogels provide efficient platforms for immobilization and laccase production by Trametes pubescens, *Biotechnol. J.* 2014, *9*, 578–584.

[91] Yang, Z.; Chabi, S.; Xia, Y.; Zhu, Y. Preparation of 3D graphene-based architectures and their applications in supercapacitors, *Pro. Nat. Sci-Mater.* 2015, *25*, 554–562.

[92] Ormategui, N.; Veloso, A.; Leal, G. P.; Rodriguez-Couto, S.; Tomovska, R. Design of Stable and Powerful Nanobiocatalysts, Based on Enzyme Laccase Immobilized on Self-Assembled 3D Graphene/Polymer Composite Hydrogels, *ACS Appl. Mater. Interfaces* 2015, *7*, 14104–14112.

[93] Gibson, J. A. A.; Mangano, E.; Shiko, E.; Greenaway, A. G.; Gromov, A. V.; Lozinska, M. M.; Friedrich, D.; Campbell, E. E. B.; Wright, P. A.; Brandani, S. Adsorption materials and processes for carbon capture from gas-fired power plants: AMPGas, *Ind. Eng. Chem. Res.* 2016, *55*, 3840–3851.

[94] Wu, B.; Yang, X. A molecular simulation of interactions between graphene nanosheets and supercritical CO_2, *J. Colloid Interface Sci.* 2011, *361*, 1–8.

[95] Liu, Y.; Wilcox, J. Molecular simulation studies of co_2 adsorption by carbon model compounds for carbon capture and sequestration applications, *Environ. Sci. Technol.* 2012, *47*, 95–101.

[96] Joos, L.; Swisher, J. A.; Smit, B. Molecular Simulation Study of the Competitive Adsorption of H_2O and CO_2 in Zeolite 13X, *Langmuir* 2013, *29*, 15936–15942.

[97] Jiao, S.; Xu, Z. Selective Gas Diffusion in Graphene Oxides Membranes: A Molecular Dynamics Simulations Study, *ACS Appl. Mater. Interfaces* 2015, *7*, 9052–9059.

[98] Rahimi, M.; Singh, J. K.; Müller-Plathe, F. Adsorption and separation of binary and ternary mixtures of SO_2, CO_2 and N_2 by ordered carbon nanotube arrays: grand-canonical Monte Carlo simulation, *Phys. Chem. Chem. Phys.* 2016, *18*, 4112–4120.

[99] Li, W.; Zheng, X.; Dong, Z.; Li, C.; Wang, W.; Yan, Y.; Zhang, J. Molecular Dynamics Simulations of CO_2/N_2 Separation through Two-Dimensional Graphene Oxide Membranes, *J. Phys. Chem. C* 2016, *120*, 26061–26066.

[100] Trinh, T. T.; Tran, K.-Q.; Bach, Q.-V.; Trinh, D. Q. A Molecular Dynamics Simulation Study on Separation Selectivity of CO_2/CH_4 Mixture in Mesoporous Carbons, *Energy Procedia* 2016, *86*, 144–149.

[101] Kandagal, V. S.; Chen, F.; Jónsson, E.; Pringle, J. M.; Forsyth, M. Molecular simulation study of CO_2 and N_2 absorption in a phosphonium based organic ionic plastic crystal, *J. Chem. Phys.* 2017, *147*, 124703.

[102] Gao, M.; Misquitta, A. J.; Yang, C.; Todorov, I. T.; Mutter, A.; Dove, M. T. Molecular dynamics study of CO_2 absorption and desorption in zinc imidazolate frameworks, *Mol. Syst. Des. Eng.* 2017, *2*, 457–469.

[103] Wang, H.; Qu, Z.; Bai, J.; Qiu, Y. Combined grand canonical Monte Carlo and finite volume method simulation method for investigation of direct air capture of low concentration CO_2 by 5A zeolite adsorbent bed, *Int. J. Heat Mass Transf.* 2018, *126*, 1219–1235.

Chapter II

Methods

Contents

II.1 Classical Molecular Dynamics Simulations

Molecular Dynamics (MD) simulations have become a powerful tool to predict the structural assembly of molecules and their microscopic interactions. MD simulation gives informations about the dynamical proprieties of a system in full atomistic detail. The possibility of describing complex molecular systems explains the great diffusion of MD in the context of structural biochemistry and material science. In fact, this method acts as a bridge between the microscopic length and time scale and the macroscopic world of the laboratory [1]: it allows to understand dynamic and structural behavior at resolutions that are not accessible to the experimental techniques. A theoretical treatment of the motions and interactions of molecules should be rigorously found on the principles of quantum mechanics due to their microscopic nature. Unfortunately, such approach makes the analytical calculations impractical or even impossible, for systems containing thousands of atoms. MD simulation circumvents this problem, applying approximations in the mathematical model chosen to represent a physical system. [2]

The concept of the molecular dynamics method depends on a very important simplification in quantum mechanics, the Born-Oppenheimer approximation, [3] which is a simplification of the behavior of a system of nuclei and electrons. The nuclei mass is much larger than the mass of the electrons and its velocity is correspondingly small. Thus, the nucleus interacts with the electrons as if they were a charge cloud, while the electrons feel as if the nuclei were static. As a consequence, the electron motions are not considered, but only the dynamics of nuclei are taken in explicit account: the electrons are moved "instantly" to any position of nuclei, and remain in their ground state. Thus, the electron transfer processes and electronically excited states can not be treated. [4]

In MD simulations the dynamics of a systems, which is the time evolution of a set of N interacting atoms, is generated by the numerical solution of Newton's classic equations of motion (Equation II.1), where $r_i(t) = (x_i(t), y_i(t), z_i(t))$ is the position vector of a single particle, F_i denotes the force acting at time t on i-th atom (due to the interaction with other atoms) and m_i is the mass of the atom.

$$F_i = m_i \frac{d^2 r_i(t)}{dt^2} \quad \text{with} \quad i = 1...N \tag{II.1}$$

The force is given by the negative gradient of the potential energy function $U(r_1, ..., r_N)$ which describes the interaction between the atoms, with respect to the position r_i of the atom i,

$$F_i = -\nabla_{r_i} U(r_1, ..., r_N) = -(\frac{\partial U}{\partial x_i}, \frac{\partial U}{\partial y_i}, \frac{\partial U}{\partial z_i}) \tag{II.2}$$

Newton's equation of motion can be related to the derivative of the potential energy to the change in position as a function of time. If the potential energy of the system is known then, given the coordinates of a starting structure and a set of velocities, the force acting on each atom can be calculate and a new set of coordinates can be generated, from which new forces can be calculated. Repetition of this procedure will generated a trajectory corresponding to the evolution of the system in time. To integrate the Newton's equations of motion, numerical finite different methods [5–7] are used to find an expression for the positions $r_i(t + \Delta t)$ at time $(t + \Delta t)$ in terms of the already known positions at time t. In this thesis, all computer simulations are performed using the molecular dynamics package **GROMACS 4.5.6** [8] and the equations of motion are solved by the **leap-frog** time integration scheme. [9]

II.2 Potential functions

The crucial step in molecular dynamics simulation is to describe the intermolecular and intramolecular interactions of a system, which is often termed as force-field. [10] There are different ways to obtain the potential functions or force fields. These parameters can be derived from experimental and/or ab-initio calculations of small molecules or fragments, and it is assumed that such parameters can be transferable to the larger molecule of interest. An alternative way is to fit the potential parameters to the values obtained from experimental measurements. [11–17] There are several reliable force fields [18–20] developed for simulations of macromolecules. In this thesis have been used those of the OPLS/OPLS-AA force field [21, 22], parametrized to reproduce thermodynamic data of small organic molecules in the liquid state. The first point when building a realistic atomistic model is to evaluate the forces acting on every particle. As described above in Equation II.2, these forces should be derived from the potential energy function. Within the framework of classical mechanics, it is natural to distinguish between **bonded** and **nonbonded** interactions.

$$U(r) = U_{bonded}(r) + U_{non-bonded}(r) \tag{II.3}$$

U_{bonded}, is the **bonded** term and it considers the intramolecular bonding interactions of the systems:

$$\begin{aligned} U_{bonded}(r) = & \sum_{bonds} K_b(b - b_0)^2 \\ & + \sum_{angles} K_\theta(\theta - \theta_0)^2 \\ & + \sum_{torsions} \frac{1}{2}[F_1(1 + \cos(\phi)) + F_2(1 - \cos(2\phi)) + \\ & \qquad + F_3(1 + \cos(3\phi)) + F_4(1 - \cos(4\phi))] \\ & + \sum_{impropers} K_\varepsilon(\varepsilon - \varepsilon_0)^2 \end{aligned} \tag{II.4}$$

The *first two terms* represent the energies of deformation of the *bond length* b and *bond angle* θ from their respective equilibrium values b_0 and θ_0. The *third term* is the *torsional* energy describing the rotations around the chemical bond. The functional form which models the torsional interaction is expressed as the first three or four cosine terms of a Fourier series [23], where F_n are the Fourier coefficients and ϕ is the current torsional angle. The *last term* describes the potential for the *improper dihedrals*, which describes the energy required to deform a planar group of atoms from its equilibrium angle ε_0. The labels K, in the Equation II.4, indicate the force constants.

The **second term** in the **Equation II.3**, $U_{non-bonded}$, representing the **non-bonding interactions** between atoms, is usually described as two-body potential energy function of the distance (r_{ij}) between the (i, j)-pairs of atoms. This potential function is expressed as the **sum** of the **Lennard-Jones** and **Coulomb** interactions:

$$U_{non-bonded} = \sum_{atompairs} 4\epsilon_{ij}\left(\left(\frac{\sigma_{ij}}{r_{ij}}\right)^{12} - \left(\frac{\sigma_{ij}}{r_{ij}}\right)^{6}\right) + \sum_{atompairs} \frac{q_i q_j}{4\pi\epsilon_0\epsilon_r r_{ij}} \quad \text{(II.5)}$$

The **Lennard Jones potential**, first term in the **Equation II.5**, accounts for two different forces which act on a pair of interacting particles: an *attractive* force, which describes the attraction at long distances (*van der Waals* force, or dispersion force) and a *repulsive* force which acts at short ranges (the *Pauli* repulsion). Thus, the r_{ij}^{-6} and r_{ij}^{-12} are the attractive and repulsive terms respectively.

ϵ_{ij} relates to the Lennard Jones potential well depth and σ_{ij} is the distance at which the inter-particle potential is zero. These parameters ϵ_{ij} and σ_{ij}, which characterize every atom type, can be combined to obtain the corresponding parameters for the pair interaction. The interpretations of the Lennard Jones parameters depends on the type of combination rule chosen. The *Lorentz-Berthelot combination rules* [24] are commonly used in molecular simulations:

$$\sigma_{ij} = \frac{\sigma_{ii} + \sigma_{jj}}{2} \qquad \epsilon_{ij} = \sqrt{\epsilon_{ii}\epsilon_{jj}} \quad \text{(II.6)}$$

In *OPLS* force fields, the *combination rules* employed for the Lennard Jones coefficients are [21, 25]:

$$\sigma_{ij} = \sqrt{\sigma_{ii}\sigma_{jj}} \qquad \epsilon_{ij} = \sqrt{\epsilon_{ii}\epsilon_{jj}} \quad \text{(II.7)}$$

The same expression is used for intramolecular non-bonded interactions between all pairs of atoms separated by more than three or more bonds. However, atoms in the same molecule can occasionally become very close to each other, leading to large values for the non-bonded energy and forces, in particular van der Waals. So, special measures are sometimes needed to accommodate this. Interactions

between atoms at the same molecule separated by three covalent bonds, the so-called 1-4 interactions, are treated in special way because their intermolecular distance is too short to be described by the LJ and Coulomb potentials. There are different variations of how to treat the 1-4 interactions. In OPLS-AA the 1,4-intramolecular interactions are reduced by a factor of two in order to use the same parameters for the intra- and intermolecular interactions and to prevent the van der Waals interaction overwhelming the torsional interaction. [21]

The **second term** in the **Equation II.5**, represents the **Coulomb interaction** if electrostatic charges are present. Opposite atom charges attract and like atom charges repel each other. In this potential, the force of the attraction is inversely proportional to the square of distance. q_i and q_j are the partial charges of atoms of type i and j, and ϵ_0 ϵ_r are the vacuum and the relative permittivities, respectively. Coulomb interactions decay slowly in comparison to van der Waals interactions. Coulomb force computation is the most time consuming part of the force computing process in molecular dynamics. [26] A variety of methods have been developed to handle the problem of the long range of interactions in molecular dynamics. The most simple method is the implementation of a cut off distance which means that the forces are computed until a fixed distance afterward the interaction is neglected. The *cut off* method is very popular in MD simulations however is not suitable in many systems and phenomena where long range electrostatic forces are important such us ionic systems (ionic liquids or ionic crystals), electrosmotic flow and electrophoresis. [27–29] *Ewald summation and particle mesh Ewald (PME)* are widely useful methodologies for evaluating the potential of large periodic systems because they have high accuracy and reasonable speed when computing long-range interactions. [30, 31]

II.3 Constraints

In a system containing polyatomic molecules, intra-molecular interaction arises. When a force field is used to model the system, the intra-molecular interaction can be decomposed into several bonded potential terms describing bonds, angles, dihedral angles, etc. Among these terms, bonds can be treated as harmonic potential with the minimum at the reference bond lengths; additionally, constraints are often introduced to maintain bonds at constant lengths, mainly for the purpose of increasing the time step of integration. On one hand, the vibrations of the bonds are in higher frequencies than, for instance, the low-frequency conformational changes regarding dihedral angles, and are less interested in MD simulations. Constraining bond vibrations will diminish the high-frequency motions in the system and therefore allow an increase in the integration time step. The constraint hydrogen bond prevents the very light hydrogen atoms from moving too far away in a relatively large integration time step. Numerous algorithm have been developed to enhance the stability and increase the efficiency of MD simulations. [32] The constraint equations are introduced into the equation of motion in the form of Lagrange multipliers.

$$\frac{\partial^2 r_i(t)}{\partial t^2} m_i = -\frac{\partial}{\partial r_i}\left[U(r_i(t)) + \sum_{k=1}^{n} \lambda_k \sigma_k(t)\right] \quad \text{with} \quad i = 1...N \tag{II.8}$$

The *LINCS* (linear constraint solver) [33] is a method that resets the constraint distances after an unconstrained update. The constraint equation takes the form:

$$\sigma_k = \|r_a - r_b\| - d_{ab} = 0 \quad \text{with} \quad K = 1, ..., N_c \tag{II.9}$$

where a and b are the two atoms involved in the K-th constraint, d_{ab} is the required distance between a and b and N_c is the total number of constraints. The method is non-iterative, as it is carried out in two steps; the first step is to constrain the projection of the new bond on the old bond while the second step is to correct the bond lengthening due to the rotation. The *SHAKE* algorithm [34] consists of a constraint equation in which the velocities are reset at every time t:

$$\sigma_k(t) = \|r_a - r_b\|^2 - d_{ab}^2 = 0 \quad \text{with} \quad K = 1, ..., N \tag{II.10}$$

The *SETTLE* method [35] is an analytical solution of the SHAKE algorithm, [34] specifically for water molecules.

II.4 Periodic Boundary Conditions

MD simulations are performed on a limited number of particles at the cost of a reasonable computational resource. In general the molecular systems of interest have a size much larger than the system which are simulated. The implementation of **Periodic Boundary Conditions (PBC)** reduce the computational cost of a simulation because is an approximating of a large (infinite) system by using a small part called a unit cell. In the Periodic Boundary Condition the central simulated box is surrounded by the periodic images of itself. The arrangement and movement of particles in the periodic images are exactly the same as in the central simulated box, which means that the particles move out from the box on one side would re-enter the box instantaneously from the opposite side (Figure II.1). This also ensures the constant number of particles in the simulated system. However, caution needs to be exercised to minimize the artifacts caused by the artificial periodicity if one wishes to simulate non-periodic systems, such as

liquids or solutions. [36, 37] The box shapes are limited to space-filling boxes to ensure a seamless connection between boxes, such as triclinic unit cells, which cover cubic, rhombic dodecahedra, and truncated octahedra, etc. GROMACS is based on triclinic unit cells. PBC are imposed to the systems simulated in our molecular dynamics studies in Chapters 3, 4, 5.

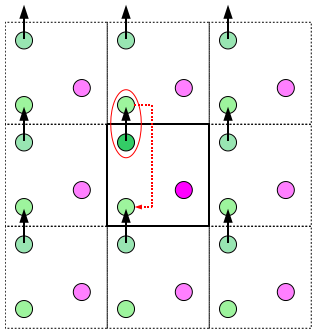

Figure II.1: Representation of Periodic Boundary Conditions in two dimensions.

II.5 Thermostats and Barostats

An ensemble is a collection of all possible systems that have differing microscopic states but belong to a single macroscopic or thermodynamic states. [38] Various different formal ensembles, characterized by the control of certain thermodynamic quantities, exist.

The **microcanonical ensemble** or **NVE** ensemble, is a thermodynamically isolated system in which the number of particles (N), the volume of the system (V) and the energy (E) are fixed. A different type of statistic ensembles are the thermodynamically non-isolated systems. The **canonical ensemble (NVT)** is a system in which the energy is exchanged with a thermal source and the number of particles (N), volume (V) and temperature (T) of the system are conserved.

Therefore the NVT ensemble is in thermal equilibrium with the heat source. The **isobaric-isothermal ensemble (NPT)** is a themodynamic state characterizes by a fixed number of atoms (N), fixed pressure (P), and fixed temperature (T). In MD simulations it is possible to realize thermodynamic ensembles which are characterized by a set of fixed and known thermodynamics variables. The Hamiltonian of an isolated system is time-independent, translationally invariant and rotationally invariant. Integration of the equations of motion for such a system leads to a trajectory mapping a microcanonical (NVE) ensemble. However, the NVE ensemble does not correspond to the conditions under which most experiments are performed. A *canonical* and *isobaric-isothermal* molecular dynamic simulations are more suitable representations of the reality because they perform systems which are coupled to a thermostat or to a barostat, to maintain constant respectively the temperature and pressure.
The temperature of the system T is related to the kinetic energy K by:

$$K = \sum_{i=1}^{N} = mi \mid v_i \mid^2 /2 = N_f K_b T/2 \tag{II.11}$$

N_f is the total number of degrees of freedom in the system, v_i the velocity of the particle i, and K_b the Boltzmann's constant. The temperature of the system T can thus be adjusted through the regulation of the velocity of particles. Different methods were proposed to fix the temperature to a fixed value during a simulation without allowing fluctuations of T [39, 40]. The **Berendsen** or **weak coupling method** [41] consists of an artificial 'thermostat' that rescales the coordinates and velocities at every time step depending on how far the system is away from the desired values for the temperature. For the Berendsen thermostat one assumes the change of the temperature depend only on the instantaneous value of the temperature with:

$$\frac{dT}{dt} = \frac{1}{\tau_T}(T_0 - T(t)) \tag{II.12}$$

with a characteristic time constant τ_T and the desired temperature T_0. The velocities of the particles in the system are then scaled by a factor λ:

$$\gamma = \sqrt{1 + \frac{\Delta t}{\tau_T}\left(\frac{T_0}{T} - 1\right)} \tag{II.13}$$

The Berendsen thermostat suppresses the fluctuations of the kinetic energy, because it enforce the total kinetic energy K to be equal to the average kinetic energy at the target temperature. This means that one does not generate a proper canonical ensemble. This error scales with $1/\mathrm{N}$, so for very large systems most ensemble averages will not be affected significantly, except for the distribution of the kinetic energy itself.

A similiar thermostat which produces a correct ensemble is the **Bussi-Donadio-Parrinello thermostat** known as **velocity rescaling thermostat** in GROMACS. [42]. In this thesis all the MD simulation have been performed using the Bussi-Donadio-Parrinello thermostat for the control of the temperature. This thermostat is an extension of the Berendsen thermostat with an additional stochastic term that ensures a correct kinetic energy distribution. Instead of forcing the kinetic energy to be exactly equal to the average kinetic, its target value is expressed by the canonical distribution for the kinetic energy, which is left invariant during the dynamics. The expression for the auxiliary dynamics is:

$$dK = (K_0 - K)\frac{dt}{\tau} + 2\sqrt{\frac{KK_0}{N_f}}\frac{dW}{\sqrt{\tau}} \tag{II.14}$$

where K is the kinetic energy, N_f is the number of degrees of freedom and dW a

Wiener process. Without considering the stochastic term the equation reduces to that of the standard thermostat of Berendsen.

The **Berendsen pressure coupling algorithm** is also a weak coupling scheme similar to the Berendsen temperature coupling [41]:

$$\frac{dP}{dt} = \frac{1}{\tau_p}(P_0 - P(t)) \tag{II.15}$$

where τ_p is the time constant for the coupling and P_0 is the reference pressure. A pressure change can be accomplished by rescaling the inter-particle distances, concomitant with a volume scaling. For this an extra term in the relation $\dot{x} = v$ is added proportional to x

$$\dot{x} = v_i + \alpha x \tag{II.16}$$

while the volume changes according to:

$$\dot{V} = 3\alpha V \tag{II.17}$$

The change of the pressure is connected to the compressibility β:

$$\frac{dP}{dt} = -\frac{1}{\beta V}\, dV dt = -\frac{3\alpha}{\beta} \tag{II.18}$$

Combining the equations II.18 with II.15, α can be expressed:

$$\alpha = -\frac{\beta(P_0 - P)}{3\tau_p} \tag{II.19}$$

Thus the modified equation of motion II.16 can be written as:

$$\dot{x} = v_i - \frac{\beta(P_0 - P)}{3\tau_p} x \tag{II.20}$$

For the case of an isotropic system in a cubic box this represents a proportional scaling of the coordinates and of the volume at each time step: the coordinates

are scaled by a factor of μ, and the volume is scaled by a factor of μ^3. As results the factor scaling μ is given by:

$$\mu = \left[1 - \beta\frac{\Delta t}{\tau_P}(P_0 - P)\right]^{1/3} \tag{II.21}$$

For an anisotropic triclinic system the pressure P becomes a tensor and the volume V is the determinant of a matrix μ formed by the a, b, c lattice vectors.

II.6 Potential of Mean Force

The **Potential of Mean Force (PMF)** is an important concept in molecular dynamics, first introduce by Kirkwood in 1935. [43] When examining a system computationally one may be interested to know how the free energy changes as a function of some inter or intramolecular coordinate (such as the distance between two atoms or a torsional angle). The Potential of Mean Force $W(\xi)$ describes the change in free energy along a reaction coordinate (ξ). It is defined from the probability to observe the system at the stare $\xi, < \rho(\xi) >$,

$$W(\xi) = W(\xi^*) - K_B T ln\left[\frac{< \rho(\xi) >}{< \rho(\xi^*) >}\right], \tag{II.22}$$

where ξ^* and $W(\xi)^*$ are arbitrary reference values. The average distribution function along the coordinate is obtained from a Boltzmann weighted average.

$$< \rho(\xi) >= \frac{\int dR\delta(\xi^{'}[R] - \xi)e^{-U(R)/K_B T}}{\int dRe^{-U(R)/K_B T}} \tag{II.23}$$

where U(R) represents the total energy of the system as a function of the coordinates R, $\delta(\xi^{'}[R] - \xi)$ is the Dirac delta function for the coordinate R and $\xi^{'}[R]$ is a function depending on the degree of freedom of the dynamical system

($\xi'[R]$ may be an angle, a distance, or a more complicated function of cartesian coordinate of the system).

It is impractical to compute the PMF $W(\xi)$ or the distribution function $< \rho(\xi) >$ directly from a straight molecular dynamics simulation. For example the presence of large energy barriers along ξ may prevent an accurate sampling of the configurational space within the available time. To avoid such difficulties, special sampling techniques have been designed to calculate the PMF from a molecular dynamics trajectory effectively.

In this thesis we calculated the potential of mean force (or free/Gibbs energy) to measure the strength of adsorption of ionic and non-ionic surfactants at poly(styrene)-water and styrene-water interfaces by integrating the average constraint force as a function of the constrained distance d_c, between polystyrene or styrene and a surfactant.

The **pull-code** in Gromacs is used to prepare the starting conformations for the potential of mean forces (PMF). The code applies constraints between the center of mass, or atom, of one or more pairs of atoms. The most common situation consists of a reference group and one pull group. The distance between the pair of groups can be determined along one dimension or along a vector defined by the user. The reference distance is constant. The constraint pulling method uses the SHAKE algorithm to calculate the constraint force. Therefore, given the constraint equation (II.10) at every time t, the forces due to the constraint are added in the equation of motion (see Equation II.8). Adding the constraint forces does not change the total energy, as the work done by the constraint forces (taken over the reference and pull groups that the constraints act on) is zero. To obtain the PMF (or free/Gibbs energy profile), the average force is integrated as a function of the constrained distance.

Error Estimation

The estimations of the errors of the free energy changes were obtained from, [44]

$$\delta\Delta G = \left[\sum_{d_c=0}^{d_{c,max}} (\delta < \partial\mathcal{H}/\partial d_c >)^2 \right]^{1/2} \tag{II.24}$$

where $\mathcal{H}$ is the perturbed Hamiltonian (the sum of potential and kinetic energy terms) and $\delta < \partial\mathcal{H}/\partial d_c >$ is the error in determining the average force at each constrained distance. The value of $\delta < \partial\mathcal{H}/\partial d_c >$ is evaluated by the block averaging method. [45]

II.7 Radial Distribution Functions

The absence of a permanent structure in a fluid means that every atom (or molecule) has around it a continuous reorganization of molecules. The function that is used to describe the average structure of a fluid is the **Radial Distribution Function (RDF)**, defined as the probability of finding a pair of atoms i and j at a distance r_{ij} relative to the probability at the random distribution. The RDF is denoted as $g(r_{ij})$ by the equation:

$$g(r_{ij}) = \frac{V}{N^2} \left\langle \sum_i \sum_{j \neq i} \delta(r - r_{ij}) \right\rangle \tag{II.25}$$

where N and V are respectively the number of the particles and the volume of the fluid, $\delta(r - r_{ij})$ is the Dirac delta function. The RDF is strongly dependent on the type of matter. Due to their dynamical motion, liquids are not characterized by a long-ranged structure. Any structural correlation is normally lost beyond the third solvation shell. The first coordination shell for a liquid will occur at $\sim \sigma_{ij}$, and is represented by the first and sharpest pick of the Radial Distribution Function (see Figure II.2). At large values of r, the molecules

become independent of each other, and the distribution undulates around the value of g(r)=1. Thus the subsequent peaks will be smaller than the first and will occur roughly in intervals of σ_{ij}.

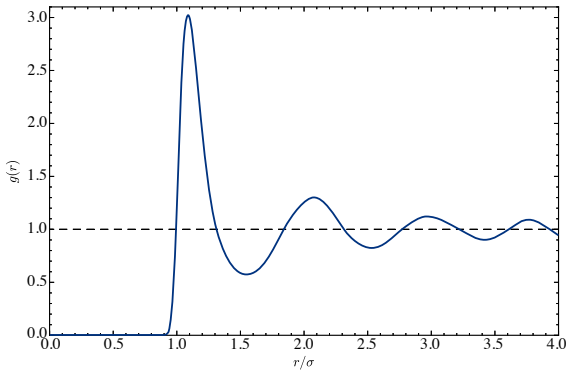

Figure II.2: Radial distribution function for the Lennard-Jones model fluid.

The coordination number (NC) indicates how many molecules are found in the range of each coordination sphere. The NC is given by integrating $g(r)$, in spherical coordinates, to the first minimum of the Radial Distribution Functions:

$$NC(r') = 4\pi\rho \int_0^{r'} g(r) r^2 dr \tag{II.26}$$

II.8 Hydrogen Bonding

Hydrogen bonds is a medium strength attractive intermolecular or intramolecular force. Hydrogen bond occurs between a partially positively charged hydrogen atom, attached to a highly electronegative atom (hydrogen bond donor), and another nearby electronegative atom (hydrogen bond acceptor). The electronegative atoms are usually oxygen, nitrogen, or fluorine. In this thesis a donor-acceptor distance cutoff, smaller than 0.35 nm, and a donor-hydrogen-acceptor

angle, larger than 150°, are used as the geometrical criteria to determine the hydrogen bonds.

References

[1] Allen, M. P.; others. Introduction to molecular dynamics simulation, *Computational soft matter: from synthetic polymers to proteins* 2004, *23*, 1–28.

[2] Petrenko, R.; Meller, J. Molecular dynamics, *e LS* 2001.

[3] Berendsen, H. J. *Simulating the physical world: hierarchical modeling from quantum mechanics to fluid dynamics;* Cambridge University Press, 2007.

[4] Gromacs user manual version 4.5. 6, see www. gromacs. org, 2010. van der Spoel, D.; Lindahl, E.; Hess, B.; van Buuren, A.; Apol, E.; Meulenhoff, P.; Tieleman, D.; Sijbers, A.; Feenstra, K.; van Drunen, R.; others.

[5] Swope, W.; Andersen, H. Berens ph and wilson kr, *J. Chem. Phys.* 1982, *1982*, 76.

[6] Beeman, D. Some multistep methods for use in molecular dynamics calculations, *J. Comput. Phys.* 1976, *20*, 130–139.

[7] Verlet, L. Computer "experiments" on classical fluids. i. thermodynamical properties of lennard-jones molecules, *Phys. Rev.* 1967, *159*, 98–103.

[8] Hess, B.; Kutzner, C.; Van Der Spoel, D.; Lindahl, E. Gromacs 4: algorithms for highly efficient, load-balanced, and scalable molecular simulation, *J. Chem. Theory Comput.* 2008, *4*, 435–447.

[9] Hockney, R.; Goel, S.; Eastwood, J. Quiet high-resolution computer models of a plasma, *J. Comput. Phys.* 1974, *14*(2), 148–158.

[10] Ponder, J. W.; Case, D. A. In *Advances in protein chemistry*, Vol. 66; Elsevier, 2003; pages 27–85.

[11] Meconi, G. M.; Ballard, N.; Asua, J. M.; Zangi, R. Adsorption and Desorption Behavior of Ionic and Nonionic Surfactants on Polymer Surfaces, *Soft Matter* 2016, *12*, 9692–9704.

[12] Meconi, G. M.; Ballard, N.; Asua, J. M.; Zangi, R. Shedding light on the different behavior of ionic and nonionic surfactants in emulsion polymerization: from atomistic simulations to experimental observations, *Phys. Chem. Chem. Phys.* 2017, *19*, 31692–31705.

[13] Potoff, J. J.; Siepmann, J. I. Vapor-liquid equilibria of mixtures containing alkanes, carbon dioxide, and nitrogen, *AIChE J.* 2001, *47*, 1676–1682.

[14] Yang, J.; Ren, Y.; Tian, A.-m.; Sun, H. COMPASS Force Field for 14 Inorganic Molecules, He, Ne, Ar, Kr, Xe, H_2, O_2, N_2, NO, CO, CO_2, NO_2, CS_2, and SO_2, in Liquid Phases, *J. Phys. Chem. B* 2000, *104*, 4951–4957.

[15] Harris, J. G.; Yung, K. H. Carbon Dioxide's Liquid-Vapor Coexistence Curve And Critical Properties as Predicted by a Simple Molecular Model, *J. Phys. Chem.* 1995, *99*, 12021–12024.

[16] Murthy, C.; Singer, K.; Klein, M.; McDonald, I. Pairwise Additive Effective Potentials for Nitrogen, *Mol. Phys.* 1980, *41*, 1387–1399.

[17] Walther, J. H.; Jaffe, R.; Halicioglu, T.; Koumoutsakos, P. Carbon Nanotubes in Water: Structural Characteristics and Energetics, *J. Phys. Chem. B* 2001, *105*, 9980–9987.

[18] Brooks, B. R.; Bruccoleri, R. E.; Olafson, B. D.; States, D. J.; Swaminathan, S.; Karplus, M. CHARMM: a program for macromolecular energy, minimization, and dynamics calculation, *J. Comp. Chem.* 1983, *4*, 187–217.

[19] Biomolecular simulation: the {GROMOS96} manual and user guide. van Gunsteren, W. F.; Billeter, S. R.; Eising, A. A.; Hünenberger, P. H.; Krüger, P.; Mark, A. E.; Scott, W. R.; Tironi, I. G. 1996.

[20] Weiner, S. J.; Kollman, P. A.; Case, D. A.; Singh, U. C.; Ghio, C.; Alagona, G.; Profeta, S.; Weiner, P. A new force field for molecular mechanical simulation of nucleic acids and proteins, *J. Am. Chem. Soc.* 1984, *106*(3), 765–784.

[21] Jorgensen, W. L.; Maxwell, D. S.; Tirado-Rives, J. Development and testing of the opls all-atom force field on conformational energetics and properties of organic liquids, *J. Am. Chem. Soc.* 1996, *118*(45), 11225–11236.

[22] Jorgensen, W. L.; Tirado-Rives, J. The OPLS potential functions for proteins. Energy minimizations for crystals of cyclic peptides and crambin, *J. Am. Chem. Soc.* 1988, *110*, 1657–1666.

[23] Jorgensen, W. L.; Tirado-Rives, J. Potential energy functions for atomic-level simulations of water and organic and biomolecular systems, *Proc. Natl. Acad. Sci. U.S.A.* 2005, *102*(19), 6665–6670.

[24] Allen, M. P.; Tildesley, D. J. *Computer Simulations of Liquids;* Oxford Science Publications: Oxford, 1987.

[25] Sambasivarao, S. V.; Acevedo, O. Development of opls-aa force field parameters for 68 unique ionic liquids, *J. Chem. Theory Comput.* 2009, *5*(4), 1038–1050.

[26] Sadus, R. J. *Molecular simulation of fluids: theory, algorithms, and object-orientation;* Elsevier, 2002.

[27] Qiao, R.; Aluru, N. Ion concentrations and velocity profiles in nanochannel electroosmotic flows, *J. Chem. Phys.* 2003, *118*(10), 4692–4701.

[28] Joseph, S.; Aluru, N. Hierarchical multiscale simulation of electrokinetic transport in silica nanochannels at the point of zero charge, *Langmuir* 2006, *22*(21), 9041–9051.

[29] Kim, D.; Darve, E. Molecular dynamics simulation of electro-osmotic flows in rough wall nanochannels, *Physical review E* 2006, *73*(5), 051203.

[30] Frenkel, D.; Smit, B. *Understanding molecular simulation: from algorithms to applications*, Vol. 1; Elsevier, 2001.

[31] Allen, M. P.; Tildesley, D. J. *Computer simulation of liquids;* Oxford university press, 2017.

[32] Andersen, H. C. Rattle: A "velocity" version of the shake algorithm for molecular dynamics calculations, *J. Comput. Phys.* 1983, *52*(1), 24–34.

[33] Hess, B.; Bekker, H.; Berendsen, H. J. C.; Fraaije, J. G. E. M. LINCS: A Linear Constraint Solver for Molecular Simulations, *J. Comp. Chem.* 1997, *18*, 1463–1472.

[34] Ryckaert, J.-P.; Ciccotti, G.; Berendsen, H. J. Numerical integration of the cartesian equations of motion of a system with constraints: molecular dynamics of n-alkanes, *J. Comput. Phys.* 1977, *23*(3), 327–341.

[35] Miyamoto, S.; Kollman, P. A. SETTLE: An Analytical Version of the SHAKE and RATTLE Algorithms for Rigid Water Models, *J. Comp. Chem.* 1992, *13*, 952–962.

[36] Bergdorf, M.; Peter, C.; Hünenberger, P. H. Influence of cut-off truncation and artificial periodicity of electrostatic interactions in molecular simulations of solvated ions: A continuum electrostatics study, *J. Chem. Phys.* 2003, *119*(17), 9129–9144.

[37] Weber, W.; Hünenberger, P. H.; McCammon, J. A. Molecular dynamics simulations of a polyalanine octapeptide under ewald boundary conditions: influence of artificial periodicity on peptide conformation, *J. Phys. Chem. B* 2000, *104*(15), 3668–3675.

[38] McQuarrie, D. A. *Statistical Mechanics;* University Science Books: Mill Valley, 1976.

[39] Nosé, S. A molecular dynamics method for simulations in the canonical ensemble, *Mol. Phys.* 1984, *52*(2), 255–268.

[40] Hoove, W. G. Canonical dynamics: Equilibrium phase-space distributions, *Phys. Rev. A* 1985, *31*, 1695–1697.

[41] Berendsen, H. J.; Postma, J. v.; van Gunsteren, W. F.; DiNola, A.; Haak, J. Molecular dynamics with coupling to an external bath, *J. Comput. Phys.* 1984, *81*(8), 3684–3690.

[42] Bussi, G.; Donadio, D.; Parrinello, M. Canonical Sampling through Velocity Rescaling, *J. Chem. Phys.* 2007, *126*, 014101.

[43] Kirkwood, J. G. Statistical Mechanics of Fluid Mixtures, *J. Chem. Phys.* 1935, *3*, 300–313.

[44] Guàrdia, E.; Rey, R.; Padró, J. A. Statistical Errors in Constrained Molecular Dynamics Calculations of the Mean Force Potential, *Mol. Sim.* 1992, *9*, 201–211.

[45] Flyvbjerg, H.; Petersen, H. G. Error Estimates on Averages of Correlated Data, *J. Chem. Phys.* 1989, *91*, 461–466.

Chapter III

Adsorption and Desorption Behavior of Ionic and Nonionic Surfactants on Polymer Surfaces

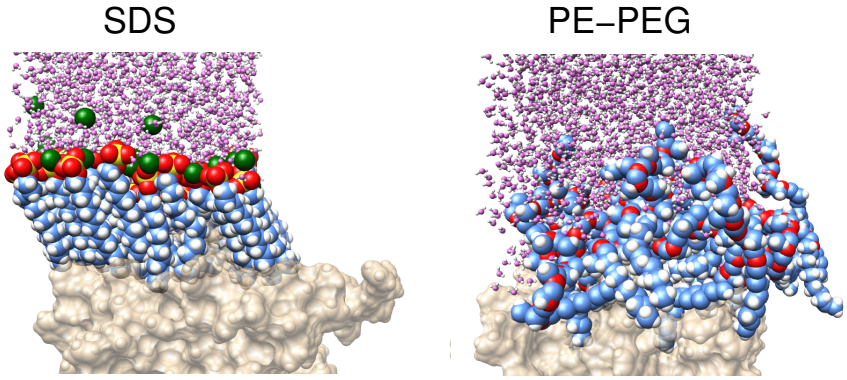

Contents

The results in this Chapter were published in:
Giulia Magi Meconi, Nicholas Ballard, José M. Asua and Ronen Zangi,
Adsorption and Desorption Behavior of Ionic and Nonionic Surfactants on Polymer Surfaces,
Soft Matter **2016**, 12, 9692-9704.
doi: 10.1039/C6SM01878E.

III.1 Introduction

In this chapter we seek to take a deeper look at how surfactants interact with polymer surfaces, so that we better understand their effects on the emulsion polymerization process. As a model for ionic surfactants we consider sodium dodecyl sulfate (SDS) and for nonionic surfactants block copolymers of poly(ethylene oxide) (PEO) and poly(ethylene) (PE). These are among the most abundantly used surfactants, in general, and in emulsion polymerization in particular. Using quartz crystal microbalance with dissipation monitoring (QCM-D) we find that, at low surfactant concentrations, it is easier to desorb (as measured by the rate) ionic surfactants than nonionic surfactants. To the best of our knowledge this phenomenon has never been addressed before and no explanation for the difference in the behavior of the adsorption/desorption between ionic and nonionic surfactants has been proposed. In order to rationalize this observation we perform molecular dynamics (MD) simulations and calculate the reversible work necessary to remove one of these surfactants from the surface. Here we find that the work increases as the concentration of the nonionic surfactants at the surface decreases. In contrast, for ionic surfactants a moderate augmentation of the work is obtained with an increase in concentration. The reason for this opposing behavior is that with increasing concentration, the nonionic surfactants at the surface are increasingly less stable whereas no such destabilization is observed for ionic surfactants. We attribute these different trends to the physio-chemical properties of the head groups and to the self-organization structure of the adsorbed surfactants.

III.2 Experimental

III.2.1 Experimental Details

Materials

Technical grade styrene (styrene, Quimidroga) were used as received. Sodium dodecyl sulfate (>99.5%, Aldrich) was recrystalized from an ethanol/water mixture, potassium persulfate (99%, Aldrich), poly(styrene) (Mw = 280000 g/mol, Aldrich) and Disponil AFX 1080 (a 10PEO6PE block copolymer, 80% active content, BASF) were used as received. Doubly deionized water was used throughout the work.

Latex Characterization

Z-average particle diameters were determined by dynamic light scattering performed on a Malvern Zetasizer ZS using a scattering angle of 173 ° at a standard temperature of 25 °C. Each measurement was conducted in triplicate and the average of the three values was taken. Conversion was determined gravimetrically.

Latex Preparation

Water (757 g), SDS (4 g) and styrene (135 g) were added to a 1 L double walled glass reactor equipped with anchor type stirrer, nitrogen inlet, condenser and thermocouple. The reaction mixture was degassed by nitrogen bubbling for 30 minutes, stirring constantly at 300 rpm, and then heated to 70 °C. Once at

reaction temperature, sodium persulfate (225 mg dissolved in 8 g water) was added in a single shot. After 6 hours, the reaction mixture was cooled and filtered through a muslin lining to remove any aggregates. The final conversion of the latex was 96% as determined gravimetrically. The latex was dialyzed until a constant conductivity was obtained. The solids content after dialysis was 13.9 wt% with a mean particle diameter of 76 nm and a polydispersity index (PDI) of 0.07.

Latex Soap Titration

The CMC and the surface area per molecule (packing area), a_s, of the surfactants were determined by means of surface tension measurements at 23 °C using a Du Noüy ring (KSV Sigma 70, KSV Instruments Ltd.) equipped with automatic dosing unit. The diluted latex or DDI water (40 g) were titrated with surfactant solutions measuring the surface tension at various concentration intervals. Multiple measurements at each point were taken and an average was taken.

Quartz Crystal Microbalance

Polymer coated sensors were obtained by spin coating a solution of poly(styrene) (PS) (Mw = 280000 g/mol, 0.5 wt% in toluene) onto a gold sensor (Diameter = 14 mm, Q-SENSE, Sweden) at a rate of 50 rps for 1 minute using a Lot Oriel SCC 200 spin coater. The coated thickness was typically 25 nm as measured by difference in frequency before and after coating using the Sauerbrey relationship. [1] The sensors were then placed in an oven at 130 °C for one hour. QCM measurements were performed on a Q-SENSE E1 system operating at

23 °C. Before experiments DDI water was passed over the chip until a stable baseline was obtained. All solutions were passed at a rate of 150 μl/min using a peristaltic pump. The resonance frequency and dissipation were monitored throughout the experiment at an approximate rate of 1 Hz. Kinetic experiments were conducted by flowing a concentration of surfactant through the QCM for a set period of time (typically 500 seconds). The desorption part of the experiment was then conducted by changing the test solution to deionized water. The QCM-D technique detects changes in the resonance frequency, Δf, and dissipation, ΔD. During the adsorption/desorption cycle the resonance frequency of the crystal changes according to changes in mass. If the mass forms an evenly distributed, rigid layer whose mass is small compared to that of the crystal then the mass per unit area, m, can be calculated from the Sauerbrey equation, [1]

$$\Delta m = \frac{-C\Delta f}{n} \tag{III.1}$$

where C is a constant (17.7 ng·cm^{-2} · s^{-1} in this equipment) and n is the resonance overtone number. In this work, n=5 was used unless otherwise stated. By monitoring the dissipation of the sensor's oscillation, information about the nature of the surface layer can be extracted. The dissipation is defined as,

$$D = \frac{E_{dis}}{2\pi E_{st}} \tag{III.2}$$

where E_{dis} is the energy dissipated during a single cycle and E_{st} is the total energy stored. A large change in D represents a large energy dissipative power of the adsorbed layer and is usually due to thick or less rigid layers. For non-rigid adsorbed layers the Sauerbrey equation results in an underestimation of adsorbed mass since the oscillation of the sensor surface and the film are not fully coupled. In order to account for viscoelastic behavior of the adsorbed layer the Voigt model can be employed using the measured dissipation. To model

the viscoelastic properties, four overtones (fifth, seventh, ninth and eleventh) were used and the adsorbed mass calculated using the Voigt model (Q-TOOLS software, Q-Sense, Goeteborg, Sweden). The layer density, fluid viscosity and fluid density were fixed at 1000 kg/m^3, 0.001 kg/m/s 1000 kg/m^3 respectively. The layer viscosity, layer shear and layer thickness were fitted in order to calculate the adsorbed mass.

III.2.2 Computational Details

Rectangular-shaped boxes, with periodic boundary conditions in all three dimensions, were employed for the simulations. The starting configuration was a pre-equilibrated (for approximately 100 ns) PS slab, placed in the xy-plane, on which surfactants with extended conformation (their long-axis normal, and their tails pointing, to the surface) were arranged in a square lattice. The box lengths in the x- and y-directions were equal and always large enough to ensure absence of interactions of the surfactants with their periodic images. The box length along the normal to the surface direction (z-axis) was elongated to allow a surfactant to be pulled away from the surface to a distance where no effective interactions with either the surface or other surfactants were observed. Then, the region in the simulation box which does not include the PS was filled with water. The resulting systems were subject to a relaxation time of 40 ns and 16 ns for the SDS and PEO-PE surfactants, respectively. Table A I.1 in Appendix I specifies the details of all systems considered in this work. Note that we choose to present the state of the system by the two-dimensional density, $\rho_{2D} = \mathrm{m}/\mathrm{A}$, where m is the mass of the surfactants and A is the area of the simulation box in the xy-plane.

The molecular dynamics package GROMACS, version 4.6.5, [2] was used to perform all computer simulations. A temperature of 300 K was maintained by the velocity rescaling thermostat, [3] pertained to the whole system, with a coupling time of 0.1 ps. The pressure in the xy-plane was maintained at 1.0 bar by the Berendsen barostat, [4] using a compressibility of $1{\cdot}10^{-6}$ 1/bar and a coupling time of 1.0 ps, whereas, the box length along the z-axis was fixed. The electrostatic forces were evaluated by the Particle-Mesh-Ewald method [5, 6] with a real-space cutoff of 0.9 nm and a grid spacing for the reciprocal-space

of 0.12 nm with quadratic interpolation. A 0.9 nm cutoff was also used to calculate the Lennard-Jones potential (with long range dispersion corrections for the energy and pressure). Equilibration stages that did not use constraints were performed with a time step of 2 fs. However, application of the distance constraint within the pull-code (see below) resulted in occasional instabilities. These instabilities disappeared upon reduction of the time step to 1 fs. Thus, whenever the application of a constraint was necessary, a 1 fs time step was used. PS and the surfactants were represented by an explicit-hydrogen all-atom model based on the OPLSAA force-field. In Appendix I we provide a detailed description, Figure A I.1– A II.16 and Table A I.2– A II.11 , explanation, and validation of the parameters used.

Water molecules were described by the TIP4P-Ew model. [7] Tang et al. [8] reported that the structure of the aggregate of 300 or more SDS surfactants at high concentration can depend on the water model used. Therefore, we also performed few simulations of the SDS system with the SPC/E water model. [9] However, we did not observe any substantial difference in the behavior of the surfactants compared with the simulations with the TIP4P-Ew water molecules (see Figure A I.7).

Water bond distances and angles were constrained using the SETTLE algorithm, [10] however, no constraints were applied for the bonded interactions of the surface or surfactant molecules. Hydrogen bonds were calculated by a donor–acceptor distance cutoff smaller than 0.35 nm and donor–hydrogen–acceptor angle cutoff larger than 150°. [11] Ion contacts were calculated by the sodium–oxygen (of SDS) distance cutoff smaller than the first minimum in the corresponding radial distribution function which was found to be 0.32 nm.

Potentials of Mean Force Calculations

In order to prepare starting conformations for the potential of mean force (PMF), we utilized the pull-code in Gromacs. More specifically, constraint-pulling along the z-axis with cylindrical geometry, was employed with a rate in the range of $1{\cdot}10^{-4}$ – $5{\cdot}10^{-2}$ nm/ps. The reference-group was the center of mass of a cylindrical cut of the surface around the pull-vector, and the pull-group was a carbon atom of the hydrophobic tail of the surfactant covalently bonded to the oxygen atom of the hydrophilic head (see Figure A II.17 and Figure A II.16 in Appendix I). Then, for several chosen distances along the reaction coordinate, we equilibrated the system for a time period in the range of 14 ns to 50 ns (depending on the time the system reached convergence) keeping these distances fixed throughout the simulation. The average force that was required to constrain the distance between the reference and the pull groups was calculated in a data collection step of additional 12 ns. However, at points in which the average force did not exhibit convergence the data collection step was extended to 36 ns. The reason that different points along the reaction coordinate require different equilibration (relaxation) and data-collection times is because of a difference in the interaction of the constrained degree of freedom with its environment. A case in which a longer equilibration time and a longer data collection segment were needed is shown Figure A I.4 in Appendix I. To obtain the PMF (or free/Gibbs energy profile), this average force was integrated as a function of the constrained distance, d_c. Because the PMF represents only relative values, it was shifted such that the Gibbs energy of the state at the largest separation corresponds to zero. Furthermore, the distances were also shifted such that the interface between the PS and water is at d_c=0.0 nm.

III.3 Results and Discussion

III.3.1 Titration and QCM-D Experiments

The adsorption isotherms of the anionic surfactant, sodium dodecyl sulfate, and the nonionic Disponil AFX 1080, a 10PEO-6PE block copolymer, were identified experimentally by surface tension measurements using a Du Noüy ring tensiometer. These two surfactants represent typical surfactant systems applied in emulsion polymerization. A thoroughly dialyzed PS latex produced by emulsion polymerization with solids content of 13.9 wt% and average particle diameter of 76 nm was titrated with the two surfactants and the variation in the surface tension with increasing surfactant concentration was observed for several latex particle concentrations (see Figure III.1).

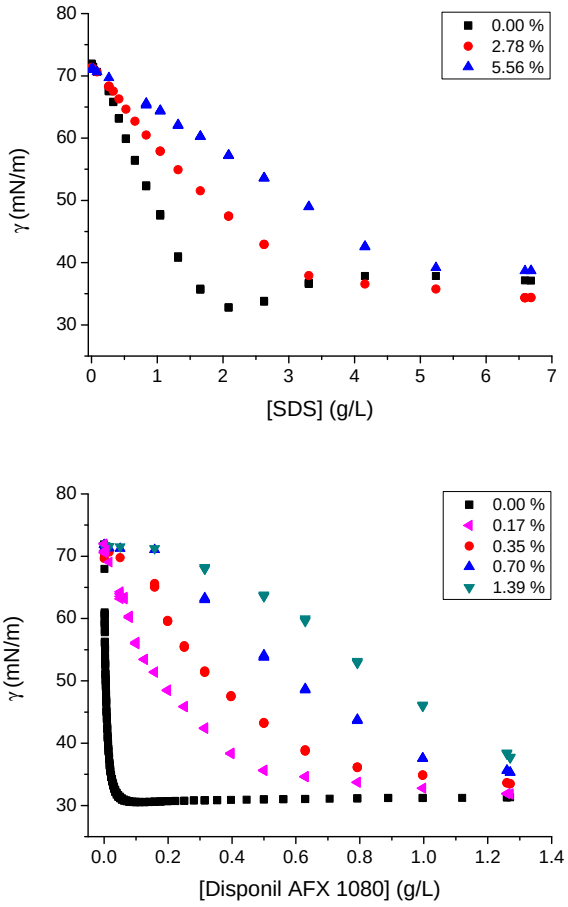

Figure III.1: Variation of surface tension with increasing bulk concentration of SDS and Disponil AFX 1080 for different solid content of the poly(styrene) latex as shown in the figure legends.

Qualitatively, two key points can be taken from the titration experiments shown in Figure III.1. First, the critical micelle concentration, as determined by the concentration at which the surface tension reaches a constant value in the absence of latex particles, is considerably lower for the nonionic surfactant. The CMC for SDS is 2.3 g/L while that of Disponil AFX 1080 is 0.05 g/L. These values are in reasonable agreement with previous experimental studies. [12] Second, for the nonionic surfactant, the presence of even small quantities of latex particles results in significant surfactant adsorption thus resulting in a large difference in the measured surface tension for a given amount of surfactant added. This behavior can be analyzed quantitatively from the adsorption isotherms which can be derived based on the assumption that a given surface tension value of the air-water interface is directly related to the equilibrium surfactant concentration in the aqueous phase, $[S]_{aq}$. Assuming that the amount of surfactant adsorbed at the air-water interface is negligible compared with the amount adsorbed on the latex particles (due to the large difference in the surface area of both interfaces), from a mass balance, the total surfactant concentration [S], is equal to the sum of $[S]_{aq}$ and the amount of adsorbed emulsifier,

$$[S] = [S]_{aq} + \Gamma \frac{A_p}{V_{aq}} \tag{III.3}$$

where A_p is the total surface area of the latex particles, V_{aq} is the volume of the aqueous phase and Γ is the amount of adsorbed emulsifier per unit area of latex. The value of $[S]_{aq}$ can be calculated from the curves in Figure III.1 from the value of the air-water surface tension and interpolation of the curve in the absence of latex, assuming that a given surface tension corresponds to a given $[S]_{aq}$. The value of Γ can be calculated accordingly. This analysis allows the construction of the adsorption isotherms shown in Figure III.2.

The isotherms for the two surfactants were fit either to the Langmuir isotherm (Disponil AFX 1080),

$$\Gamma = \Gamma_\infty \frac{K[S]_{aq}}{1 + K[S]_{aq}} \quad , \tag{III.4}$$

or the Frumkin isotherm [13] (SDS),

$$\frac{\Gamma/\Gamma_\infty}{1 - \Gamma/\Gamma_\infty} \, e^{[2a \cdot \Gamma/\Gamma_\infty]} = K[S]_{aq} \quad , \tag{III.5}$$

where Γ_∞ is the maximum quantity of surfactant that can be adsorbed, K is the adsorption constant and a is an adjustable parameter associated with molecular interactions. The use of the Frumkin isotherm was necessary for the SDS data as it shows a more S-like pattern which is not accounted for by the standard Langmuir isotherm indicating some cooperativity in the adsorption profile, as has previously been observed for the adsorption of SDS on hydrophobic polymer surfaces. [14–16]

A summary of the resulting equilibrium constants and packing area of the surfactant molecules at the PS surface at the CMC a_{CMC} are shown in Table III.1. The value of a_{CMC} was calculated from Equation III.4 or III.5 using for a value

Table III.1: Estimated values of the parameters obtained from fit of the modified Langmuir isotherm to the data shown in Figure III.2.

	K [m^3/mol]	a_{CMC} [Å^2]
SDS	0.064 ± 0.002	29 ± 5
Disponil AFX 1080	7.4 ± 1.2	24 ± 9

of $[S]_{aq}$ equal to the CMC of each surfactant. It is clear that the equilibrium constant for the nonionic surfactant is significantly higher than that of SDS, in agreement with previous experimental data. [15, 17, 18] In both cases the

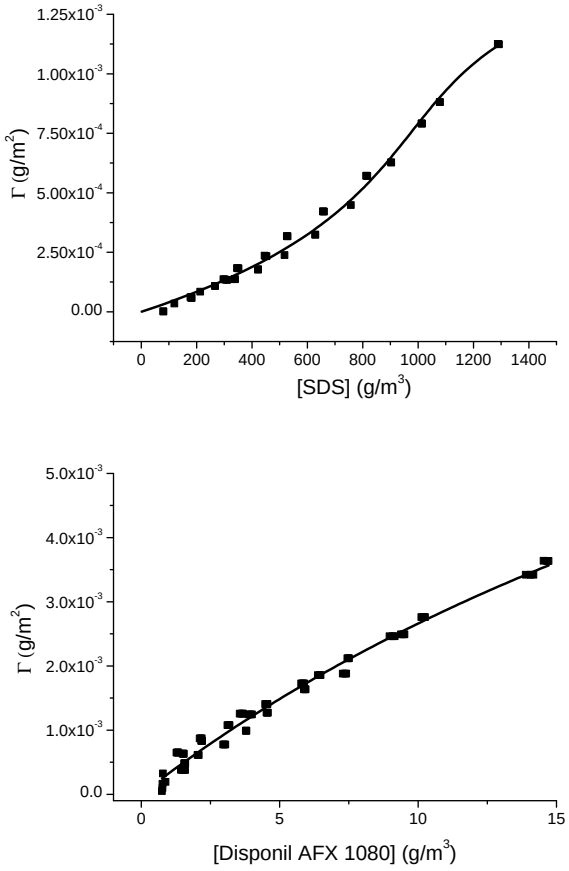

Figure III.2: Adsorption isotherms of SDS and Disponil AFX 1080 onto poly(styrene). Lines represent fit of the experimental data to the Langmuir or Frumkin isotherm as detailed in the text.

absolute value of a_{CMC} is slightly lower than some previous experimental results using polystyrene surfaces obtained by spin-coating and scattering techniques to measure surfactant adsorption. [19] However, measurements using latex particles have given values similar to those reported here for the adsorption of SDS on polystyrene surfaces, suggesting that surface roughness in polymer latexes may result in an underestimation of the total surface area and consequently affect estimates of a_{CMC} and K. For example, Brown and Zhao [20] conducted experiments using polystyrene latex particles of 200 nm and found a packing area of 30 $Å^2$ which compares very favorably with our results. They also observed a very similar adsorption isotherm to that of the present case with a tendency to increase the strength of adsorption with increasing surface density. For the non-ionic surfactant the lack of literature data makes comparison difficult but in comparison to other PEO-PE surfactants which typically have area of 50–70 $Å^2$ the value obtained here seems significantly lower. [21–24] One possible reason for this is that PEO-PE surfactants typically contain a broad distribution of chain lengths with varying numbers of ethylene glycol units. Small quantities of molecules with very few ethylene glycol units can have a huge impact on adsorption behavior. For example, Turner et al. showed that the presence of residual dodecanol in recrystallized SDS results in a measurement of almost twice the surface concentration compared to highly purified SDS. [19]

One important point that has been highlighted recently is how the strength of surfactant adsorption can also impact on nucleation events in emulsion polymerization. [15, 18] In order to further explore this and to investigate the reversibility of surfactant adsorption at varying concentrations the QCM-D technique was used. The QCM equipment is capable of measuring small changes in surface concentration and was used in a series of experiments in which a PS surface was sequentially subjected to water and surfactant solution to monitor adsorption

and desorption from the surface. In order to convert the measured change in frequency to a mass per unit area the Sauerbrey relation was used, which is based on the assumption that the adsorbed surfactant layer is rigid. Whilst for SDS this assumption is valid, as confirmed by the similar values obtained for the amount of surfactant adsorbed in comparison to the surface tension measurements shown in Figure III.2, for the non-ionic surfactant, the PEO part of the chain is hydrated and therefore leads to viscoelastic behavior of the adsorbed layer. In this case the mass adsorbed was calculated using the Voigt model which takes into account the viscoelasticity through the relationship of the measured frequency and energy dissipation at a number of resonance frequencies.

Figure III.3 shows the plot of the amount of surfactant adsorbed to the surface with time when subjected to surfactant solution (shown in grey areas), at around the CMC of each surfactant, and water.

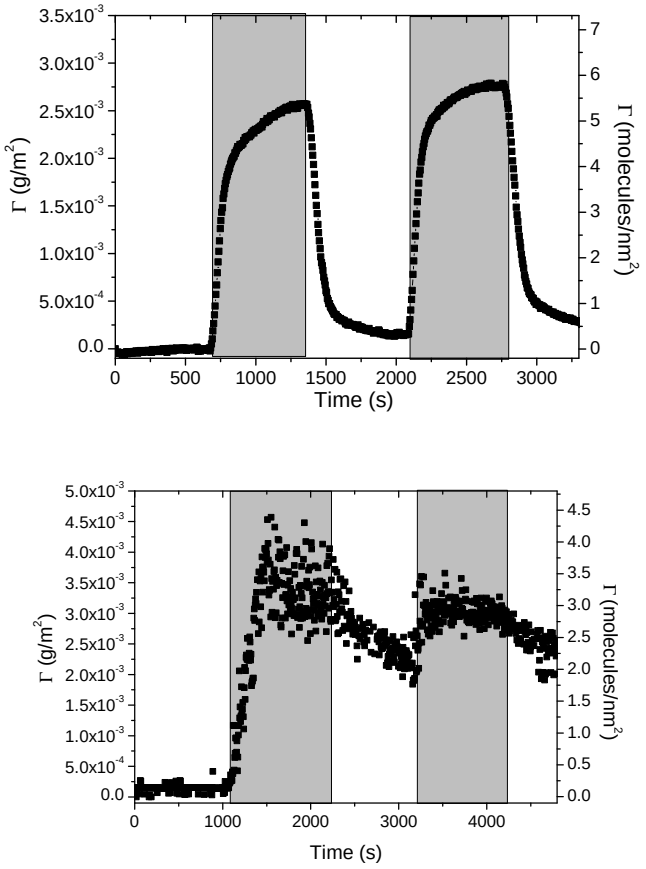

Figure III.3: Adsorption of SDS (left panel) and Disponil AFX 1080 (right panel) onto poly(styrene) measured by QCM-D. Initially water is flown through the cell followed by two cycles of either SDS (1.8 g/L) or Disponil AFX 1080 (0.02 g/L). Shaded regions correspond to time periods in which the surfactant solution is being passed over the polymer surface.

It can be observed that after adsorption, SDS is rapidly removed from the surface when the surfactant solution is replaced with water.
In the case of the nonionic surfactant, however, upon flowing water through the cell the surfactant is very slow to be removed.
Previous work by Ballard et al. has shown that this is a common occurrence for nonionic surfactants when adsorbed to polymer surfaces and was previously attributed to the a change in the strength of adsorption as a function of the surface coverage of the surfactant such that at low concentration the nonionic surfactant is strongly bound. [18]

III.3.2 Potentials of Mean Force Calculations

In order to explain the experimental observations we studied the strength and nature of surfactant adsorption at polymer surfaces using molecular dynamics simulations. The strength of the adsorption was calculated by measuring the Gibbs (free) energy required to pull a surfactant adsorbed at the PS–water interface to the bulk water phase. In order to display the behavior of the systems at equilibrium (thus, at zero pull-force and when all surfactants are adsorbed) for the different 2D-densities studied, we plot in Figure III.4 the density profiles normal to the PS–water interface.

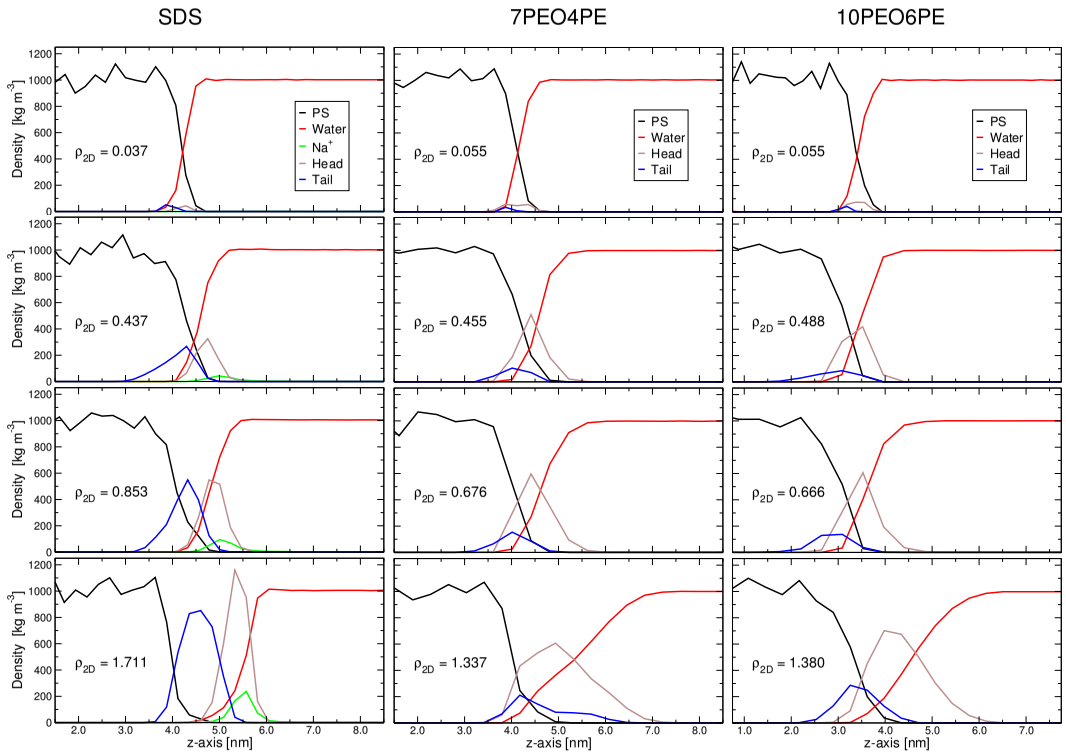

Figure III.4: Density profiles perpendicular to the PS-water interface at different surfactant two-dimensional densities. Left, middle and right panels are for SDS, 7PEO4PE and 10PEO6PE surfactants, respectively. Each surfactant is divided into a hydrophilic head and a hydrophobic tail as defined in Figure A II.17 and Figure A II.16 in Appendix I. Only part of the simulation box around the interface is shown.

As expected, the hydrophilic head of the surfactants points toward the water phase whereas the hydrophobic tail points toward, and to some extent penetrates, the PS surface. For SDS, the water–PS interface is sharp (i.e., the two phases share a small overlapping region) for all densities. However, for the non-ionic surfactants at high 2D-densities, the variation in the water density is more gradual.

In Figure III.5 we display the free energy profiles (potentials of mean force (PMF)) of removing one surfactant adsorbed to the surface.

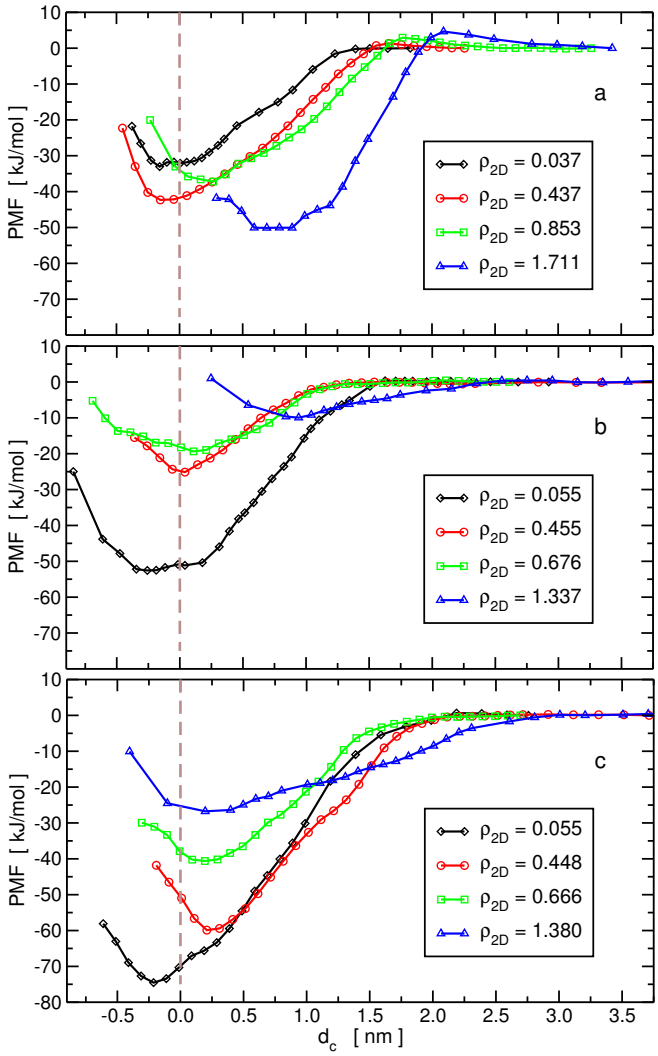

Figure III.5: The potential of mean force of pulling away one surfactant from the poly(styrene)–water interface into the water phase as a function of the constrained distance, d_c (see Experimental section for details). The different curves correspond to different 2D-densities, indicated in mg/m^2, of the surfactant adsorbed at the interface. Panel (a) is for SDS, (b) for 7PEO4PE, and (c) for Disponil AFX 1080 (10PEO6PE) surfactants. The brown vertical dashed line marks to the PS–water interface.

A clear distinction between ionic and non-ionic surfactants is observed. In the former, the strength of adsorption of SDS moderately increases with the increase of 2D-density (with a minor deviation in the trend between ρ_{2D}=0.437 mg/m^2 and ρ_{2D}=0.853 mg/m^2). In contrast, in the case of the two non-ionic surfactants, a considerably stronger force (more negative free energy) is required to pull a surfactant away from the surface as its 2D-density decreases. In addition at low concentrations of 10PEO6PE, the magnitude of the free energy is substantially larger than that of SDS, despite the fact that both have the same length of hydrocarbon tail. Both observations are in agreement with the experimental results shown in Figure III.3 which indicate the process of washing-out the surfactants is slower, and the removal of the last surfactants (i.e. at low concentrations) from the surface is more difficult for 10PEO6PE than for SDS. It should, however, be noted that the QCM experiments are affected by both the thermodynamic equilibrium of surfactant adsorption/desorption, and the kinetic processes of surfactant removal, and diffusion away from, the polymer surface. The shape of the PMF curves we obtained for these systems, as well as for other systems involving extended surfaces, [25] suggests that at least for low concentrations the free energy barrier for adsorption is either very low or practically nonexistent. Therefore, the depth of the potential-well is also a measure for the free energy barrier from which the kinetics of the desorption processes can be derived. [26, 27] As an exception for this, we point-out that at high concentrations, steric interactions and the need for surface reorganization may lead to slower adsorption kinetics than is reflected in the PMF.

The free energy change of adsorbing the surfactant from the water phase to the surface as a function of its 2D-density is shown in Figure III.6a. The qualitatively different behavior is reflected by the positive slopes for the non-ionic surfactants versus the mild negative slope for the ionic surfactant. The values of the Gibbs

energy change upon binding can be converted to equilibrium constants using the relation, $K = \exp^{-\Delta G/RT}$, which are shown for T=300 K in Figure III.6b.

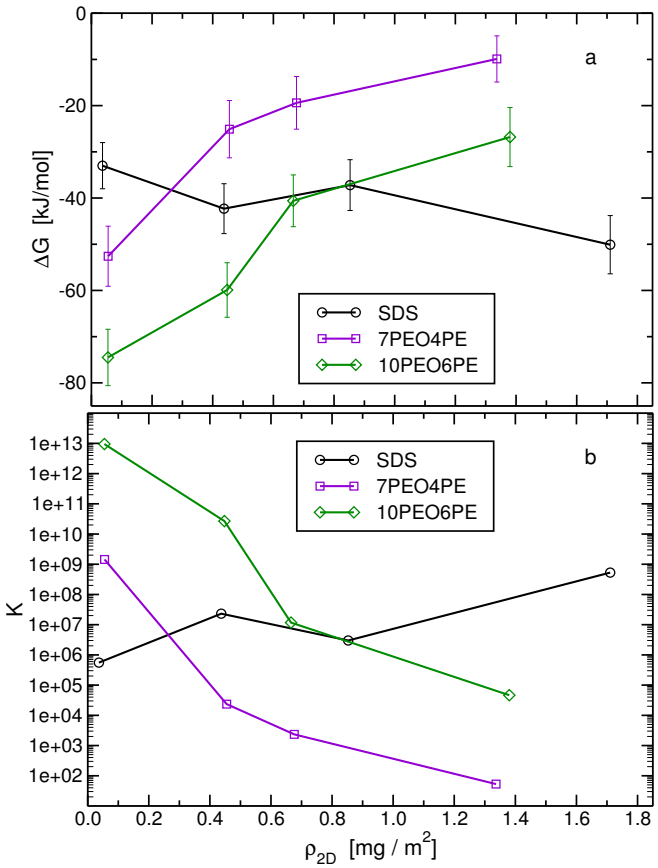

Figure III.6: (a) The Gibss (free) energy change, and (b) the corresponding equilibrium constant at T = 300K, for the adsorption process of the different surfactants at the poly(styrene)–water interface for different 2D-densities of the adsorbed surfactants.

Note however, that a direct quantitative comparison with values obtained from the experiment is not possible because the equation for the adsorption process and, thereby, the corresponding expression and dimension of the equilibrium constant are different. [28, 29] The models used experimentally consider the surface as composed of adsorbing sites with a total concentration equals to Γ_∞. In contrast, in the simulations the surface is treated as a region in space to which the surfactants can migrate without explicitly entering the equilibrium expression.

III.3.3 Properties of the Layers from by the Adsorbed Surfactants

Why do the nonionic surfactants experience substantial strengthening, whereas SDS (a moderate) weakening, in their adsorption to the PS surface with decreasing density? To address this question we first consider the direct interactions of the surfactants with the surface.

In Figure A I.5 in Appendix I, we exhibit this interaction which indicates that in all cases, the surfactant-surface attraction becomes stronger with decreasing surfactant concentration by a roughly similar slope. This can be explained by the fact that at low concentrations, the long-axis of the surfactant aligns parallel to the surface plane.

As the density increases, the surfactant long-axis tends to adopt a more perpendicular orientation (Figure A I.6 in Appendix I), thereby, losing considerable contact (and as a consequence the interaction energy) with the surface. Thus, the direct surfactant-surface interaction energy can be ruled-out as the reason for the contrasting behavior.

In the following we will argue that a significant contribution for this behavior lies in the structure of the assembly of the surfactants at the surface and the

properties of the head group.

The driving force for a surfactant in aqueous solution to adsorb at hydrophobic/hydrophilic interface is predominantly the minimization of the hydrophobic water-exposed surface area of its tail and the surface.

The interaction is thus solvent-induced and for the size of hydrophobic tail relevant to this study (large-scale regime), the adsorption process is driven by favorable changes in enthalpy and entropy. [25, 30] Nevertheless upon adsorption of surfactants, there is a loss of favorable interactions between the head group and the aqueous solution which are compensated by the reduction in the interaction between the hydrophobic surface and water. The magnitude of this loss depends on the conformation of the surfactant as well as on its environment at the interface, and therefore, can display variations with changes in the concentration of adsorbed surfactants. In Table III.2 we present the total number of hydrogen bonds in the system for the adsorbed state relative to the desorbed state.

Table III.2: The change in the number of hydrogen bonds in the entire system for the adsorption process of a single surfactant, at different surfactant concentrations, as defined in the reaction coordinate for the PMFs.

# of Surfactants	SDS	7PEO4PE	10PEO6PE
1	$+0.9 \pm 0.8$	$+2.4 \pm 0.8$	$+4.4 \pm 0.7$
8	—	$+2.1 \pm 1.0$	$+2.6 \pm 1.2$
12	$+0.2 \pm 0.7$	$+0.2 \pm 1.2$	$+0.9 \pm 1.4$
24	$+0.9 \pm 0.7$	-0.2 ± 1.3	-2.6 ± 1.1
48	$+3.9 \pm 0.7$	—	—

In the majority of the cases, the values are positive due to a reduction in the number of water molecules surrounding the surfactants or the PS surface (or equivalently, due to an increase in the number of water molecules in the bulk phase) which form a smaller number of hydrogen bonds relative to bulk waters. For the non-ionic surfactants, the excess number of hydrogen bonds in the adsorbed state decreases with increasing concentration. It starts from positive values at low concentrations and changes sign at the highest concentration.

For the ionic surfactant, no such reduction is observed. The variations are small except at the highest density where an increase is displayed. This increase is, however, likely to be a result of changes in the distributions of the counter-ions (see below).

Where does the reduction in the number of hydrogen bonds for the adsorption process of the non-ionic surfactants arise from?

Figure III.7 displays the last configuration for the simulations with the highest density for the three surfactants. The SDS molecules are assembled perpendicular, with a slight tilt, to the surface. The assembly is ordered where the tails interact with one another and the heads interact with the water molecules and the sodium ions. The interaction with sodium ions also counter-balance the electrostatic repulsions between the head groups.

In contrast, the non-ionic surfactants form a disordered assembly and the head and tail groups do not segregate due to an interwoven configuration (see also Figure III.4), a behavior in accord with experimental findings. [31]

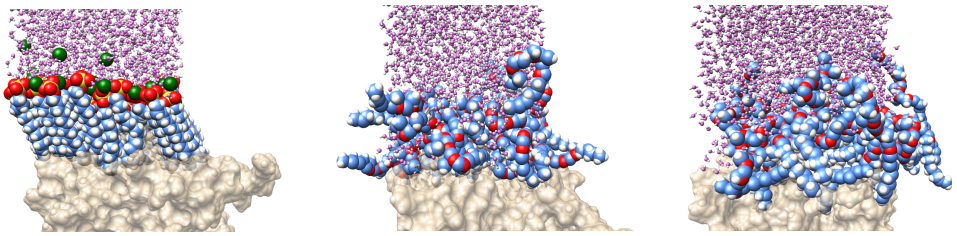

Figure III.7: Snapshots of the simulation box showing the assembly of the surfactants at the interface. Poly(styrene) molecules are represented by a surface representation in beige, water molecules (oxygens in purple and hydrogens in white) in a ball-and-stick model, sodium ions as green spheres, and the surfactant (carbon in blue, hydrogens in white, oxygens in red, and sulfur in yellow) in a space-filling model.

In Figure A I.8 in Appendix I we plot for the nonionic surfactants the head–tail radial distribution functions (excluding intra-molecule interactions).

The behavior of the curves for the first neighbor shell atoms ($r \lesssim 0.7$ nm) suggests that the degree of interweaving is slightly larger for the shorter surfactant (7PEO4PE) and that it displays a maximum as the surfactants 2D-density increases.

It is interesting to point that based on reflectometry studies on the kinetics of nonionic surfactants it was suggested that at high concentration, "the surfactant molecules stagger in the interface such that there is a possible overlap of hydrophilic headgroups with hydrophobic tails". [23] Furthermore, proton nuclear magnetic resonance relaxation investigations demonstrated that nonionic surfactants containing PEO display a high degree of flexibility. [32] Anyway in both the long and short nonionic surfactants considered in our simulations, not all of the oxygens of the PEO heads are surrounded by molecules able to donate

them a hydrogen because a significant number of these oxygens are in contact with other head groups or with the PE tails[1].

Thus, these head group oxygen atoms are not able to satisfy all their hydrogen-bond forming capacity. This partial loss of the ability to form hydrogen bonds, which is heightened by the increase of the 2D-density (and partially explains the trend observed in Table III.2 for non-ionic surfactants), will decrease the driving force of the surfactant to adsorb at the interface.

In order to quantify this effect we proceed to examine the interaction between the head groups of the surfactants and the entire system.

However, in the case of SDS we note that as the 2D-density of the surfactant increases, the concentration of the sodium ions in the vicinity of (and in contact with) these heads groups increases as well, a phenomenon reminiscent, albeit with a smaller magnitude, of multivalent counterion condensation. [33–36]

This is shown in Figure A I.9a in Appendix I by the radial distribution functions (RDFs) of the head group oxygen atoms with the oxygen of water.

A decrease in the height of the first peak is observed, which indicates reduced contacts and thereby reduced hydrogen bondings. Nevertheless, the lost hydrogen bondings with the water molecules are replaced by contacts with the sodium cations (displayed in the RDFs in Figure A I.9b in Appendix I) resulting in a gain of electrostatic interactions which also allows to overcome the repulsion between the charged head groups. Snapshots of the SDS surfactants at the interface are shown in Figure III.8.

[1]Note that only the terminal hydroxyl group of the head groups and the water molecules are able to donate a hydrogen, however, hydrogen bonds between the surfactants are found to be insignificant in number.

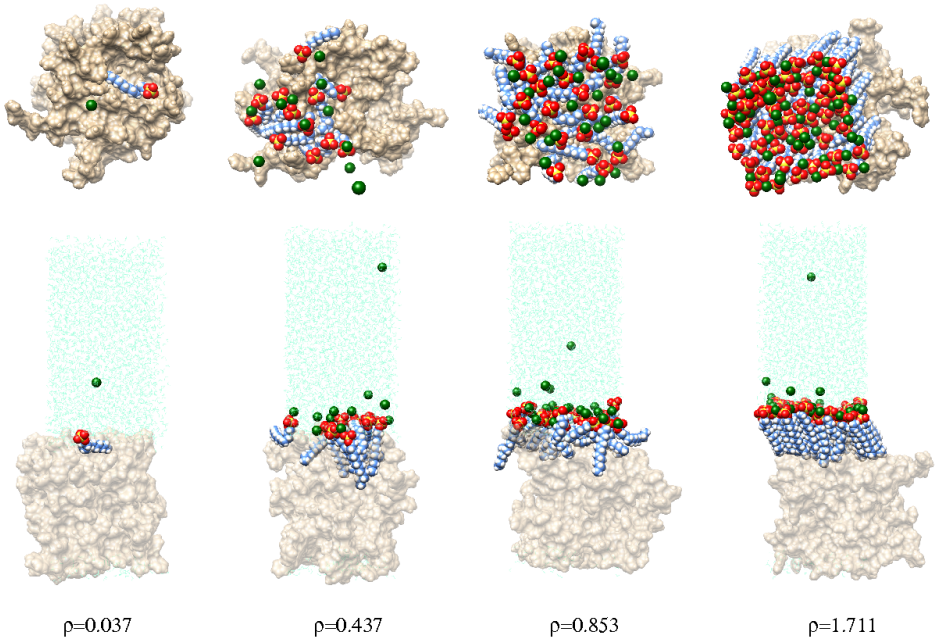

Figure III.8: Top-view (upper panel) and side-view (lower panel) of instantaneous configuration of the simulations box of the SDS surfactants adsorbed at the interface (i.e. at equilibrium) for different 2D-densities given in mg/m^2. Sodium cations are shown as green spheres, the poly(styrene) in a surface representation colored beige, and water molecules are colored in light-blue in a wire-frame representation. Note that the molecules are not broken due to periodic boundary conditions and the figures do not capture the entire length of the box along the z-axis (normal to the surface).

Thus for SDS, the interaction of the heads groups with the surrounding solvent molecules must also include the sodium cations.

In Figure III.9a we calculate the number of hydrogen bonds, and where relevant, also the number of ion contacts, between the surfactants and the entire system (for SDS a decomposition of the total number is shown in Figure A I.10 in Appendix I).

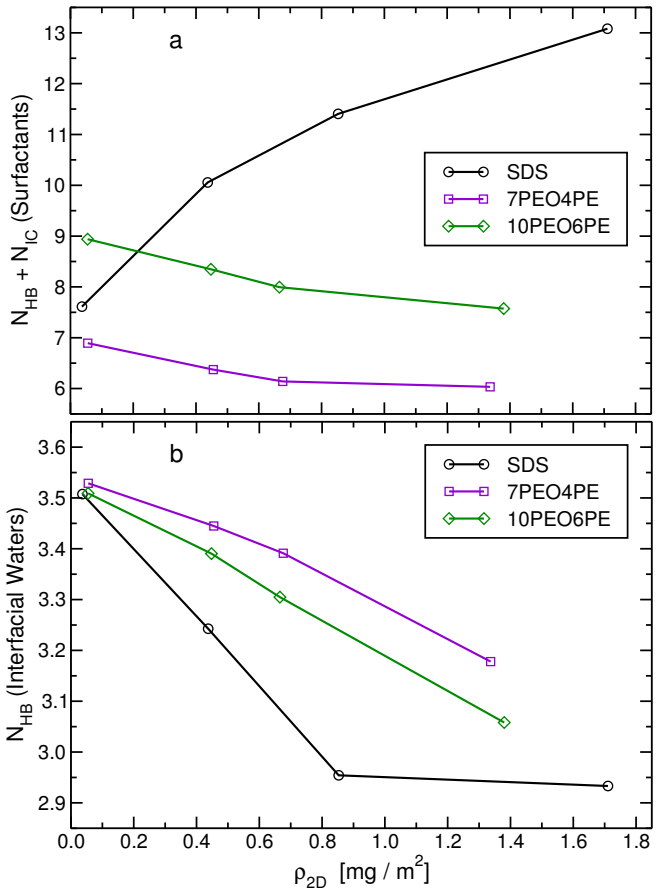

Figure III.9: (a) The number of hydrogen bonds and ion contacts, between the surfactants and the system, per surfactant. (b) The number of hydrogen bonds, per water molecule, the (intruding/interfacial) II-waters make with the system. The II-waters were determined as the first 400 waters closest to the surfactants tails. Both figures are analyzed for the adsorbed state and are plotted as a function of the 2D-density.

For the non-ionic surfactants a decrease in the number of hydrogen bonds is observed as the density is increased. This confirms the physical picture described above of the decline in the ability of the oxygen atoms of the PEO segments to accept hydrogen bonds.

The number of hydrogen bonds, per surfactant, lost for the entire density range studied is 0.9 and 1.4 for the 7PEO4PE and 10PEO6PEO, respectively.

For SDS, however, the sum of hydrogen bonds and ion-contacts exhibits an increase with increasing density, largely due to the behavior of the sodium ions. Furthermore, the impaired structure of the layer formed by the nonionic surfactants affects not only the surfactants themselves but also the surrounding water molecules.

In the density profiles shown in Figure III.4 we note that at high concentrations, the curve for water at the interface with nonionic surfactants does not decreases sharply as it does in the case of SDS.

This is due to water molecules intruding the surfactant layer and forming hydrogen bonds with the oxygen atoms of PEO as shown in Figure III.7. Obviously, this helps to stabilize the surfactant, however, at the expense of the stability of the intruding waters.

In bulk, a water molecule is surrounded by four other water molecules and at room temperature forms on average 3.5 hydrogen bonds. [37] However, when they penetrate the surfactant layer they are not able to maintain this number of hydrogen bonds.

In order to identify these penetrating waters, we calculate the minimum distance between all waters and any atom of the tail group of all surfactants. Then, we consider the first 400[2] water molecules closest to the tails. Nevertheless, for the lowest concentration these waters correspond to water molecules at the interface and to hardly any intruding waters.

In Figure III.9b we plot the number of hydrogen bonds formed by these water molecules, hereafter, referred to as (Intruding/Interfacial) II-waters.

[2]This number was estimated to be the number of water molecules penetrating the non-ionic surfactant layer in the simulations with the highest 2D-density.

For the non-ionic surfactants, a linear decrease with increasing surfactant density is observed, supporting the argument of the loss of interaction energy of the II-waters.

Figure III.10 shows a zoom of the interface layer for the long non-ionic surfactant.

It clearly demonstrates that the intruding waters and the oxygens of the PEO

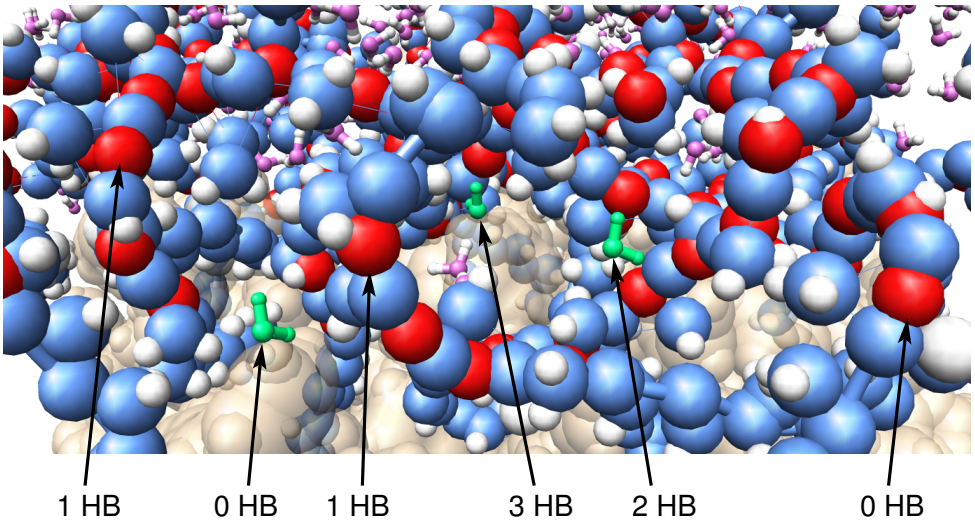

Figure III.10: A close-up of the structure of the 10PEO6PE non-ionic surfactant layer on the poly(styrene) surface at ρ_{2D}=1.380 mg/m^2. The six arrows point to three waters (colored in green) and to three surfactant oxygens and the corresponding number of hydrogen bonds these waters/oxygens make with the entire system is indicated.

segment of the surfactants form incomplete hydrogen-bond interactions.

For SDS the decrease is sharper at low densities and it seems to plateau at higher densities (nevertheless, additional densities in this region are needed to validate that it is indeed a plateau). In this case, the II-waters are predominantly interfacial and the reduction in the number of hydrogen bonds they experience

is due to an increase in the concentration of the sodium counter-ions (characterized by a relatively high-charge density) at the interface. [37]

These drastic changes of the electrostatic interactions in the system for SDS, which mainly compensate each other, are associated with large fluctuations in the energy. This unfortunately, impede us from drawing further conclusions on the adsorption of the ionic surfactant to the surface.

Concerning the effect of entropy and especially that originating from the flexibility of the surfactant chains, we note that in addition to the orientational preference of the long axis of the surfactants, Figure A I.6 in Appendix I indicates that the end-to-end distance of the PEO-PE surfactants increases with concentration whereas that of SDS hardly changes (as expected from their different persistence lengths. [38, 39]) Such straightening of the PEO-PE chains reduces their entropy and thereby contributes to their weakened adsorption with increasing concentration.

Nevertheless, it is not the only factor affecting the Gibbs adsorption energy because the curves in Figure A I.6 in Appendix I do not mirror the changes in the adsorption free energy shown in Figure III.6. Furthermore, from additional simulations we conducted of the same nonionic surfactants but with artificially stiff dihedral angles (see description in the Supplementary Information of Appendix I, Figure A I.11 and Figure A I.12) we obtained that the reduction of the chains flexibility was accompanied also by a loss in the degree of interweaving heads and tails groups (Figure A I.13 in Appendix I), as well as, by a loss in the ability of the surfactants to hydrogen bond with the water molecules (Table A I.5 in Appendix I).

III.4 Conclusions

Surfactants in aqueous solutions favorably adsorb to hydrophobic surfaces in order to minimize the hydrophobic solvent exposed area of their tails and the surface. Normally, it is assumed that upon adsorption the interactions of the head groups with the solvent are not substantially affected. However, in this work we find that this is not the case, especially for nonionic surfactants with aprotic head groups such as poly(ethylene oxide). This conclusion, together with the explanation we provide for the contrasting behavior of ionic and nonionic surfactants, critically relies on two observations obtained from the simulations. The first is that there is a large degree of interweavement between head and tail groups in the adsorbed layer formed by the non-ionic surfactant (PEO/PE systems). The second is that water molecules penetrate this layer. In the disordered layer these nonionic surfactants generate at the surface, only oxygens of the head groups present at the interface with the water phase or oxygens next to penetrating waters can form hydrogen bonds. Oxygens inside this layer lose this favorable energy, with a magnitude that increases with the surfactants density at the interface. This reduced stability of the surfactants diminishes their driving force for adsorption. That means, the effective interaction of the surfactant with the surface increases with the decrease in their concentration. This behavior is shown to be in accordance with experimental results on the dynamics of surfactant desorption, which indicated that at low surface concentrations non-ionic surfactants are very slow to desorb from the surface. In the case of the ionic surfactant this behaviour is not observed. In this case, SDS assembles into an ordered structure and the attraction to the surface was even slightly augmented at higher surfactant concentrations, in agreement with the experimentally determined adsorption isotherm. We hypothesize, that the

reason these two types of surfactants behave differently is because the ionic surfactant has a small head group that is strongly hydrophilic, whereas, the head groups of the nonionic surfactants are large and only weakly attracted to water.

References

[1] Sauerbrey, G. Verwendung von Schwingquarzen zur Wägung dünner Schichten und zur Mikrowägung, *Zeitschrift für Physik* 1959, *155*(2), 206–222.

[2] Hess, B.; Kutzner, C.; Van Der Spoel, D.; Lindahl, E. Gromacs 4: algorithms for highly efficient, load-balanced, and scalable molecular simulation, *J. Chem. Theory Comput.* 2008, *4*, 435–447.

[3] Bussi, G.; Donadio, D.; Parrinello, M. Canonical Sampling through Velocity Rescaling, *J. Chem. Phys.* 2007, *126*, 014101.

[4] Berendsen, H. J.; Postma, J. v.; van Gunsteren, W. F.; DiNola, A.; Haak, J. Molecular dynamics with coupling to an external bath, *J. Comput. Phys.* 1984, *81*(8), 3684–3690.

[5] Darden, T.; York, D.; Pedersen, L. Particle Mesh Ewald: An N-log(N) Method for Ewald Sums in Large Systems, *J. Chem. Phys.* 1993, *98*, 10089–10092.

[6] Essmann, U.; Perera, L.; Berkowitz, M. L.; Darden, T.; Lee, H.; Pedersen, L. G. A Smooth Particle Mesh Ewald Method, *J. Chem. Phys.* 1995, *103*, 8577–8593.

[7] Horn, H. W.; Swope, W. C.; Pitera, J. W.; Madura, J. D.; Dick, T. J.; Hura, G. L.; Head-Gordon, T. Development of an improved four-site water model for biomolecular simulations: TIP4P-Ew, *J. Chem. Phys.* 2004, *120*, 9665–9678.

[8] Tang, X.; Koenig, P. H.; Larson, R. G. Molecular Dynamics Simulations of Sodium Dodecyl Sulfate Micelles in Water - The Effect of the Force Field, *J. Phys. Chem. B* 2014, *118*, 3864–3880.

[9] Berendsen, H. J. C.; Grigera, J. R.; Straatsma, T. P. The missing term in effective pair potentials, *J. Phys. Chem.* 1987, *91*, 6269–6271.

[10] Miyamoto, S.; Kollman, P. A. SETTLE: An Analytical Version of the SHAKE and RATTLE Algorithms for Rigid Water Models, *J. Comp. Chem.* 1992, *13*, 952–962.

[11] Luzar, A.; Chandler, D. Structure and hydrogen bond dynamics of water-dimethyl sulfoxide mixtures by computer simulations, *J. Chem. Phys.* 1993, *98*, 8160–8173.

[12] Mukerjee, P.; Mysels, K. J. *Critical Micelle Concentrations of Aqueous Surfactant Systems;* U.S. National Bureau of Standards: Washington, DC, 1971.

[13] Volkova-Gugeshashvili, M. I.; Volkov, A. G.; Markin, V. S. Adsorption at Liquid Interfaces: The Generalized Frumkin Isotherm and Interfacial Structure, *Russ. J. Electrochem.* 2006, *42*, 1073–1078.

[14] Vale, H. M.; McKenna, T. F. Adsorption of sodium dodecyl sulfate and sodium dodecyl benzenesulfonate on poly(vinyl chloride) latexes, *Colloids and Surfaces A: Physicochem. Eng. Aspects* 2005, *268*, 68–72.

[15] Hecht, L. L.; Schoth, A.; Muñoz-Espí, R.; Javadi, A.; Köhler, K.; Miller, R.; Landfester, K.; Schuchmann, H. P. Determination of the Ideal Surfactant Concentration in Miniemulsion Polymerization, *Macromol. Chem. Phys.* 2013, *214*, 812–823.

[16] Brown, W.; Zhao, J. Adsorption of Sodium Dodecyl Sulfate on Polystyrene Latex Particles using Dynamic Light Scattering and Zeta Potential Measurements, *Macromolecules* 1993, *26*, 2711–2715.

[17] Colombié, D.; Landfester, K.; Sudol, E. D.; .; El-Aasser, M. S. Competitive Adsorption of the Anionic Surfactant SLS and the Nonionic Surfactant Triton X-405 on Polystyrene Latex Particles, *Langmuir* 2000, *16*, 7905–7913.

[18] Ballard, N.; Urrutia, J.; Eizagirre, S.; Schäfer, T.; Diaconu, G.; de la Cal, J. C.; Asua, J. M. Surfactant Kinetics and Their Importance in Nucleation Events in (Mini)emulsion Polymerization Revealed by Quartz Crystal Microbalance with Dissipation Monitoring, *Langmuir* 2014, *30*, 9053–9062.

[19] Turner, S. F.; Clarke, S. M.; Rennie, A. R.; Thirtle, P. N.; Cooke, D. J.; Li, Z. X.; Thomas, R. K. Adsorption of Sodium Dodecyl Sulfate to a Polystyrene/Water Interface Studied by Neutron Reflection and Attenuated Total Reflection Infrared Spectroscopy, *Langmuir* 1999, *15*, 1017–1023.

[20] Brown, J. W.; Huestis, W. H. Structure and orientation of a bilayer-bound model tripeptide. A ^{1}H NMR study, *J. Phys. Chem.* 1993, *97*, 2967–2973.

[21] Zhao, J.; Brown, W. Dynamic Light Scattering Study of Nonionic Surfactant ($C_{12}E_{25}$) Adsorption on Polystyrene Latex Particles: Effect of Poly(ethylene oxide) Chain Size, *J. Phys. Chem.* 1996, *100*, 5908–5912.

[22] Postmus, B. R.; Leermakers, F. A. M.; Koopal, L. K.; Cohen Stuart, M. A. Competitive Adsorption of Nonionic Surfactant and Nonionic Polymer on Silica, *Langmuir* 2007, *23*, 5532–5540.

[23] Geffroy, C.; Cohen Stuart, M. A.; Wong, K.; Cabane, B.; Bergeron, V. Adsorption of Nonionic Surfactants onto Polystyrene: Kinetics and Reversibility, *Langmuir* 2000, *16*, 6422–6430.

[24] Lu, J. R.; Li, Z. X.; Thomas, R. K.; Staples, E. J.; Thompson, L.; Tucker, I.; Penfold, J. Neutron Reflection from a Layer of Monododecyl Octaethylene Glycol Adsorbed at the Air-Liquid Interface: The Structure of the Layer and the Effects of Temperature, *J. Phys. Chem.* 1994, *98*, 6559–6567.

[25] Zangi, R. Driving Force for Hydrophobic Interaction at Different Length-Scales, *J. Phys. Chem. B* 2011, *115*, 2303–2311.

[26] Kramers, H. A. Brownian Motion in a Field of Force and the Diffusion Model of Chemical Reactions, *Physica* 1940, *7*, 284–304.

[27] Hagen, S. J. Solvent Viscosity and Friction in Protein Folding Dynamics, *Curr. Protein Pept. Sci.* 2010, *11*, 385–395.

[28] Liu, Y. Is the Free Energy Change of Adsorption Correctly Calculated?, *J. Chem. Eng. Data* 2009, *54*, 1981–1985.

[29] Zhou, X.; Zhou, X. The Unit Problem in the Thermodynamic Calculation of Adsorption Using the Langmuir Equation, *J. Chem. Eng. Data* 2014, *201*, 1459–1467.

[30] Lum, K.; Chandler, D.; Weeks, J. D. Hydrophobicity at small and large length scales, *J. Phys. Chem. B* 1999, *103*, 4570–4577.

[31] Lu, J. R.; Su, T. J.; Li, Z. X.; Thomas, R. K.; Staples, E. J.; Tucker, I.; Penfold, J. Structure of Monolayers of Monododecyl Dodecaethylene Glycol at the Air-Water Interface Studied by Neutron Reflection, *J. Phys. Chem. B* 1997, *101*, 10332–10339.

[32] Boissier, C.; Löfroth, J.-E.; Nydén, M. Water-Based Latex Dispersions. 2. Adsorption and Dynamics of Nonionic Surfactants on Colloidal Particles with Different Interfacial Properties, *Langmuir* 2002, *18*, 7313–7319.

[33] Manning, G. S. Limiting Laws and Counterion Condensation in Polyelectrolyte Solutions I. Colligative Properties, *J. Chem. Phys.* 1969, *51*, 924–933.

[34] Mukherjee, A.; Schmitz, K.; Bhuiyan, L. Overcharging in macroions. effects of macroion geometry/charge distribution, *Langmuir* 2003, *19*, 9600–9612.

[35] Besteman, K.; Zevenbergen, M. A. G.; Lemay, S. G. Charge inversion by multivalent ions: Dependence on dielectric constant and surface-charge density, *Phys. Rev. E* 2005, *72*, 061501.

[36] Li, W.; Zheng, X.; Dong, Z.; Li, C.; Wang, W.; Yan, Y.; Zhang, J. Molecular Dynamics Simulations of CO_2/N_2 Separation through Two-Dimensional Graphene Oxide Membranes, *J. Phys. Chem. C* 2016, *120*, 26061–26066.

[37] Zangi, R. Can Salting-In/Salting-Out Ions be Classified as Chaotropes/Kosmotropes?, *J. Phys. Chem. B* 2010, *114*, 643–650.

[38] Magid, L. J.; Li, Z.; Butler, P. D. Flexibility of Elongated Sodium Dodecyl Sulfate Micelles in Aqueous Sodium Chloride: A Small-Angle Neutron Scattering Study, *Langmuir* 2000, *16*, 10028–10036.

[39] Lee, H.; Venable, R. M.; MacKerell, A. D.; Pastor, R. W. Molecular Dynamics Studies of Polyethylene Oxide and Polyethylene Glycol: Hydrodynamic Radius and Shape Anisotropy, *Biophys. J.* 2008, *95*, 1590–1599.

Chapter IV

Shedding Light on the Different Behavior of Ionic and Nonionic Surfactants in Emulsion Polymerization: From Atomistic Simulations to Experimental Observations

Absorption of Surfactants Into a Hydrophobic Phase

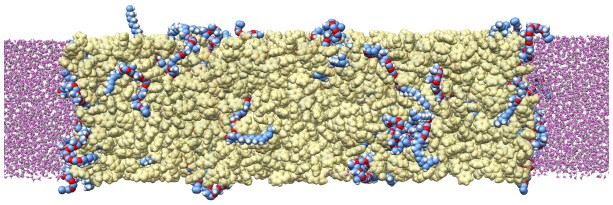

Contents

The results in this Chapter were published in:
Giulia Magi Meconi, Nicholas Ballard, José M. Asua and Ronen Zangi,
Shedding Light on the Different Behavior of Ionic and Nonionic Surfactants in Emulsion Polymerization: From Atomistic Simulations to Experimental Observations,
Phys. Chem. Chem. Phys. **2017**,19, 31692-31705.
doi: 10.1039/C7CP05206E.

IV.1 Introduction

Inspired by previous experimental and computational studies in Chapter III of emulsion polymerization in the presence of ionic and nonionic surfactants, in this chapter we investigate the different behavior of the two types of surfactant during the polymerization process as the organic phase shifts from being a liquid monomer-rich to a solid polymer.

MD simulations were helpful to have a deeper comprehension of the behavior of surface active agents at molecular level. Moreover, the vast majority of the computational studies of surfactants are limited to the behavior at interfaces [1–4] and/or inside aqueous solutions [5–8], whereas the behavior inside an organic phase has been overlooked.

First, an experimental study of two surfactants, SDS and Disponil AFX 1080, is performed with a focus on the differing behavior they induce with respect to particle nucleation and the effect on the polymerization process.

Second, using atomistic MD simulations these results are subsequently explained and characterized by examining the differences in surfactant behavior at the interface between water and an organic phase with varying binary composition of styrene and poly(styrene).

IV.2 Experimental

IV.2.1 Experimental Details

Materials

Technical grade styrene (styrene, Quimidroga) was used as received. Sodium dodecyl sulfate (>99.5%, Aldrich) was recrystalized from an ethanol/water mixture, ammonium persulfate (APS, 99%, Aldrich), 2,2'-Azodi(2-methylbutyronitrile) (¿98%, Aldrich), dodecanethiol (>98%, Aldrich) and Disponil AFX 1080 (80% active content, BASF) were used as received. Doubly deionized water was used throughout the work. All other solvents were purchased from Scharlab and were of technical grade.

Latex characterization

Z-average particle diameters were determined by dynamic light scattering performed on a Malvern Zetasizer ZS using a scattering angle of 173° at a standard temperature of 25 °C. Each measurement was conducted in triplicate and the average of the three values was taken. Drop shape analysis for surface tension measurements were conducted using a DataPhysics OCA contact angle system. The reported values are taken using an average of 5 measurements with different drops.

Scanning Electron Microscopy (SEM) images were obtained using a Quanta 250 FEG ESEM (FEI, Netherlands). An aluminium stub covered with mica was used as a substrate. To obtain monolayer coverage of polymer particles on the substrate, the latex was diluted to 0.1 wt% solids content. A drop of the diluted

latex was placed onto the substrate which was dried. The images were recorded under high vacuum at an accelerating voltage of 10 kV.

Synthesis of low molecular weight poly(styrene)

Low molecular weight poly(styrene) (PS), to enable the handling of styrene/PS mixtures with high PS content, was synthesized by solution polymerization in the presence of high amount of chain transfer agent. Styrene (50 g), toluene (50 g), dodecanethiol (2.5 g) and 2,2'-Azodi(2-methylbutyronitrile) (0.25 g) were added to a 250 mL round bottomed flask equipped with reflux condenser and nitrogen inlet and heated to 70 °C. The reaction was left for 24 h and after cooling the polymer was precipitated in MeOH. The solid was redissolved in chloroform, reprecipitated in MeOH, filtered and dried under vacuum.

Surfactant partitioning behavior

Styrene/polystyrene solutions ranging in composition from 0% polystyrene to 60% polystyrene by mass were formed by dissolving the low molecular weight polystyrene, synthesized as described above, over the course of 24 h. The partitioning behavior of the surfactants was analyzed by mixing 4 g of 20 mM aqueous surfactant solutions of SDS and Disponil AFX 1080 with 1 g of the styrene/polystyrene solution. The vials were placed in a water bath at 60 °C equipped with a shaking unit for 24 h to allow the surfactant to equilibrate with the two phases. After this time, the aqueous phase was removed and the solid content was analyzed gravimetrically. The residual solid from the aqueous phase was also subjected to ^{1}H NMR on a Bruker Avance DPX 400 MHz spectrometer in $(CD_3)_2CO$ at 25 °C. A relaxation time of 10 s was used in NMR measurements

to ensure a quantitative measurement. In order to determine the distribution of ethylene oxide groups in the two phases, the average number of ethylene oxide groups in the surfactant partitioned in the aqueous phase, N_{EO}, was calculated by comparison of the integrals of the terminal methyl group of the polyethylene glycol chain at 0.9 ppm with the ethylene glycol groups at 3.6 ppm using the formula,

$$N_{EO} = \frac{I_{3.6}/4}{I_{0.9}/3} \quad . \tag{IV.1}$$

Batch Emulsion Polymerization

Batch emulsion polymerizations were carried out in a Mettler Toledo RC1 calorimeter equipped with an anchor type stirrer rotating at 150 rpm. Water (390 g), styrene (100 g) and surfactant were added to the reactor and degassed by nitrogen bubbling for 30 minutes, stirring constantly, and then heated to 75 °C. Once at reaction temperature, ammonium persulfate (1 g dissolved in 10 g water) was added in a single shot. The reaction was continued until the change in conversion was negligible as observed from the heat flow. Conversion of monomer as a function of time was determined from the evolution of heat flow during the reaction. At selected time intervals samples of the reaction were taken for particle size and surface tension measurements. The formulations for the batch reactions carried out are given in Table IV.1.

Table IV.1: Recipes for batch emulsion polymerization of styrene using ionic (SDS) and nonionic (Disponil AFX 1080) surfactants.

	water [g]	styrene [g]	APS [g]	SDS [g]	Disponil AFX 1080 [g]
Run 1	400	100	1	0.58 (5 mM)	—
Run 2	400	100	1	1.15 (10 mM)	—
Run 3	400	100	1	2.30 (20 mM)	—
Run 4	400	100	1	—	3.20 (10 mM)
Run 5	400	100	1	—	6.40 (20 mM)
Run 6	400	100	1	—	12.80 (40 mM)

Semi-batch Emulsion Polymerization

Semi-batch emulsion polymerizations were carried out in a 500 mL glass reactor equipped with an anchor type stirrer rotating at 150 rpm. Water (390 g) and surfactant were added to the reactor and degassed by nitrogen bubbling for 30 minutes, stirring constantly, and then heated to 75 °C. Once at reaction temperature, ammonium persulfate (1 g dissolved in 10 g water) was added in a single shot and styrene (100 g) was fed over the course of 3 hr. At the end of the feeding period the reaction was held at 75 °C for an additional 2 hr in order to achieve full monomer conversion. At selected time intervals samples of the reaction were taken for conversion, particle size and surface tension measurements. Conversion of monomer as a function of time was determined gravimetrically. The formulations for the semi-batch reactions carried out are given in Table IV.2.

Table IV.2: Recipes for semi-batch emulsion polymerization of styrene using ionic (SDS) and nonionic (Disponil AFX 1080) surfactants.

	water [g]	styrene [g]	APS [g]	SDS [g]	Disponil AFX 1080 [g]
Run 7	400	100	1	2.30 (20 mM)	—
Run 8	400	100	1	—	6.40 (20 mM)

IV.2.2 Computational Details

We conducted simulations of the adsorption of non-ionic surfactants at the interface between water and an organic phase. Five different organic phases with different compositions of PS and styrene (S) were considered: 100% PS, 75% PS / 25% S, 50% PS / 50% S, 25% PS / 75% S, and 100% S. For each type of organic phase we performed several simulations corresponding to different concentrations of the surfactant. The nonionic surfactant used, 10PEO6PE, is a block copolymers of 10 units of poly(ethylene oxide) (PEO) and 6 units of poly(ethylene) (PE). In addition, to compare the behavior observed with that for ionic surfactants, simulations with SDS molecules were performed as well. In Tables A II.6–A II.7 of the Appedix II we report the details of these simulations, and in Tables A II.9–A II.12 and Figures A II.14–A II.17 we provide the force-field parameters describing the (explicit-hydrogen all-atom) models for the surfactants and organic phase.

In order to prepare the starting conformations, the organic phase was pre-equilibrated as a bulk for 40 ns before the addition of surfactants and water. Then, this organic phase was placed in the middle of a rectangular box, larger along the z-axis, and surfactants (in extended conformations in which their long-axis normal and their tail point to the organic phase) were equally distributed

on each side of its two interfaces. The region in the simulation box which does not include styrene or PS was then filled with water molecules described by the TIP4P-Ew model. [9] Note that certain properties deducted from simulations of charged surfactants can be sensitive to the choice of the water model. This is noticeable only at high concentrations of ionic surfactants at the interface. For example, SPC/E and TIP4P-Ew water models yield very similar adsorption affinity of SDS to a polymeric surface, however, at high concentrations there are quantitative differences.[1] [10, 11] Periodic boundary conditions in all three dimensions were employed for the simulations, nevertheless, the box lengths in the x- and y-directions were large enough to ensure absence of short-range interactions of any surfactant with its periodic image. These systems were subject to an equilibration time of 100 ns. However for the 100% S systems, this time was extended to 120 ns (for 0–20 surfactants) and 150 ns (for 30–120 surfactant) due to the miscibility of the surfactants, above a critical concentration, in the organic phase. Then, the simulations were continued for additional 20 ns for data collection. The amount of surfactants at the interface is reported by the two dimensional density, $\rho_{2D} = m/2A$, where m is the mass of the surfactants and A is the area of the simulation box in the xy-plane. The location of the interface was determined by a drop of the water density to half of its value in the bulk, i.e., to $\sim$ 500 kg/m^3.

The calculations and the preparations of the systems for the Potential of Mean Force (PMF) of pulling one adsorbed surfactant from the interface to the water phase were done according to the protocol described in the III. [11] In brief, the reaction coordinate was described by the (shortest) distance, d_c, between the

[1] We conjecture that different water models affect differently the extent of counterion condensation onto the assembled structure of the surfactants leading to different magnitudes of repulsive energy between the ionic head groups.

interface and a carbon atom of the hydrophobic tail of the surfactant covalently bonded to the oxygen atom of the hydrophilic head (see Figure A II.17 and Figure A II.16 in Appendix II). In practice, the distance involving this carbon atom of the surfactant was constrained relative to the center of mass of a cylindrical cut of the organic phase, and only during analysis a shift to represent the distance relative to the interface was applied. For several distances along the reaction coordinate, the system was equilibrated for a time period in the range of 14 ns to 50 ns (depending on the time the system displayed convergence of the constrained force). The average force that was required to constrain the distance between the reference and the pull group was calculated in a data collection step of additional 36 ns. To obtain the PMF (or free/Gibbs energy profile), this average force was integrated as a function of the constrained distance, d_c. Because the PMF represents only relative values, it was shifted such that the Gibbs energy of the state at the largest separation corresponds to zero. Note that in these series of simulations, only one interface between the organic phase and water was initially adsorbed with surfactants. Further details on this series of simulations are given in Table A II.8 in Appendix II.

All computer simulations were performed using the molecular dynamics package GROMACS version 4.6.5. [12] A constant temperature of 300 K was maintained by the velocity rescaling thermostat [13] with a coupling time of 0.1 ps. The box length along the z-axis was fixed during the simulation, however, in the xy-plane the pressure was maintained at 1.0 bar utilizing the Berendsen barostat [14] with a compressibility of $1 \cdot 10^{-6}$ bar^{-1} and a coupling time of 1.0 ps. Electrostatic interactions were calculated using the Particle-Mesh-Ewald method. [15, 16] Quadratic interpolation was used with a real space cutoff of 0.9 nm and a grid spacing for the reciprocal-space of 0.12 nm. A 0.9 nm cut-off was also used to calculate the Lennard-Jones potential applying long range

dispersion corrections for the energy and pressure. Water bond distances and angles were constrained using the SETTLE algorithm [17], whereas all-other bond distances were constrained using the LINCS algorithm. [18] A time step of 2 fs was used to integrate the equation of motion, except for simulations utilizing the pull-code (for calculating the PMFs). Constraining the distance d_c within the pull-code resulted in occasional instabilities, which disappeared upon reduction of the time step to 1 fs. Therefore, in these simulations a 1 fs time step was used. Two molecules were considered to be hydrogen bonded if the distance between the donor (oxygen) and acceptor (oxygen) is smaller than 0.35 nm and the hydrogen–oxygen(donor)–oxygen(acceptor) interaction angle is smaller than 30°. [19] Figures A II.19a and A II.19b in Appendix II indicate these values to be appropriate for our systems as well.

IV.3 Results and Discussion

In order to gain an insight into the different behavior ionic and nonionic surfactants have during emulsion polymerization, we performed emulsion polymerization of styrene using varying quantities of an ionic surfactant, SDS (5–20 mM), and a nonionic surfactant, Disponil AFX 1080 (10-40 mM), at a solids content of 20%. The reactions were carried out in a calorimeter reactor to allow for continuous monitoring of the rate of polymerization and samples were taken periodically for measurements of the particle size and surface tension of the aqueous phase. The evolution of the heat of reaction, particle size, and surface tension as a function of conversion, for various concentrations of SDS, are shown in Figure IV.1.

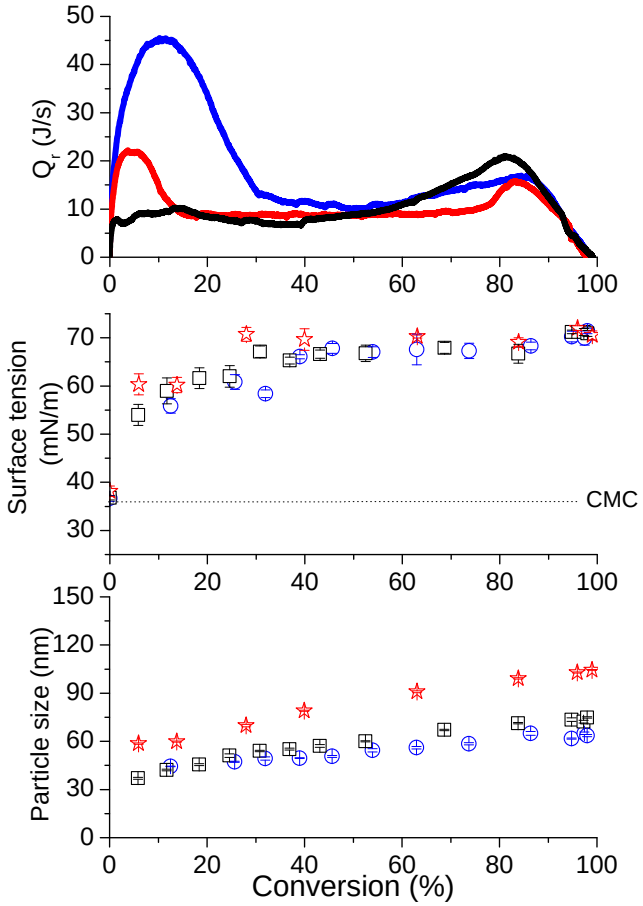

Figure IV.1: Evolution of heat of reaction, surface tension and particle size as a function of conversion for emulsion polymerization of styrene with 5 mM (Run 1, red line and stars), 10 mM (Run 2, black line and squares), and 20 mM (Run 3, blue line and circles) SDS.

Figure IV.1 indicates that SDS behaves as a 'classical' surfactant in the emulsion polymerization of styrene. Based on the surface tension measurements, it is evident that initially the surfactant concentration in the aqueous phase is slightly below the CMC for Run 1 and above the CMC for Runs 2 and 3, as expected based on the known CMC of SDS (8.2 mM) [20] and the concentrations of SDS used. In the early stages of the reaction, the surface tension rapidly increases in all cases as a result of micellar particle nucleation and adsorption of the surfactant to the newly formed interfaces. The surface tension reaches a steady value close to that of pure water indicating a low concentration of free surfactant in the aqueous phase. It can be observed that the particle size increases with decreasing surfactant concentration. At higher surfactant concentration the initial number of micelles in the system is higher and thus a higher number of particles are generated in the early stages of the reaction, which are consequently of lower size. The evolution of the rate of polymerization, as reflected by the heat of reaction, shows an initial rapid rate which slows to a constant value, perhaps as a result of some coalescence of particles which reduces the overall number of particles and thus the polymerization rate. As may be expected due to effects of radical compartmentalization, which results in a reduced termination rate for smaller particle sizes, this initial rise in the heat of polymerization is largest for the reaction containing most surfactant, where particle size is smallest. At around 80% conversion, there is a rapid increase heat of reaction which corresponds to the time at which the gel effect becomes visible. [21] In this region the rate of termination is lowered due to restricted diffusion of the propagating chains which results in an increase in the rate of polymerization. The behavior of the nonionic surfactant Disponil AFX 1080 in the emulsion polymerization strongly differs from that of SDS as can be observed in Figure IV.2.

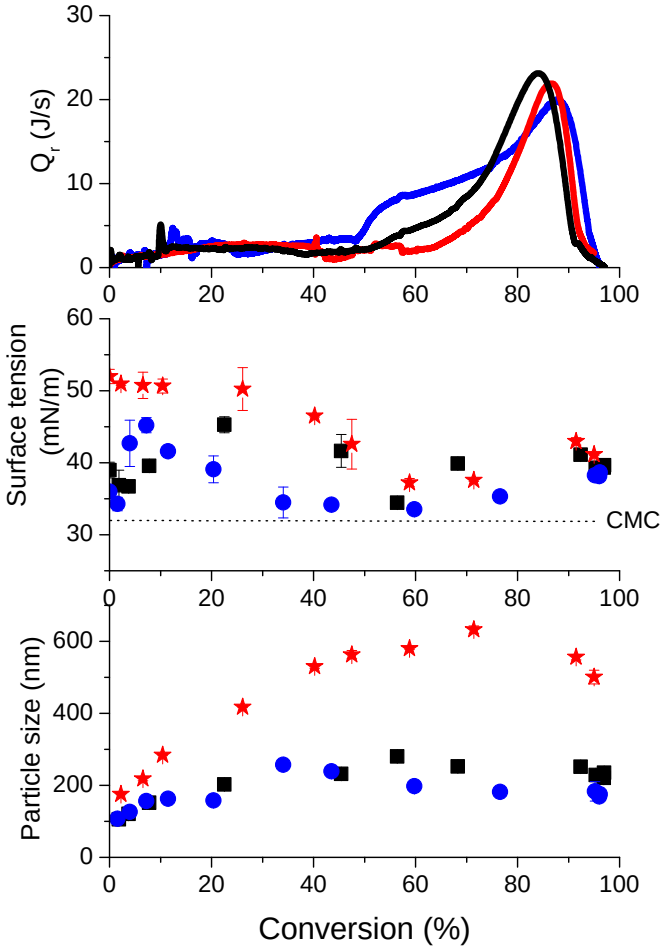

Figure IV.2: Evolution of heat of reaction, surface tension and particle size as a function of conversion for emulsion polymerization of styrene with 10 mM (Run 4, red line and stars), 20 mM (Run 5, black line and squares), and 40 mM (Run 6, blue line and circles) Disponil AFX 1080.

Despite using a concentration of Disponil AFX 1080 which is at least an order of magnitude higher than the CMC, [22] the surface tension measurements reveal that from the first moment the concentration of surfactant in the aqueous phase is below the CMC. The low concentration of surfactant in the aqueous phase leads to nucleation of fewer particles, primarily by homogeneous nucleation, which are consequently of a larger size. The nucleation period is accompanied by a decrease in the surfactant concentration in the aqueous phase for reactions with 10 and 20 mM Disponil AFX1080, because the limited amount of surfactant in the aqueous phase adsorbs to the newly formed interfaces. The relatively large size of the particles also means that in the early stages of the reaction the rate of polymerization is low as reflected by initial values for the heat of polymerization which are an order of magnitude below that of the reactions conducted using SDS as surfactant. As the reaction progresses, the concentration of surfactant in the aqueous phase increases and eventually reaches the CMC. At this point, the onset of nucleation of a second crop of much smaller particles by heterogeneous (micellar) nucleation leads to a decrease in the average particle size. Due to the increased number of particles in the system and the well known effects of radical compartmentalization in emulsion polymerization, the nucleation of new particles also results in a concomitant increase in the rate of polymerization, as is observed in the rapid increase in the heat of polymerization. With lowering the amount of surfactant in the formulation, this effect was observed at a later stage in the polymerization process. It should also be noted that contrary to the work of Özdeğer et al. [23] (mentioned in the Section I.2.5 of the Chapter I) this effect could be seen to occur after the disappearance of monomer droplets ($\sim$40% for styrene) in some reactions. At high conversion, as for SDS, the gel effect is observed which is visible in the onset of a high rate of polymerization at around 80% conversion. The appearance of a new crop

of particles, arising from secondary nucleation in the emulsion polymerization of styrene, when using a nonionic surfactant is confirmed visually by scanning electron microscopy images of the final latex displayed in Figure IV.3.

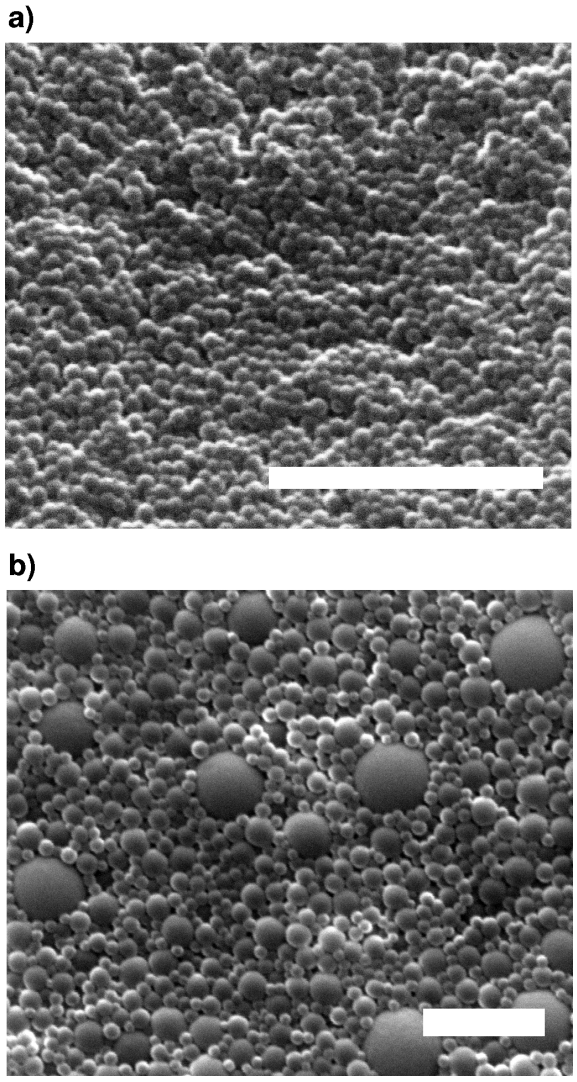

Figure IV.3: SEM images of latexes synthesis using either (a) SDS (Run 3) or (b) Disponil AFX 1080 (Run 5). In both cases the white scale bar represents 1 micron.

It can be seen that latexes synthesized with SDS contain a unimodal distribution of small particles, whereas those synthesized with Disponil AFX 1080 contain one crop of large particles and a second crop of much smaller particles. The larger particles are formed at the beginning of the reaction where the aqueous phase surfactant concentration is low. The large size of these particles is in agreement with the initial low rate of polymerization as discussed above. The smaller particles are formed at the point at which the CMC is reached in the aqueous phase, which leads micellar nucleation and results in a new crop of small particles as well as the reduction in the average particle size as shown by DLS measurements (see Figure IV.2).

How is it possible that the amount of (nonionic) surfactant in the aqueous phase increases during the polymerization reaction? Note that the area of the interface at which the surfactant adsorb only increases during the reaction. Similar to the conclusions reported by Özdeğer et al. [23], we hypothesize that initially the surfactant is somehow partitioned into the organic phase and later, as the reaction proceeds, is released into the aqueous phase. It is therefore the purpose of this Chapter to confirm this hypothesis, to investigate how a surfactant with a hydrophilic head can partition into a completely hydrophobic medium, and why it is then released at later stages of the polymerization process.

We start by designing a simple direct experiment in which we measure the partition coefficient of both SDS and Disponil AFX 1080 between water and an organic phase containing various compositions of styrene and PS. The partition coefficient, P_s, was calculated by,

$$P_s = \frac{m_{s,op}/m_{op}}{m_{s,aq}/m_{aq}} \quad , \tag{IV.2}$$

where $m_{s,op}$ is the mass of surfactant in the organic phase and m_{op} is the mass of the organic phase. The corresponding terms for the aqueous phase are

$m_{s,aq}$ and m_{aq}. Note that in this experiment it is not possible to distinguish between surfactants adsorbed at the interface to those absorbed inside the organic phase. Nevertheless, the area of the interface relative to the volume of the organic phase is very small so the amount of surfactant at the interface can be ignored. The results shown in Figure IV.4 indicate that SDS resides entirely (within experimental error) in the aqueous phase. In this case, the surfactant may be expected to behave as a classical surfactant in emulsion polymerization as initially postulated by Smith and Ewart. [24] In contrast, for Disponil AFX 1080 the surfactant is present substantially in the organic phase. As the quantity of monomeric styrene in the organic phase increases the surfactant has an increasing affinity for the organic phase. Furthermore for organic phases containing less than 45% PS, the concentration of surfactant in the organic phase is larger than in water. This means that in emulsion polymerization the surfactant is partitioned not just between the aqueous phase and the polymer–water interface, but also partitions into the monomer droplets and/or the polymer particles themselves.

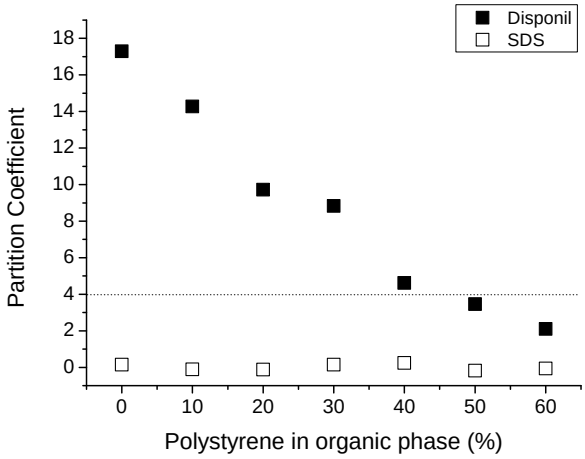

Figure IV.4: Partition coefficient, as defined in Equation IV.2, of SDS (open symbols) and Disponil AFX 1080 (closed symbols) as a function of increasing fraction of PS in organic phase. The dotted horizontal line denotes the value of the partition coefficient at which the surfactant is partitioned equally between the water and the organic (for emulsion composition of 20% organic phase).

Note that commercially available Disponil AFX 1080 contains a distribution of surfactants characterized by different lengths of the ethylene-oxide chain, albeit peaked at 10 units. These different surfactants are likely to partition differently between the two phases. By ^{1}H NMR analysis, it was possible to measure the average number of ethylene oxide groups of the surfactants in the aqueous phase (see Figure IV.5).

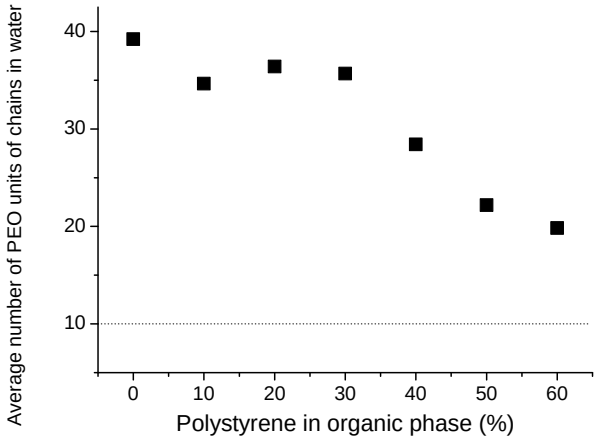

Figure IV.5: Average number of ethylene oxide units of the surfactant molecules residing in the aqueous phase with increasing fraction of PS in organic phase.

As expected, surfactants with a larger number of ethylene-oxide groups displayed a higher propensity to reside in the aqueous phase. As the amount of PS in the organic phase increases the average number of ethylene oxide units decreases approaching the value of 10.

To further examine our hypothesis that secondary nucleation is triggered by a late release of surfactants from the organic phase, we conducted an additional set of experiments under semi-batch conditions with slow addition of the monomer. Under these conditions the monomer concentration remains low throughout the experiment and the effect of surfactant partitioning should therefore be avoided.

In the case of SDS the evolution of particle size and surface tension follow a similar trend to the reaction in batch, although with a much smaller particle size as a result of the low rate of particle growth (see Figure IV.6). [25, 26]

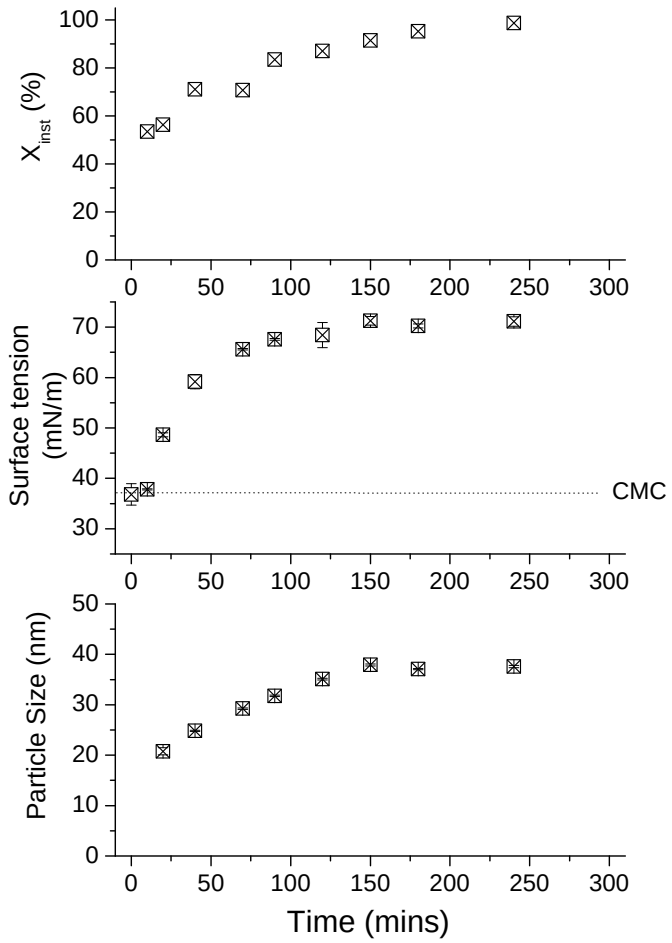

Figure IV.6: Evolution of instantaneous conversion, X_{inst}, surface tension and particle size during the semi-batch emulsion polymerization of styrene using SDS as surfactant (Run 7).

As particles are nucleated, the concentration of surfactant in the aqueous phase is decreased due to adsorption to the newly formed water–polymer interface. The particle size is small and thus rate of polymerization is high, resulting in a high instantaneous conversion for the duration of the reaction.

In contrast, the reactions conducted using the nonionic surfactant showed very different behavior in semibatch compared to batch emulsion polymerization. In the early stage of the reaction, the concentration of surfactant is above the CMC and thus nucleation of particles decreases the amount (and thereby, the concentration) of surfactant in the aqueous phase because it adsorbs to the newly formed particles (see Figure IV.7).

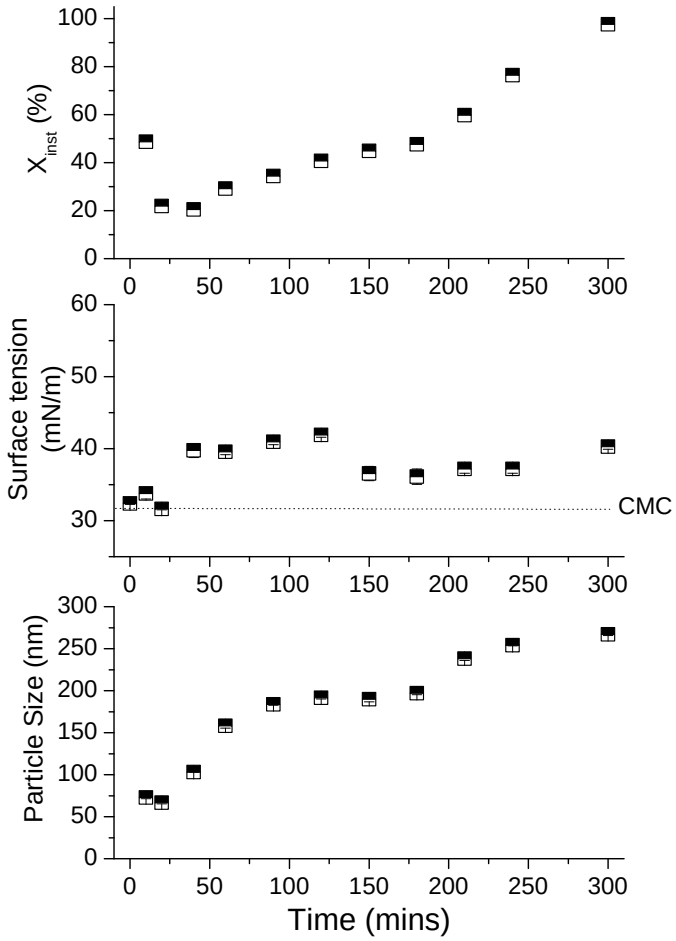

Figure IV.7: Evolution of instantaneous conversion, X_{inst}, surface tension and particle size during the semi-batch emulsion polymerization of styrene using Disponil AFX 1080 as surfactant (Run 8).

Compared to the reaction with SDS, the particle size was larger which results in a lower rate of polymerization and as a consequence the reaction did not proceed under starved conditions, namely the concentration of monomers inside the particles was higher than for a typical semi-batch reaction. For this reason, we suspect that some surfactants were able to partition to the organic phase and at later stages of the reaction were released to the aqueous phase. This explains the small reduction in surface tension at around 130 minutes in Figure IV.7. Crucially however, the amount of surfactant in the aqueous phase does not reach the CMC and thus secondary nucleation does not occur. The result is a monodisperse particle size distribution standing in stark contrast to the results from batch polymerizations. The absence of any secondary nucleation in the semi-batch polymerization using Disponil AFX 1080 was further evidenced by the highly monodisperse nature of the latex as revealed by SEM (see Figure IV.8).

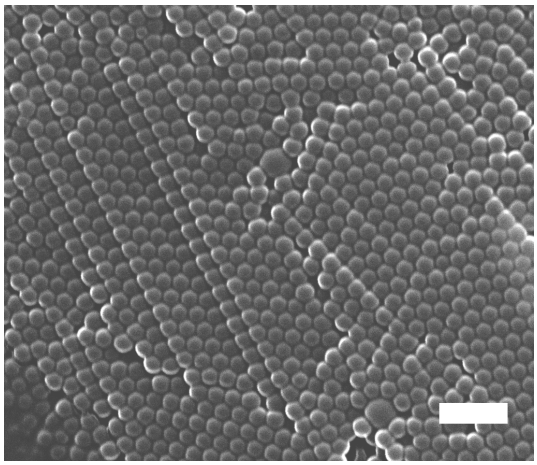

Figure IV.8: SEM image of latex produced by semi-batch emulsion polymerization of styrene using Disponil AFX 1080 (Run 8). The white scale bar represents 1 micron.

To understand at the molecular level the absorption of a nonionic surfactant (10PEO6PE) into a styrene-rich organic phase we performed molecular dynamics (MD) simulations. First, the adsorption character of the surfactant at the organic-phase–water interface was investigated, and second, potential spontaneous absorption into the organic phase was examined. The results obtained with the nonionic surfactant were then compared to those with an ionic surfactant (SDS). It is reasonable to assume that the absorption into a styrene-rich organic phase, and later, the release from a PS-rich phase arise because the strength of binding of the surfactant to styrene is stronger than that to PS. Therefore, in the first series of simulations we calculated the potential of mean force (PMF) of pulling an adsorbed 10PEO6PE surfactant away from the interface, towards the water phase, for three different surfactant concentrations. In this case the organic phase was either neat PS (results taken from our previous work in Chapter III [11]) or neat styrene. The results are shown in Figure IV.9 which suggests it is not possible to attribute this peculiar behavior of the nonionic surfactant to different binding strengths.

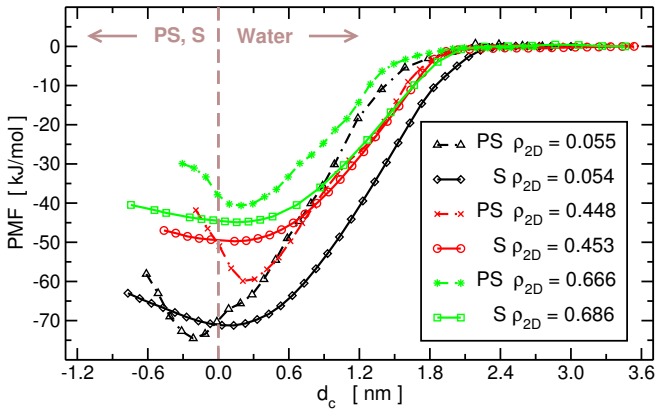

Figure IV.9: The (Gibbs) free energy profile of pulling away one 10PEO6PE surfactant from the organic-phase/water interface into the water phase as a function of the constrained distance, d_c. Different curves correspond to different 2D-densities (in mg/m^2) of the surfactant. Dashed lines are for PS and solid lines are for styrene. The brown vertical dashed line marks the interface.

The depths of the minima of the PMFs (which occur around the same location with respect to the interface) display similar values for the two organic phases, except for $\rho_{2D} \simeq 0.4$ where binding to PS is found to be stronger. Nevertheless, the shape of minima is different. Whereas for PS the minima are well defined, indicating the surfactant experience substantial penalty when pushed farther into the organic phase, for styrene the minima are very shallow and at higher concentrations are almost completely flattened. This means that at high concentrations, there is hardly any penalty for the surfactant to penetrate and adsorb at, the styrene phase. In Figure IV.10 we display the last configuration at each surfactant concentration for the simulations with PS and styrene.

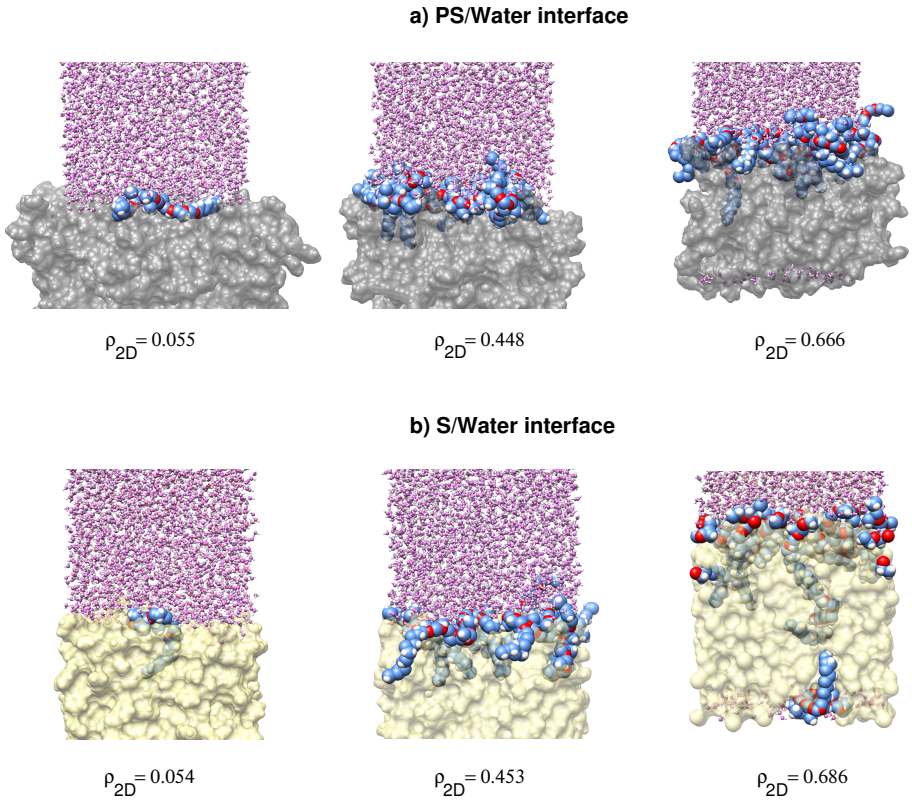

Figure IV.10: Side view of instantaneous configurations of the simulation box of the 10PEO6PE surfactants adsorbed at equilibrium (i.e. at zero pull-force) at (a) PS/water interface and (b) styrene/water interface for the three 2D-densities (in mg/m^2) studied. The poly(styrene) and styrene are shown in a surface representation colored gray and beige, respectively. Water molecules are colored in pink with a ball-and-stick representation. The carbon, oxygen, and hydrogen atoms of the surfactant are shown as space filling spheres colored in blue, red, and white, respectively. For clarity, the snapshots do not capture the entire length of the simulation box along the z-axis (normal to the interface), nevertheless, the same figure displaying the entire simulation boxes is given in Figure A II.20 in Appendix II.

For PS, the head groups of the surfactants are always at the PS–water interface whereas the hydrophobic tails can sometimes enter the organic phase. In contrast, for styrene at the two highest concentrations the entire 10PEO6PE surfactant penetrates the organic phase, and in fact, at the highest concentration one surfactant even passed through the whole styrene phase and adsorbed at the opposite interface that was initially devoid of surfactants. Obviously once the devoid interface becomes accessible, the concentration of the surfactant at equilibrium at both interfaces should be equal because of the 2-fold symmetry of the system. Therefore, if the starting conformation includes surfactants only at one interface the simulation time to reach equilibrium will be, unnecessarily, very long.

As a consequence, we constructed another series of simulations in which the starting configurations include the same concentration of surfactant at both interfaces. In this case, we also considered different chemical compositions of the binary organic phase, in particular, we successively increased the percentage of monomeric styrene, inside PS, in steps of 25%. These different compositions of S/PS in the organic phase correspond to different stages of the polymerization process. In Figure IV.11 we display the density profiles along the z-axis for all different organic phases at surfactant density (i.e., the density initially put at the interface) of ρ_{2D}=1.61±0.09 mg/m^2, alongside snapshots of the last configuration of the corresponding simulations.

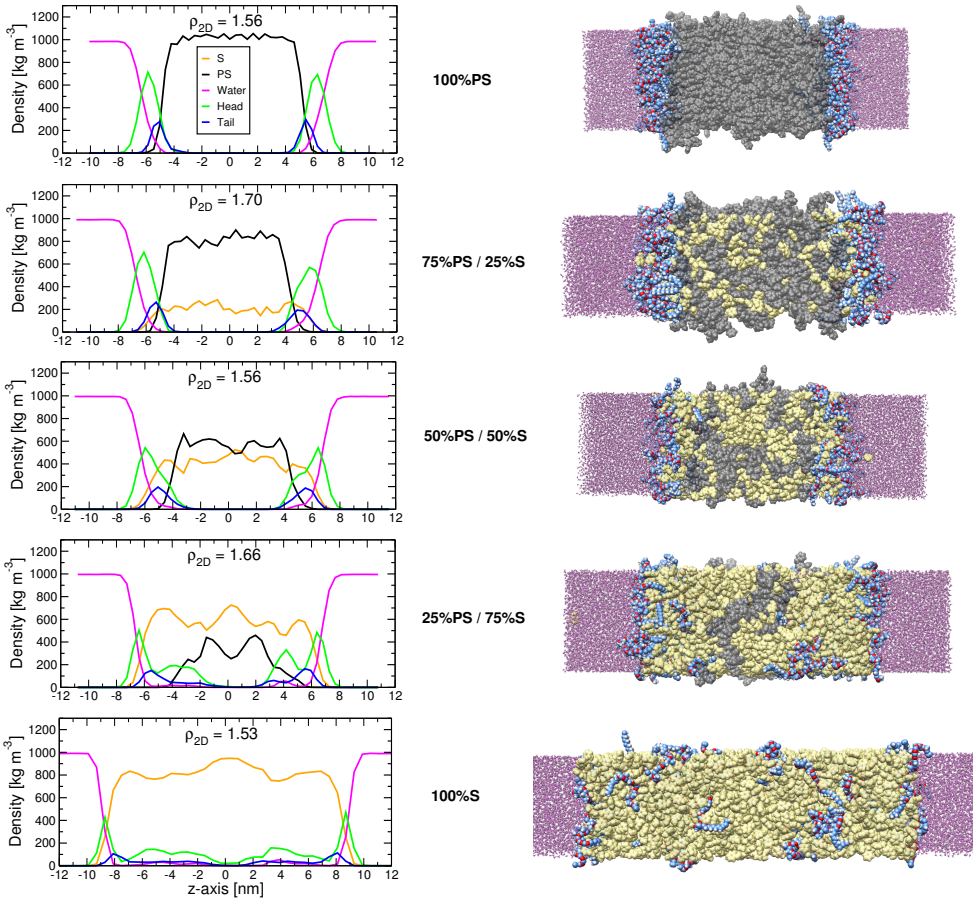

Figure IV.11: Left panel: Density profiles along the z-axis for the five systems with different PS/S binary compositions of the organic phase with the nonionic surfactant 10PEO6PE. The surfactants were placed initially at the two interfaces at 2D-density of 1.61±0.09 mg/m^2 and their profiles are decomposed into heads and tails. Right panel: A snapshot of the last configuration of the corresponding simulations. Color code is the same as in Figure IV.10.

For the systems with 100% PS, 75% PS, and 50% PS, the hydrophilic head and hydrophobic tail of the surfactants are at the interface where the former is positioned more towards the water phase and the latter towards the organic phase. However, a closer inspection of the density profiles of these systems reveals that the surfactants shift into the organic phase with the increase of the content of styrene. Notably, at 50% content of PS there is an onset of a second peak in the distribution of the surfactants heads that is closer to the organic phase, and a concomitant extension of the tail of the water distribution around this second peak position. These trends are augmented in 25% PS and 0% PS (i.e., 100% S), however, in these two systems some of the surfactants can be clearly classified by visual inspection as being completely dissolved (or absorbed) in the organic phase. For 100% S, the density distribution of the surfactants is non-zero throughout the entire styrene phase. These are unexpected results given the common working assumption that below the CMC surfactants adsorb at the interface, and above the CMC they form micelles in the aqueous phase.

We now examine the extent of the absorption of the surfactant into the organic phase for different concentrations of surfactants initially placed at the interface. A surfactant is considered to be inside the organic phase if the z-coordinate of its first tail carbon atom (the atom covalently bonded to the oxygen atom of the head), z_s, satisfies the condition $(-z_i + 2.5\ \text{nm}) < z_s < (+z_i - 2.5\ \text{nm})$, where $+z_i$ and $-z_i$ are the intersection points the two interfaces' lines make with the z-axis. The distance of 2.5 nm away from the interfaces lines represents the region towards the organic phase that is still considered to be the interface.[2] At equilibrium, the chemical potential of the surfactant

[2]Its value was determined from the distance in the density profile between the point the distribution of the head atoms vanishes and the interface line, for a case when no surfactant absorption was detected, i.e., for the system with 100% PS as shown in Figure IV.11.

at the interface equals its chemical potential inside the organic phase. This equality determines the partitioning of the surfactant into these two phases (see Equation 3 in the Appendix II), and therefore, in Figure IV.12a we plot its 3D-density in the organic phase as a function of its 2D-density at the interface. For the systems of 100% PS and 75% PS, the organic phase entirely lacks any surfactant. The 50% PS (50% S) phase supports very small density of surfactant starting at $\rho_{2D} \sim 0.7$ mg/m^2. However as the percentage of styrene increases, i.e. the systems of 75% S and 100% S, there is a substantial increase in the concentration of the surfactant absorbed inside the organic phase. Nevertheless even at 100% S, there is still a critical density at the interface below which the surfactant does not absorb into the organic phase. The values of this critical density are $\rho_{2D} \sim 0.7$ and 0.3 mg/m^2 for 75% S and 100% S, respectively. Above these points, we observe a direct correlation between the surfactant concentration in the organic phase with that at the interface. The curve for 100% S seems to be linear (with a correlation coefficient of 0.983) as dictated by the equality of the chemical potentials (see Equation 3 in Appendix II). Furthermore, the slopes of the lines in Figure IV.12a reflect the propensities of the different organic phases to absorb the surfactants. In Figure A II.21 and Equation 7 in Appendix II we show that the system with 75% S absorbs more, and the system with 50% S absorbs less, surfactants than the amount predicted based on a linear interpolation of the composition of styrene and PS in the organic phase.

Note that our system contains three media in which the surfactant can accumulate, and therefore, there is another equilibrium between the surfactants at the interface and those in the aqueous phase. In fact experimentally, this equilibrium is more relevant to the changes observed during emulsion polymerization (e.g. Figure IV.2). In the previous work in III [11] we found that only at

high densities of the surfactant at the interface does the difference in free energies between adsorption at the interface and dissolution in the aqueous phase is small enough to support significant partitioning into water. Thus, these two equilibria set in successively and not in parallel. In other words, the accumulation of surfactant in the water phase will start only after the adsorption (at the interface) and absorption (inside the organic phase) reached their maximum capacities. This maximum amount of surfactant, Γ_{max}, is estimated by,

$$\Gamma_{max} = \rho_{2D,max} A + \rho_{3D,max} V \quad , \tag{IV.3}$$

where A is the total interfacial area and V is the total volume of the organic phase.

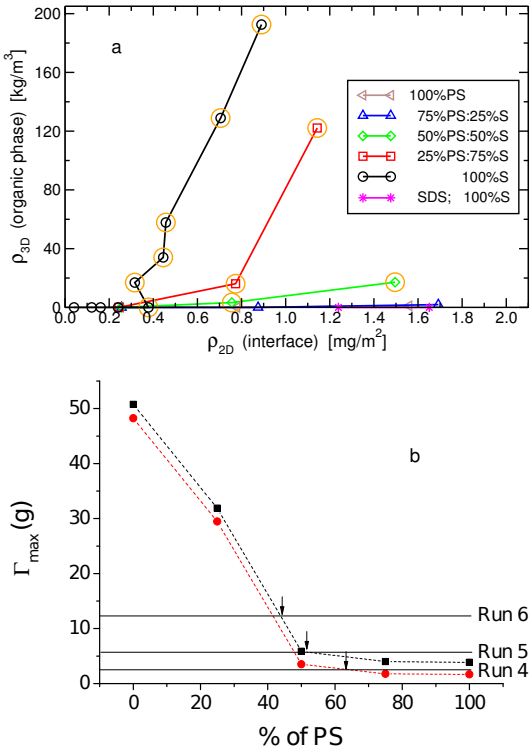

Figure IV.12: (a) The density of the 10PEO6PE nonionic surfactant absorbed inside the organic phase as a function of its density adsorbed at the interface in equilibrium. Note that whereas the former is calculated using the three-dimensional volume of the organic phase the latter uses the two-dimensional area of the interface. The different curves corresponds to different chemical compositions of the organic phase. Data points surrounded by orange circles were considered for subsequent analysis in Figure A II.21 in Appendix II. Results from simulations of SDS ionic surfactant with 100% styrene as the organic phase are also shown. (b) Correlation of the maximum amount of 10PEO6PE surfactant that can be both adsorbed at the interface and absorbed into the organic phase, Γ_{max}, with varying PS content. In these calculations we considered the mass of the organic phase the same as in the experiment (100 g) and the diameter of the particles to be 250 nm (black squares) and 600 nm (red circles). The amounts of surfactant used in emulsion polymerizations using Disponil AFX 1080 corresponding to the Runs 4, 5 and 6 from Table 1 are denoted by horizontal lines.

By extrapolating the data shown in Figure IV.12a to the point which corresponds approximately to the maximum packing density of the surfactant ($\rho_{2D,max}$=1.6 mg/m^2), the value of $\rho_{3D,max}$ (organic phase) can be obtained. Figure IV.12b shows the variation of Γ_{max} for varying PS fraction. The different curves correspond to particles with different diameters, yet under the constraint that the total mass of the organic phase is constant and equals 100 g (see experimental conditions in Table IV.1). At low PS content large amounts of surfactant can be absorbed into the organic phase and hence the value of Γ_{max} is large. As the PS content increases, Γ_{max} decreases substantially and above 75% PS its value remains practically constant with all surfactant being adsorbed at the interface and no absorption occurring. The value of Γ_{max} is also affected by the particle size, with smaller particle sizes having higher surface area for adsorption, but as the total organic phase volume is constant, the extent of absorption into the organic phase is not affected.

We now relate the value of Γ_{max} obtained from the simulation to the observation of a conversion dependent secondary nucleation step in the emulsion polymerization of styrene. When the amount of surfactant in the system is less than Γ_{max}, all surfactant molecules are removed from the aqueous phase and occupy the particles' interface and potentially also their interior. However, when the amount of surfactant in the system is greater than Γ_{max}, excess surfactant will reside in the aqueous phase. Secondary nucleation occurs as a result of an increase in concentration of surfactant in the aqueous phase, thus, the point at which Γ_{max} becomes smaller than the total amount of surfactant introduced to the system should signifies the onset of secondary nucleation. In Figure IV.12b the amounts of surfactant used in Runs 4, 5 and 6 (see Table IV.1) are shown as horizontal lines and the intersection points with the curves of Γ_{max}, accounted by the particle size, are marked by arrows. It can be seen that these points

are at PS content of approximately 63%, 50% and 45% for Run 4, 5 and 6, respectively, which corresponds well with the observation of the occurrence of secondary nucleation in the emulsion polymerization at conversions of approximately 65%, 55% and 40% as shown in Figure IV.2.

The penalty for the surfactant to enter the organic phase is the loss of hydrogen bonds between the head groups and the aqueous solution. To partially render the surfactant intrusion easier, water molecules accompanied this absorption process as evidenced in the density profiles in Figure IV.11. In Figure IV.13 we calculated the number of water molecules absorbed inside the organic phase (applying the same criteria described above for the surfactant) and plotted it against the number of absorbed surfactants. A strong correlation is evidenced for the three systems exhibiting surfactant absorption. If we approximate the curves as straight lines we find from the slopes that the number of accompanying water molecules per surfactant is 1.3, 2.8, and 5.0 for the systems with 50% S, 75% S, and 100% S, respectively.

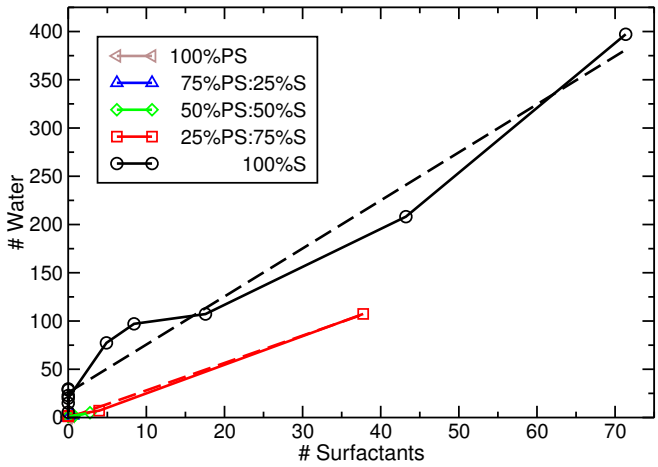

Figure IV.13: The number of water molecules as a function of the number of surfactants, both of which are absorbed inside the organic phase. The corresponding dashed lines are linear regression fits.

In Figure IV.14 we plot the number of hydrogen bonds the head group of the surfactant forms with the surrounding water molecules as a function of the surfactant position along the z-axis.

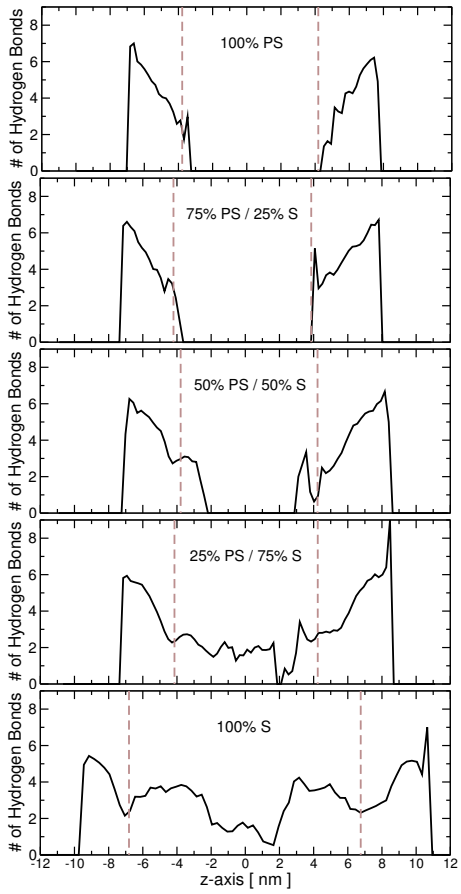

Figure IV.14: The average number of hydrogen bonds (per surfactant) the nonionic surfactant forms with its surrounding water molecules as a function of its z-axis (as determined by z-coordinate of its first tail carbon atom covalently bonded to the oxygen atom of the head) for the five different organic phases for the systems shown in Figure IV.11. The region between the dashed brown vertical lines denotes the location we considered to be the interior of the organic phase.

Although there is a reduction in the number of hydrogen bonds compared with the values observed at the interface, the interaction between the absorbed surfactant and the intruding water molecules is still substantial ranging from four to two hydrogen bonds per surfactant. Note that even when no surfactant is absorbed inside the organic phase or adsorbed at the interface, the number of water molecules inside the organic phase, albeit at low concentrations, is not zero. This is shown in Figure A II.22 in Appendix II which reveals a sharp increase in the water density inside the organic phase of 100% S reaching a value of 1.5–3.0 kg/m^3 which is larger by a factor of 2.5–5.0 than that found experimentally. [27] We also performed similar simulations with 100% S for the organic phase but instead of 10PEO6PE we used SDS as the surfactant. Here, in contrast to the results for the nonionic surfactant, no absorption (zero density) into styrene was observed and the density distributions of the head and tail of SDS are clearly confined only to the interface region (Figure IV.15).

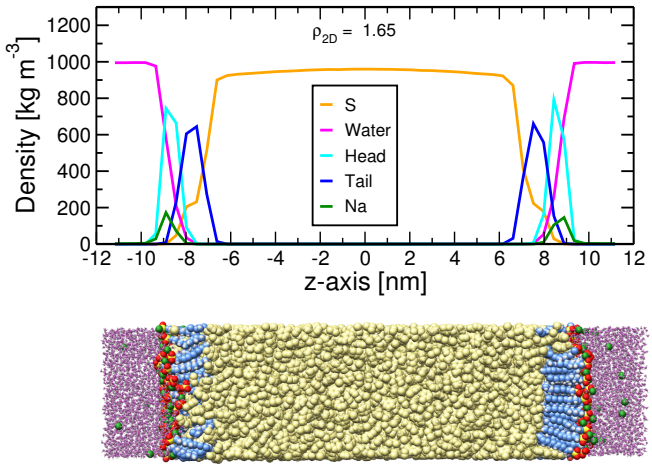

Figure IV.15: The density profile along the z-axis (upper panel) and a snapshot of the last configuration (lower panel) for the simulations with SDS surfactants at 2D-density of 1.65 mg/m^2. The color code is the same as in Figure IV.10, sulfur atoms of SDS and the sodium counterions are shown as yellow and green spheres, respectively. Similar results, of no absorption of SDS into the styrene phase, were also obtained with a lower 2D-density of 1.24 mg/m^2.

Given that 100% S is the organic phase with the highest propensity to absorb the nonionic surfactant, we anticipate to observe zero densities also for systems containing any mixture of styrene and PS. As we found in our previous study in III, [11] the self-assembly of SDS at the interface is very ordered (compared with that of the PEO–PE block copolymer surfactants), and similarly, we attribute its exclusion from a styrene-rich organic phase to its small and strongly hydrophilic head group. Such a physio-chemical character of the head group would impose a large energetic barrier upon intrusion into a medium with a low dielectric constant. Why then, the nonionic surfactant is able to absorb into styrene and not into PS. We speculate it is because at room temperature styrene is liquid whereas PS is solid. This relationship of states between monomers and their corresponding polymers is likely to be the same for other materials, and therefore, the effect induced by ionic and nonionic surfactants during the course of the polymerization reaction is anticipated to be similar to that described in this work.

IV.4 Conclusions

In conclusion, we have demonstrated that nonionic surfactants, such as poly(ethylene glycol)–poly(ethylene) block copolymers, exhibit substantially different behavior in emulsion polymerization as compared to the widely employed ionic surfactant SDS. The emulsion polymerization with nonionic surfactants is characterized by an increase in the rate of polymerization and a second nucleation period, which can be related to an unexpected increase in the surfactant concentration at advanced stages of the reaction. This can be explained by the partitioning of the surfactant into the styrene-rich phase followed by its release as the reaction progresses and the organic phase becomes rich in poly(styrene). Using atomistic molecular dynamics simulations, it was shown that when adsorbed above a critical concentration at the interface nonionic surfactants can absorb into the hydrophobic medium. For hydrophobic phases with mixed compositions of styrene and poly(styrene), we found the onset of surfactant partitioning at a content around (or just above) 50% styrene. Alongside the dissolution of the surfactant, water molecules penetrate the hydrophobic phase as well. The number of accompanying water molecules per surfactant depends on the composition of the hydrophobic medium. For ionic surfactants, such as SDS, no absorbance of surfactant has been observed under any conditions (e.g. neat styrene at high surfactant concentrations). It is likely that nonionic surfactants are able to absorb into these styrene-rich organic phases because their head groups are not strongly hydrophilic rendering the energetic penalty, relatively, small.

References

[1] Chanda, J.; Bandyopadhyay, S. Molecular Dynamics Study of a Surfactant Monolayer Adsorbed at the Air/Water Interface, *J. Chem. Theory Comput.* 2005, *1*, 963–971.

[2] Tummala, N. R.; Shi, L.; Striolo, A. Molecular dynamics simulations of surfactants at the silica-water interface: Anionic vs nonionic headgroups, *J. Colloid Interface Sci.* 2011, *362*, 135–143.

[3] Li, Z.; Dyk, A. K. V.; Fitzwater, S. J.; Fichthorn, K. A.; Milner, S. T. Atomistic Molecular Dynamics Simulations of Charged Latex Particle Surfaces in Aqueous Solution, *Langmuir* 2016, *32*, 428–441.

[4] Wu, R.; Qiu, X.; Shi, Y.; Deng, M. Molecular dynamics simulation of the atomistic monolayer structures of N-acyl amino acid-based surfactants, *Mol. Sim.* 2017, *43*, 491–501.

[5] Esselink, K.; Hilbers, P.; van Os, N.; Smit, B.; Karaborni, S. Molecular dynamics simulations of model oil/water/surfactant systems, *Colloids Surf. A Physicochem. Eng. Asp.* 1994, *91*, 155–167.

[6] Chen, J.; Hao, J. Molecular dynamics simulation of cetyltrimethylammonium bromide and sodium octyl sulfate mixtures: aggregate shape and local surfactant distribution, *Phys. Chem. Chem. Phys.* 2013, *15*, 5563–5571.

[7] Tang, X.; Koenig, P. H.; Larson, R. G. Molecular Dynamics Simulations of Sodium Dodecyl Sulfate Micelles in Water - The Effect of the Force Field, *J. Phys. Chem. B* 2014, *118*, 3864–3880.

[8] Yang, C.; Sun, H. Surface-Bulk Partition of Surfactants Predicted by Molecular Dynamics Simulations, *J. Phys. Chem. B* 2014, *118*, 10695–10703.

[9] Horn, H. W.; Swope, W. C.; Pitera, J. W.; Madura, J. D.; Dick, T. J.; Hura, G. L.; Head-Gordon, T. Development of an improved four-site water model for biomolecular simulations: TIP4P-Ew, *J. Chem. Phys.* 2004, *120*, 9665–9678.

[10] Li, Z.; Fichthorn, K. A.; Milner, S. T. Surfactant binding to polymer-water interfaces in atomistic simulations, *Langmuir* 2016, *32*, 7519–7529.

[11] Meconi, G. M.; Ballard, N.; Asua, J. M.; Zangi, R. Adsorption and Desorption Behavior of Ionic and Nonionic Surfactants on Polymer Surfaces, *Soft Matter* 2016, *12*, 9692–9704.

[12] Hess, B.; Kutzner, C.; Van Der Spoel, D.; Lindahl, E. Gromacs 4: algorithms for highly efficient, load-balanced, and scalable molecular simulation, *J. Chem. Theory Comput.* 2008, *4*, 435–447.

[13] Bussi, G.; Donadio, D.; Parrinello, M. Canonical Sampling through Velocity Rescaling, *J. Chem. Phys.* 2007, *126*, 014101.

[14] Berendsen, H. J.; Postma, J. v.; van Gunsteren, W. F.; DiNola, A.; Haak, J. Molecular dynamics with coupling to an external bath, *J. Comput. Phys.* 1984, *81*(8), 3684–3690.

[15] Darden, T.; York, D.; Pedersen, L. Particle Mesh Ewald: An N-log(N) Method for Ewald Sums in Large Systems, *J. Chem. Phys.* 1993, *98*, 10089–10092.

[16] Essmann, U.; Perera, L.; Berkowitz, M. L.; Darden, T.; Lee, H.; Pedersen, L. G. A Smooth Particle Mesh Ewald Method, *J. Chem. Phys.* 1995, *103*, 8577–8593.

[17] Miyamoto, S.; Kollman, P. A. SETTLE: An Analytical Version of the SHAKE and RATTLE Algorithms for Rigid Water Models, *J. Comp. Chem.* 1992, *13*, 952–962.

[18] Hess, B.; Bekker, H.; Berendsen, H. J. C.; Fraaije, J. G. E. M. LINCS: A Linear Constraint Solver for Molecular Simulations, *J. Comp. Chem.* 1997, *18*, 1463–1472.

[19] Luzar, A.; Chandler, D. Structure and hydrogen bond dynamics of water-dimethyl sulfoxide mixtures by computer simulations, *J. Chem. Phys.* 1993, *98*, 8160–8173.

[20] Mukerjee, P.; Mysels, K. J. *Critical Micelle Concentrations of Aqueous Surfactant Systems;* U.S. National Bureau of Standards: Washington, DC, 1971.

[21] Sundberg, D. C.; Hsieh, J. Y.; Soh, S. K.; Baldus, R. F. In *Emulsion Polymers and Emulsion Polymerization*; Bassett, D. R., Hamielec, A. E., Eds.; American Chemical Society: Washington, D. C., 1981; chapter 20, pages 327–343.

[22] Fernandez, A. M.; Held, U.; Willing, A.; Breuer, W. H. New green surfactants for emulsion polymerization, *Prog. Org. Coatings* 2005, *53*, 246–255.

[23] Özdeğer, E.; Sudol, E. D.; El-Aasser, M. S.; Klein, A. Role of the nonionic surfactant Triton X-405 in emulsion polymerization. I. Homopolymerization of styrene, *J. Polym. Sci. A Polym. Chem.* 1997, *35*, 3813–3825.

[24] Smith, W. V.; Ewart, R. H. Kinetics of Emulsion Polymerization, *J. Chem. Phys.* 1948, *16*, 592–599.

[25] Nunes, J. d. S.; Asua, J. M. Theory-Guided Strategy for Nanolatex Synthesis, *Langmuir* 2012, *28*, 7333–7342.

[26] Sajjadi, S. Nanoparticle Formation by Monomer-Starved Semibatch Emulsion Polymerization, *Langmuir* 2007, *23*, 1018–1024.

[27] Lane, W. Determination of Solubility of Styrene in Water and of Water in Styrene, *Ind. Eng. Chem. Anal. Ed.* 1946, *18*, 295–296.

Chapter V

Adsorption of CO_2 Gas on Graphene-Polymer Composites

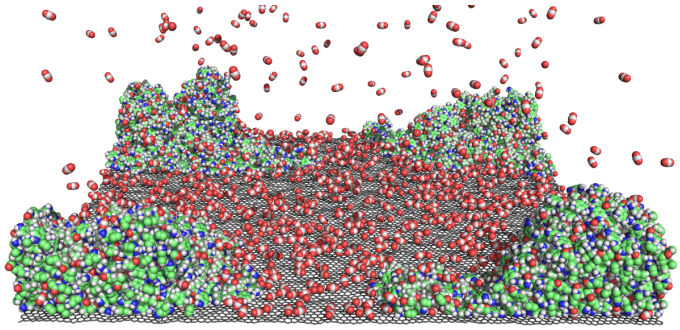

Contents

The results in this Chapter were submitted in: Polymers.

Giulia Magi Meconi, Radmila Tomovska and Ronen Zangi,

Adsorption of CO_2 Gas on Graphene-Polymer Composites.

V.1 Introduction

In this work we perform atomistic molecular dynamics simulations (MD) to investigate the capture of CO_2 gas by several graphene-polymer composite systems and characterize the discrimination with respect to the capture of N_2 and CH_4. Six different types of polymers, with polymer/graphene mass ratio of one, are considered and their performance is compared to that of a bare-graphene system. We find that the adsorption of CO_2 increases with the increase in the number of protic groups in the polymer such as amines and amides. The number of protic groups in the polymer also determine the morphology of the polymer on graphene; those with large numbers tend to self-aggregate whereas those lacking such groups spread homogeneously on the graphene surface. For all the graphene-polymer composites, the adsorption of CO_2 is favored relative to N_2 and CH_4.

V.2 Methods

V.2.1 Computational details

We performed molecular dynamics simulations to model the adsorption of a mixture of three gases, CO_2, N_2, and CH_4 at graphene-polymer (GP) composite surfaces. Six different polymers, drawn in Figure V.1, were considered: poly(methyl methacrylate) (PMMA), poly(2-aminoethyl methacrylate) (PEAM), poly(3-diamin-(aminomethyl)propyl methacrylate) (DAPM), poly(aniline methacrylamide) (PAAM), poly(N-(3,5-diaminophenyl)methacrylamide) (PDAFMA), and poly(styrene) (PS). For comparison, we also conducted simulations in the absence of any polymer (referred to as bare-graphene simulations).

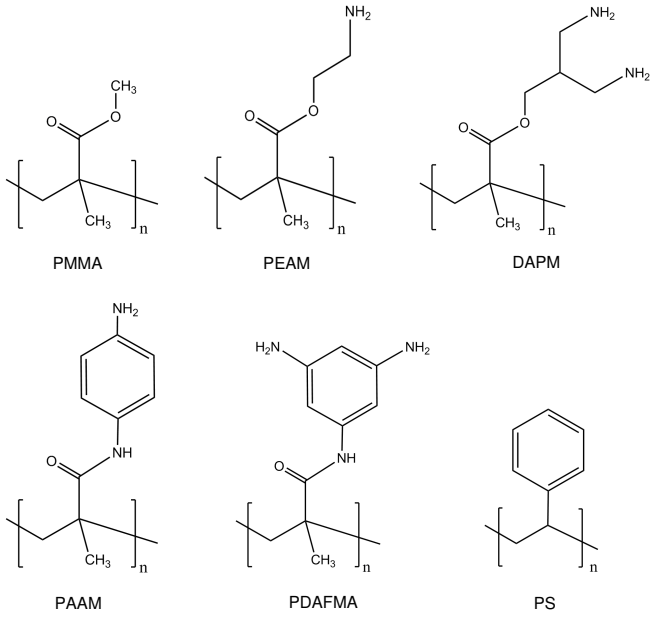

Figure V.1: The chemical structure of the polymers considered in this study. The abbreviated names given correspond to, PMMA: poly(methyl methacrylate), PEAM: poly(2-aminoethyl methacrylate), DAPM: poly(3-diamin-(aminomethyl)propyl methacrylate), PAAM: poly(aniline methacrylamide), PDAFMA: poly(N-(3,5-diaminophenyl)methacrylamide), and PS: poly(styrene).

A rectangular-shaped box with dimensions of 24.065 nm, 24.668 nm, 64.000 nm, along the x-, y-, and z-axes was used for the simulations. Although, periodic boundary conditions were applied in all three directions, they effectively acted only across the x-, and y-axes. The simulation box consisted of two non-interacting graphene sheets, periodic in the xy-plane, located at z_1=2.0 nm and z_2=62.0 nm. In order to prevent translations of the graphene sheets, the positions of their carbon atoms were restrained along the z-axis by a harmonic potential with a force constant of 1000 kJ/(mol·nm^2). Each chain of polymer consists of seven monomer units. Equal amount of polymer chains were randomly distributed on both graphene sheets, on the (inner) sides that are facing each other via the larger distance (z_2-z_1=60.0 nm). Accordingly, the mixture of gases was placed in that region as well. Experimentally, properties of a GP composite is characterized by the ratio of the polymer mass to that of graphene, m_p/m_G. Therefore, we constructed all systems to have the same polymer/graphene weight ratio, chosen to be equal to 1.020 $\pm$ 0.002. Because the size of the graphene sheets were the same in all systems, this meant that the number of polymer chains was different for the different systems (see Figure A III.13 in Appendix III for details).

The gas mixture contained equal number of molecules of each gas in the system, $N^o_{CO_2} = N^o_{N_2} = N^o_{CH_4} = \frac{1}{3}N^o_{gas}$. For each type of graphene-polymer system we conducted nine simulations with different numbers of N^o_{gas}. When the system reached equilibrium, we calculated the number of molecules, and from this the density, of each gas in the bulk phase of the simulation box (see Tables A III.14, A III.15, and A III.16 in Appendix III). A gas molecule is considered to be in the bulk region if its z-coordinate of its center of mass (com) satisfies, (z_1 + 4.0 nm) $<$ z_{gas} $<$ (z_2 - 4.0 nm). The distance of 4.0 nm away from the graphene sheet was determined by the onset of a homogeneous (con-

stant) behavior of the density profile for all gases. This bulk density was then used to determine the partial pressure, from the pressure–density curves (see below), each gas exerted on the GP surface. A gas molecules is counted as adsorbed to the graphene sheet if the distance from its com to the graphene com, along the z-axis, is smaller than 0.55 nm. This cutoff value roughly corresponds to the first minimum in the density profiles (see for example Figure V.3). Accordingly, a gas molecule is considered adsorbed to the polymer if the distance from its com to any atom of the polymer is smaller than 0.55 nm. The amount of gas molecules adsorbed at the GP composite surface is expressed by its two-dimensional mass density, $\rho_{2D} = m/A$, where m is the mass of the adsorbed gas and A is the area of the two graphene sheets. Two molecules were considered to be hydrogen bonded if the donor–acceptor distance is smaller than 0.35 nm and the hydrogen–donor–acceptor interaction angle is smaller than 30°. [1] Figure A III.23 in Appendix III displays a snapshot of the entire simulation box of one of the G-PDAFMA systems.

All simulations were performed in the canonical ensemble (NVT) using the molecular dynamics package GROMACS version 4.6.5. [2]. The simulation box was fixed during the simulations and a constant temperature of 300 K was maintained by the velocity rescaling thermostat [3] with a coupling time of 0.1 ps. The time step for integrating the equations of motion was set to 2 fs. Bonds stretching and angles bending were described by harmonic potentials. Lennard-Jones (LJ) interactions between unlike atoms were computed using the geometric combination rules of the OPLSAA force-field. The GP composite systems were subjected to a relaxation time of 40 ns, except those with $N°_{gas}$=2700 where the equilibration time was extended to 50 ns. Due to absence of polymer chains in the bare-graphene system, these simulations reached equilibrium much faster and therefore the relaxation time was shortened to 30 ns. Then,

all simulations were continued for additional 10 ns of data collection.

Interactions Parameters

A carbon dioxide molecule was represented by the TraPPE model [4] for which the non-bonded interactions are specified in Table V.1.

Table V.1: The non-bonded parameters for the models of carbon dioxide and nitrogen gases.

	q [e]	σ [nm]	ϵ [kJ/mol]
C (CO_2)	+0.70	0.280	0.224
O (CO_2)	-0.35	0.305	0.657
N (N_2)	-0.482	0.3318	0.303
MW (N_2)	+0.964	0.0000	0.000

In this case, the Lorentz-Berthelot combination rules were used. The carbon-oxygen covalent bond [5] is 0.116 nm long with a force constant of 476976 kJ/(mol·nm^2). We adopted a force constant of 1236 kJ/(mol·rad^2) for the linear O–C–O bond angle from the EPM2 model [6]. The three-site model of Murthy et al. [7] was utilized to describe a nitrogen molecule (see Table V.1). In this model, a positively-charged massless virtual site (MW) is symmetrically placed between the two nitrogen atoms. The covalent bond between the two nitrogens is characterized by an equilibrium distance of 0.1098 nm and a force constant [8] of 138570 kJ/(mol·nm^2). A methane molecule was represented by the OPLSAA force-field [9]. To validate the force-fields described above for CO_2, N_2, and CH_4 gases we performed a series of MD simulations in the NVT ensemble, modeling the homogeneous gas phase, for each of these gases. Seven different densities were considered for which the pressure was calculated

and compared against experimental data [8] obtained from the van der Waals equation of state (see Table A III.17 in Appendix III). The results, which are shown in Figure A III.24 in Appendix III, indicate these models reasonably predict the gas pressure, albeit consistently underestimating its value.

Details of the parameters used to model the flexible graphene sheets (thus including bond stretching and angle bending) are described in a simulation study of Zangi et al., [10] in which the LJ parameters of the carbon atoms, σ_{CC}=0.3851 nm and ϵ_{CC}=0.4396 kJ/mol, were parameterized to mimic single-walled carbon nanotubes [11]. The different polymer chains were modeled using the OPLSAA force-field. The model for PS is taken from our previous works in Chapters III or IV [12, 13] whereas the models for the other polymers are specified in Figures A III.26–A III.30 and Tables A III.18–A III.39 of the Appendix III.

V.3 Results and Discussion

The ability of the proposed graphene-polymer composite surfaces to capture CO_2 gas at 300 K is shown in Figure V.2.

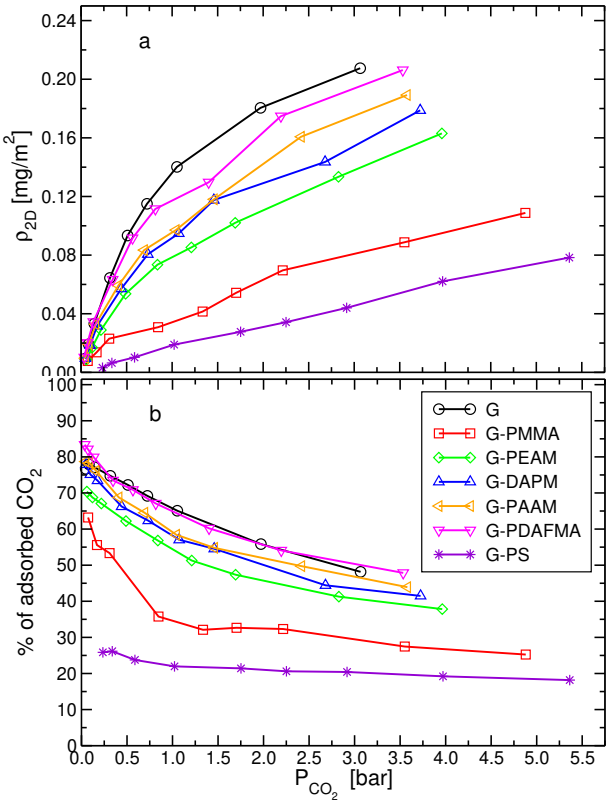

Figure V.2: Adsorption isotherms of CO_2 gas on graphene-polymer composite surfaces, as well as for bare graphene sheet, at 300 K. (a) The two-dimensional density of the CO_2 gas adsorbed. (b) The percentage of the number of CO_2 molecules adsorbed at the surface relative to the total number of CO_2 in the system. Both graphs are plotted as a function of the partial pressure of CO_2 in the system.

In Figure V.2a this is expressed by the two-dimensional mass-density of adsorbed CO_2, at the two surfaces of the simulation box, as a function of its partial pressure. These adsorption isotherms indicate that bare-graphene has the highest capability to adsorb CO_2, slightly better than the best performing graphene-polymer composite system, G-PDAFMA. The other graphene-polymer systems exhibit the following decreasing order of performance in adsorbing CO_2 gas: $G-PAAM > G-DAPM > G-PEAM > G-PMMA > G-PS$. The percentage of CO_2 molecules adsorbed at the surfaces relative to the total number of CO_2 molecules is shown in Figure V.2b. This percentage ranges from 83% to 18% and decreases substantially with the increase of the partial pressure. The latter is manifestation of interactions between the adsorbed molecules. Nevertheless for the G-PS system, which exhibits the lowest ability to adsorb CO_2, the decrease is very mild. In this case, the adsorption isotherm is almost linear and is analogous to Henry's law of the amount of gas dissolved in a liquid. This means that for the G-PS system, the number of gas molecules adsorbed is much smaller than the available adsorbing sites on the graphene-polymer composite system.

In order to investigate the way CO_2 molecules are adsorbed at the graphene-polymer surfaces, we plot in Figure V.3 the density profile of the CO_2 molecules along the z-axis (normal to the graphene sheet) for systems with $N°_{CO_2}$=2700 yielding partial pressures in the range of 1–2 bar.

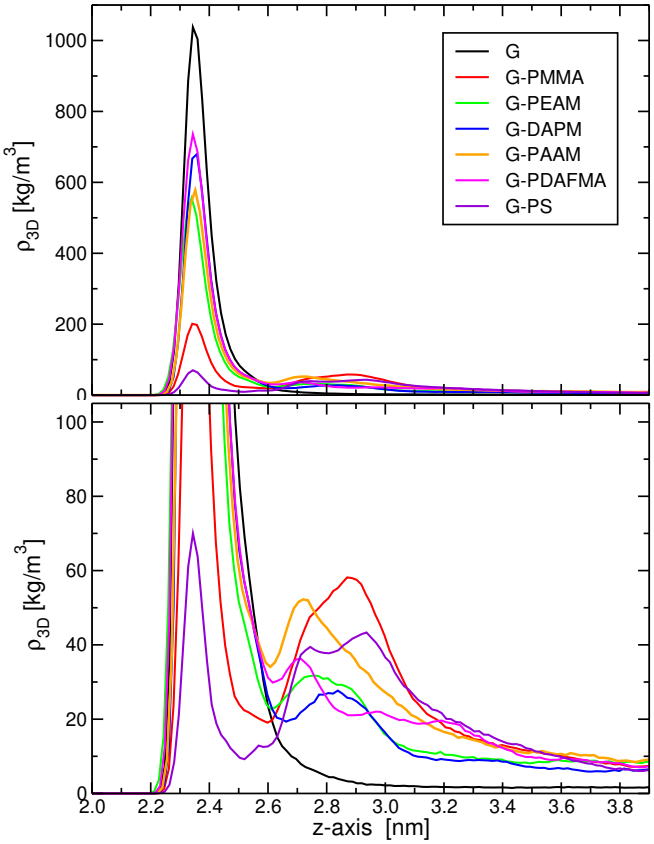

Figure V.3: Upper panel: The density profile of the CO_2 molecules along the z-axis for different graphene-polymer composite systems with $N°_{CO_2}$=2700. These profiles were averaged over the two surfaces in the simulation box by folding the center of mass of the second graphene sheet (at z_2=62.0 nm) onto the first one at z_1=2.0 nm. Lower panel: A zoom-in of the density profiles displaying the second peaks due to adsorption to the polymers.

Except for G-PS and G-PMMA, the first peak away from the graphene sheet is by far the most dominant. For bare-graphene, the distribution is unimodal indicating the formation of only monolayers. This is also true for bare-graphene systems with larger numbers, or higher partial pressures, of CO_2 (profiles not shown). The location of this first peak, 0.35 nm away from the average positions of the carbon atoms of graphene, points to van der Waals contacts. For the graphene-polymer systems, there is a second peak which is broad and for some systems there is even a third peak or a shoulder at distances 0.70–0.96 nm away from graphene. For G-PS the integral of the second and third peaks is significantly larger than that of the first peak, whereas for G-PMMA these integrals are comparable. These second and third peaks originate due to adsorption of CO_2 either inside (i.e. absorption) or at the outer surface of the polymer and are not an indication of multilayer formation of adsorbed CO_2 even at the highest gas pressure studied. The systems with the added polymer exhibit also a slow decay of the CO_2 density along the z-axis and only at around 4.0 nm away from the graphene sheets, does the density adopt a constant value characterizing the 'bulk-region' in the simulation box. This slow decay results from the adsorption to the polymer and its range coincides with the extent of polymer intrusion into the gas phase (see below).

Thus, the CO_2 molecules are adsorbed to the graphene sheet as well as to the chains of the polymer. Nevertheless, although the adsorption to the graphene and the polymer can be done independently, CO_2 molecules are also adsorbed simultaneously to both. In Figure V.4 we display a snapshot of the graphene-polymer interface isolating six CO_2 molecules exhibiting the three different adsorption modes.

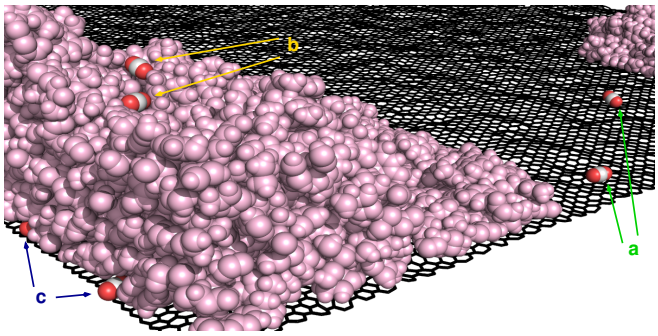

Figure V.4: A snapshot of a segment of the simulation box for the graphene-PDAFMA composite system displaying three different types of adsorption of CO_2 gas at the interface. Adsorption only to the graphene sheet (a), only to the polymer (b), and simultaneously to the graphene and the polymer (c). The graphene sheet is shown as black rods, the polymer atoms as pink spheres, and the carbon dioxide molecules as white and red spheres. For clarity, nitrogen and methane gases, as well as other CO_2 molecules, were removed.

Adsorption only-to-graphene, as well as, simultaneous adsorption to graphene and polymer give rise to the first peaks in Figure V.3. In the latter, the polymer covers the adsorbed molecules, thereby, increasing the adsorption energy albeit at the expense of the graphene-polymer interaction. In the adsorption only-to-polymer, the gas molecules are adsorbed at the surface of, or absorbed inside, the polymer. The population of each adsorption mode is plotted in Figure V.5.

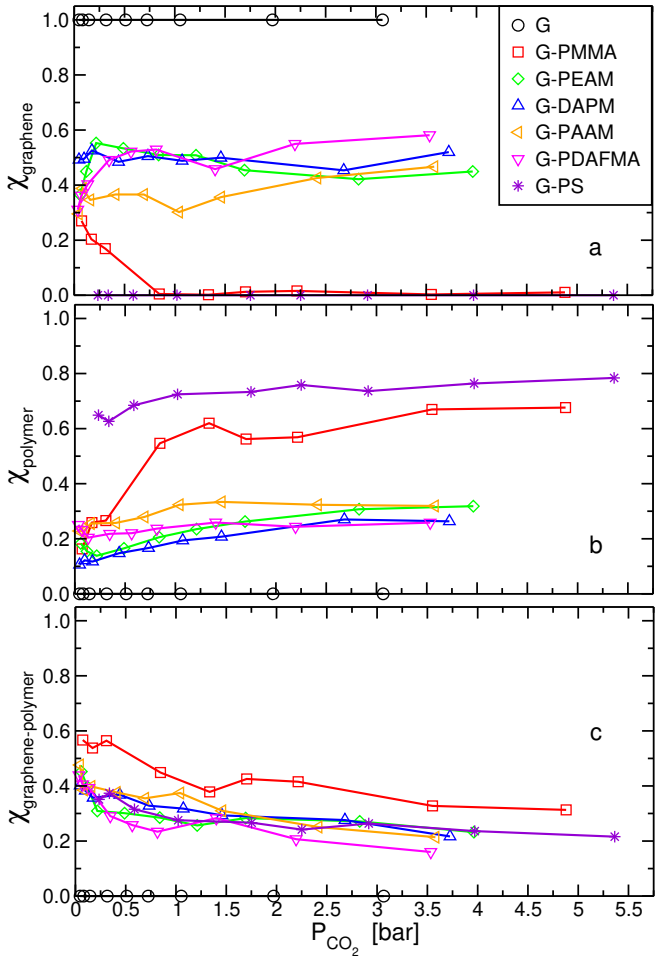

Figure V.5: The decomposition of the adsorbed CO_2 molecules into the different modes of adsorption. The graphs exhibit the fraction of carbon dioxide molecules adsorbed (a) only to the graphene sheet, (b) only to the polymer, and (c) simultaneously to the graphene and the polymer, relative to the total number of CO_2 adsorbed.

G-PS displays a negligible adsorption via the only-to-graphene mode for all partial pressures of CO_2. For G-PMMA, there is a sharp decrease in the adsorption of only-to-graphene, after which the contribution of this adsorption mode is also negligible. Consequently for these two polymer systems, the largest contribution for CO_2 adsorption comes from the only-to-polymer mode. For the other graphene-polymer composite systems, all three adsorption modes contribute substantially. In most cases, the only-to-graphene mode has the largest contribution. The other two adsorption modes are more or less comparable in their populations, where the only-to-polymer and the simultaneous adsorption modes slightly increases and slightly decreases, respectively, with the partial pressure.

Figure V.5 demonstrates there is a large difference between the adsorption mechanism of G-PS and G-PMMA to that of the other graphene-polymer systems. We find the reason G-PS and G-PMMA systems display negligible populations of the only-to-graphene adsorption mode is because these polymers cover completely, or almost completely, the graphene sheet. This is clearly seen in Fig V.6 where we present snapshots of the different polymers adsorbed on the graphene sheet.

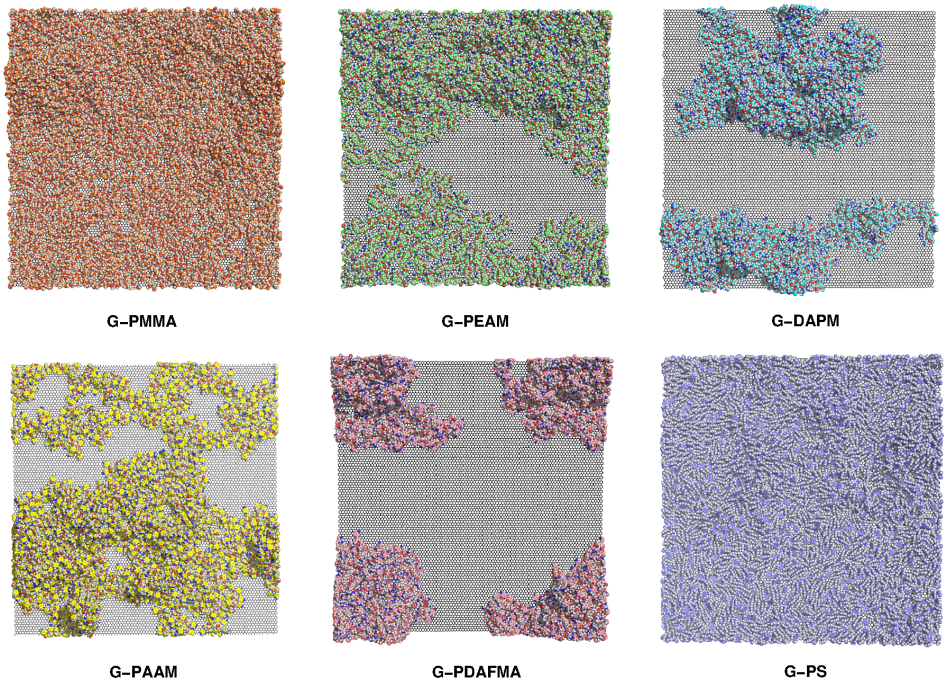

Figure V.6: Snapshots of the structural organization of the different polymers on the graphene sheet. The figures display top-views, of the last configuration, on one of the two graphene-polymer interfaces taken from simulations with a partial pressure of CO_2 at, approximately, 1 bar. For clarity, none of the gas molecules present in the system are displayed. Graphene is shown as black sticks. Polymers are represented as spheres, where hydrogens are colored in white, oxygens in red and nitrogens in blue. Carbon atoms have different colors in each polymer (orange for PMMA, green for PEAM, cyan for DAPM, yellow for PAAM, pink for PDAFMA, and violet for PS).

In contrast, the other graphene-polymer composite systems display different degrees of aggregation of the polymer. In this regard, the polymers can be grouped into those with moderate degree of aggregation (PEAM and PAAM) and those with strong degree of aggregation (DAPM and PDAFMA). The extent of aggregation is a result of the interaction energy within the polymer relative to the interaction between the polymer and graphene. Not surprisingly, each of the monomors of PEAM and PAAM contain one amine group whereas those of DAPM and PDAFMA contain two amine groups. These amine groups are able to form hydrogen bonds with one another and are likely responsible for the polymer-polymer energy that would overcompensate the lost polymer-graphene energy accompanied the process of aggregation. We calculate the number of hydrogen bonds formed between and within the polymer chains in Figure V.7a.

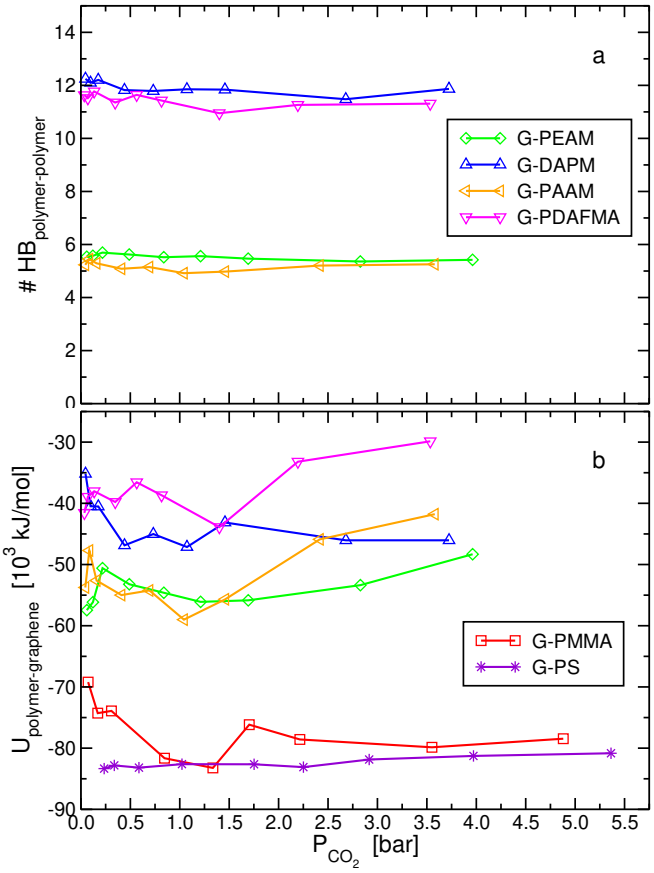

Figure V.7: (a) The number of polymer–polymer hydrogen bonds, per polymer molecule, and (b) the potential energy between the polymer and the graphene sheet, as a function of the partial pressure of CO_2.

The above mentioned grouping of the polymers according to the degree of aggregation they exhibit is apparent in this figure as well. Because PS and PMMA do not contain suitable groups for hydrogen bond formation their corresponding values are zero by definition. DAPM and PDAFMA form similar numbers of intra-polymer hydrogen bonds which are about twice as much as those formed by PEAM and PAAM. Obviously, larger numbers of hydrogen bonds within the polymer strengthen the polymer-polymer interaction energy and will induce aggregation and intrusion into the gas bulk phase. As a consequence, the strength of the interaction of the polymer with the graphene sheet will display the inverse order, as it is found in Figure V.7b. PS and PMMA have the strongest adsorption energy with graphene whereas PDAFMA and DAPM display the weakest adsorption, a trend that correlates well with the formed morphologies shown in Figure V.6. It is worth noting that phenyl aromatic rings are oriented perpendicular to graphene as the backbone chains lie flat on the surface. This is shown in a snapshot in Figure V.8 and in the distribution of the angle between the plane of the phenyl ring and the graphene plane.

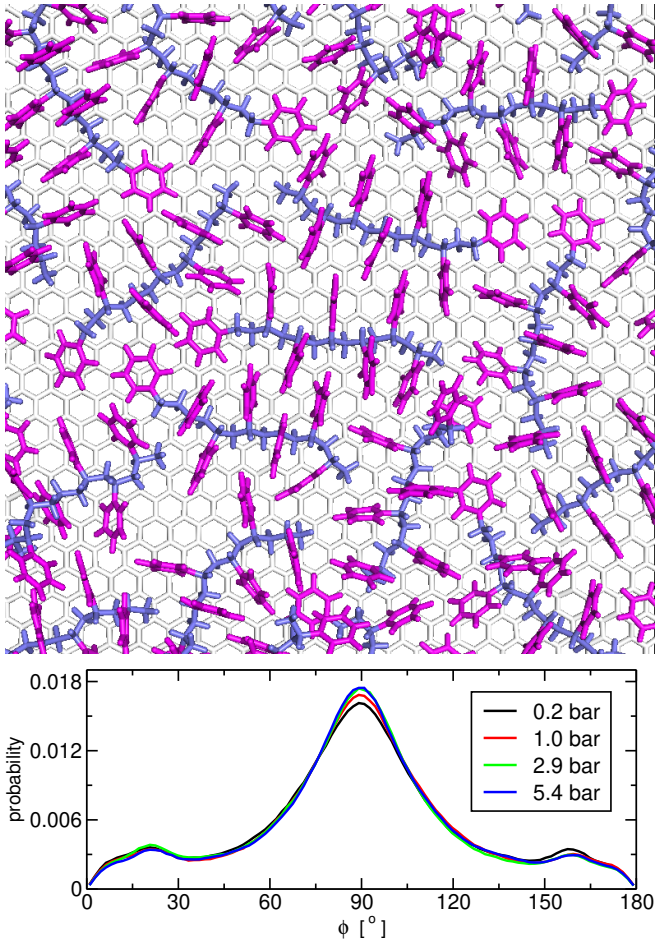

Figure V.8: Top panel: top-view of the poly(styrene) chains on graphene. The phenyl rings are colored in magenta and the backbones in blue. For clarity, all gas molecules were removed from the figure. Lower panel: normalized distribution of the angle, ϕ, between the plane of the phenyl ring and the z-plane, at four different partial pressures of CO_2.

The distribution has a pronounced maximum at 90° and small maxima at 20° and 160°. The latter two maxima result because the first phenyl in the chain is able to orient almost parallel to the surface.

Thus, the density of the amine groups of the polymer chains influences the morphology of the assembly on the graphene sheet. However, the main purpose for introducing this group is its potential ability to form hydrogen bonds with the CO_2 molecules. In Figure V.9a we present the number of hydrogen bonds the polymer forms with carbon dioxide.

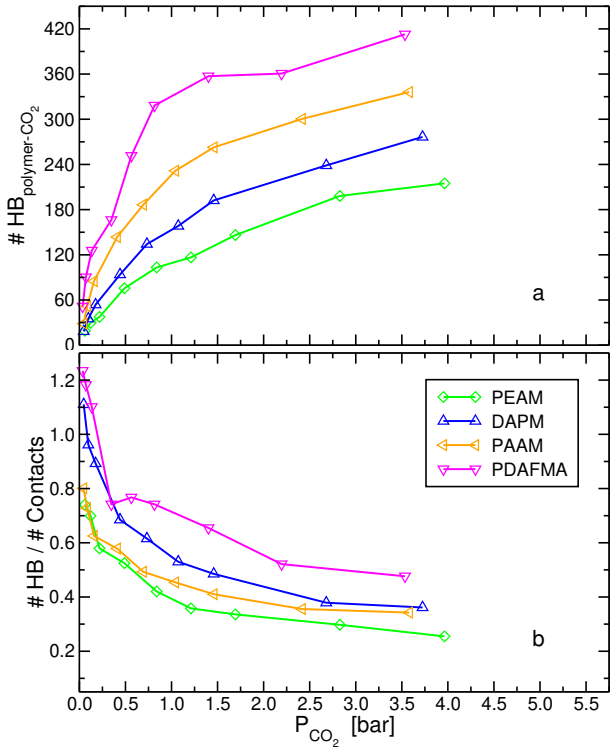

Figure V.9: The number of hydrogen bonds between the polymer and CO_2 molecules. (a) Absolute numbers, and (b) the ratio relative to the number adsorbed by the only-to-polymer mode, as a function of the partial pressure of CO_2.

The graph indicates that the larger the number of these hydrogen bonds the larger the capacity of the graphene-polymer composite systems to capture CO_2 gas as presented in Figure V.2. For the polymers considered in this study, larger number of amine groups resulted in more hydrogen bonds. Note that PAAM and PDAFMA contain also amides groups capable of donating and accepting hydrogen bonds as well. In fact, the contribution of these amide groups to the total number of hydrogen bonds formed between the polymer and the CO_2 molecules is significant (see Figure A III.25 in Appendix III). Thus, the amine and amide groups of the polymer can form intra-polymer hydrogen bonds affecting the polymer morphology as well as act as donors in the hydrogen bond formation with CO_2. Both augment the capture of CO_2 gas, the latter by direct interactions, whereas the former by aggregation, exposing areas of bare-graphene, that relative to the graphene-polymer models considered here exhibit the highest performance in adsorbing CO_2 gas. It is interesting that the amine groups substituted on a phenyl ring, e.g. PDAFMA and PAAM, have larger propensities to form hydrogen bonds with CO_2 than amine groups on a hydrocarbon chain, e.g. DAPM and PEAM. These amine groups are described by the same partial charges and Lennard-Jones parameters, thus, the reason for the different capacity in forming hydrogen bonds is probably because of larger dispersion interactions due to the aromatic ring. As expected, the curves in Figure V.9a show saturation behavior at higher pressures because of a decrease in available hydrogen bond donors. In Figure V.9b, we display the ratio of the number of hydrogen bonds to the number of CO_2 molecules adsorbed only to the polymer. This ratio is larger than one for G-PDAFMA and G-DAPM at low pressures because one CO_2 molecule can form two (or theoretically more) hydrogen bonds to the amine groups of the polymer. At these low partial pressures, it is evident that the adsorption to the polymer via a hydrogen bond(s) is

the predominant mechanism for all systems. As the partial pressure of CO_2 increases, the extent of adsorption by nonspecific dispersion interactions increases as well, again because of saturating the hydrogen donor sites. Figure V.10 displays three snapshots from the simulation of G-PDAFMA system depicting an adsorbed carbon dioxide molecule forming two, one, and zero hydrogen bonds. As mentioned in the Methods section, in all systems the carbon dioxide gas is

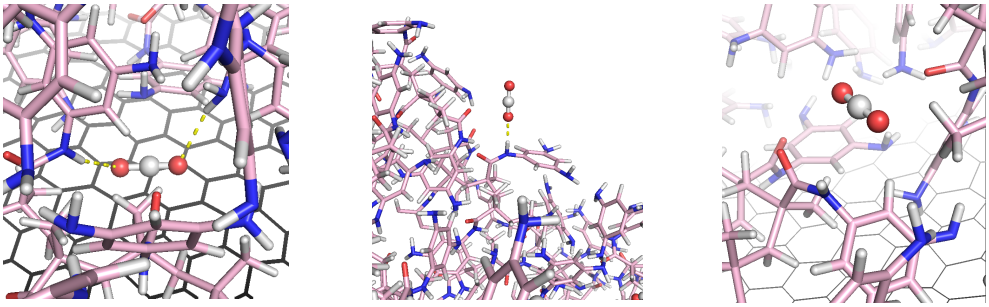

Figure V.10: Snapshots from the simulation of the G-PDAFMA composite system showing a CO_2 molecule in a ball and stick representation that is: (left) bound simultaneously to graphene and polymer and forms two hydrogen bonds, (middle) bound at the air/polymer interface and forms one hydrogen bond, (right) absorbed inside the polymer by nonspecific interactions (zero hydrogen bonds).

placed together with nitrogen (N_2) and methane (CH_4) gases, all with equal number of molecules. This is because optimized removal of CO_2 has to discriminate the binding to this gas with respect to binding other gases present in the air to be purified. Nitrogen is naturally present in the atmosphere in a large quantity and methane is one of the products of fuel combustion. Figure V.11 displays the percentage of the adsorbed molecules for these two gases as a function of the partial pressure of each gas.

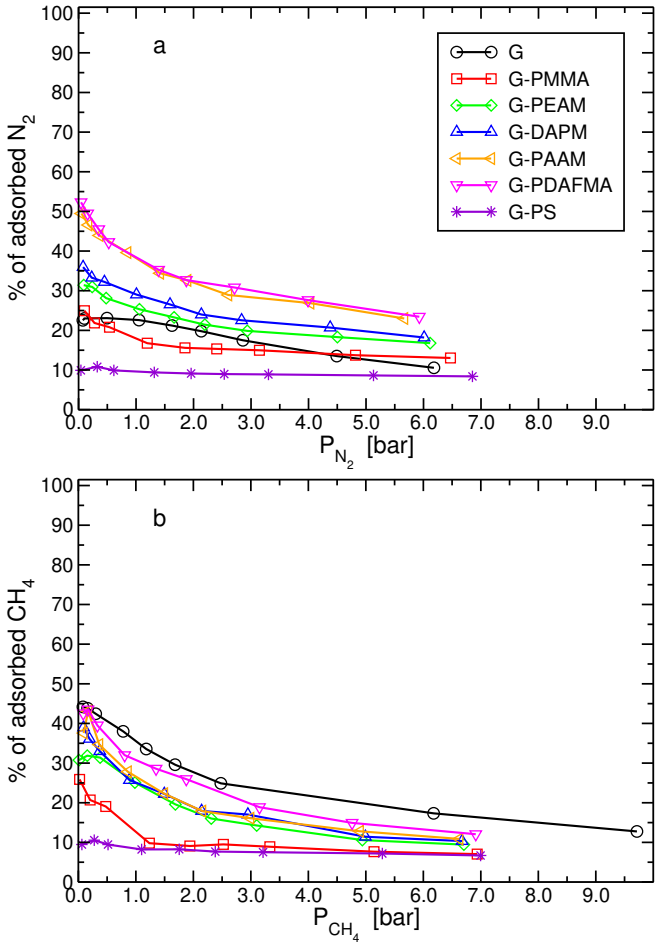

Figure V.11: The adsorption of the other two gases in the system. The figure displays the percentage of the number of gas molecules adsorbed at the graphene-polymer composite surface relative to the total number of these gas molecules in the system, plotted as a function of the partial pressure of the gas. (a) For nitrogen and (b) for methane.

In these cases the amounts of gases adsorbed are smaller than in the case for CO_2, ranging from 55% down to 15%. Again, the constant values exhibited by G-PS, and by G-PMMA above 1 bar, indicate the adsorbate molecules behave ideally and do not interact with one another. The decrease exhibited by the G-PMMA system up to around 1 bar is because at very low pressures the adsorption due to only-to-graphene mode saturates very quickly. This is because in this system the area of exposed graphene is very small. Once the binding sites on the exposed graphene are saturated, there is an onset of adsorption only to the polymer (a similar behavior occurs for the adsorption of CO_2 shown in Figure V.2b and explained by the changes of the different adsorption modes shown in Figure V.5). In Figure V.12 we calculate the selectivities of the adsorption.

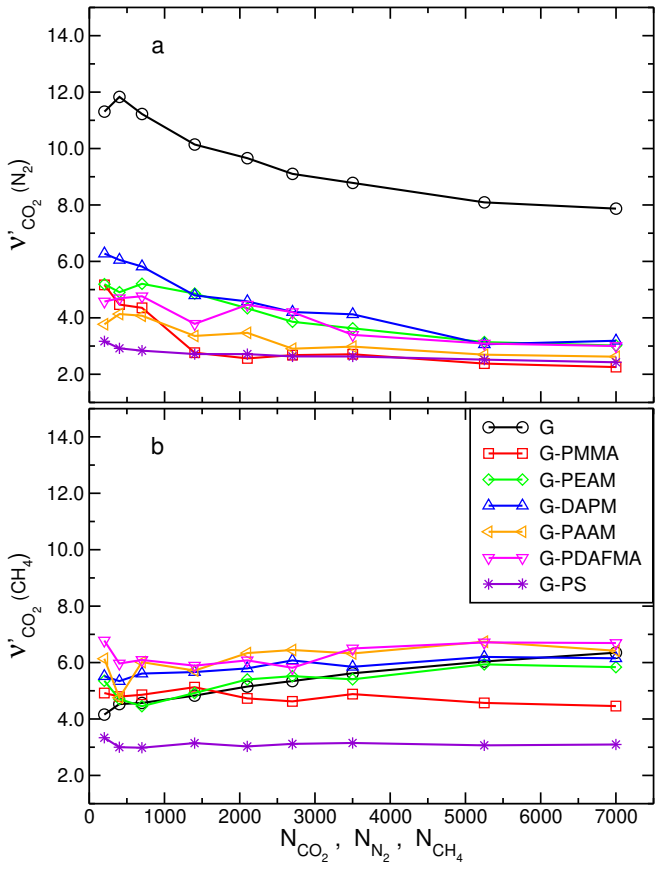

Figure V.12: The selectivity of the graphene-polymer composite surface to adsorb CO_2 relative to the adsorption of (a) nitrogen and (b) methane at 300 K. These selectivities are expressed as the ratio of the number of molecules of the two gases adsorbed at the interface divided by the corresponding ratio in bulk (see Equation V.1) and plotted against the number of molecules of each gas in the system (N_{CO_2}=N_{N_2}=N_{CH_4}).

We adopt the formalism of preferential binding [14] and plot the excess number of CO_2 molecules adsorb to the graphene-polymer composite, ν'_{CO_2}, by

$$\nu'_{CO_2}(x) = \frac{\theta_{CO_2}\ N_x}{\theta_x\ N_{CO_2}} \tag{V.1}$$

where θ_i is the number of molecules of gas i adsorbed to the composite. These numbers of adsorbed gas molecules are then divided by the corresponding numbers in bulk, N_i, to yield a measure of the excess ($\nu'_{CO_2} > 1$) or depleted ($\nu'_{CO_2} < 1$) number of adsorbed CO_2 molecules relative to a random distribution, i.e., relative to what is expected if there was no preference in binding of the two gases to the composite ($\nu'_{CO_2} = 1$). The results are shown in Figure V.12 with respect to (a) x=N_2 and (b) x=CH_4. For all graphene-polymer composites, CO_2 gas is adsorbed preferentially relative to nitrogen and methane. The curves are more or less constant as a function of the amount of gas in the system with values ranging from 2 to 7. This constant behavior is expected. If u_{GP-i} is the interaction energy between the composite and gas i, per gas molecule, and μ_i^0 is the standard chemical potential of gas i, then it can be shown [15] that,

$$\ln \nu'_{CO_2}(x) = \beta\left(\mu^0_{CO_2} - \mu^0_x\right) \ln \frac{\mathcal{Z}'_{CO_2,ads}}{\mathcal{Z}'_{x,ads}} + \beta\left(u_{GP-CO_2} - u_{GP-x}\right) \tag{V.2}$$

where $\mathcal{Z}'_{i,ads}$ is the single-site molecular partition function, summed over internal energies, of adsorbate i, and β is $1/k_BT$. Thus, the preferential adsorption of CO_2 is independent of N^o_{gas}.

Nevertheless, there are some deviations from a constant behavior, especially for the bare-graphene system. Although, we did not evaluate the first term on the right-hand side of Equation V.2, we attributed these deviations for

the breakdown of the non-interacting adsorbing-sites approximation on bare-graphene [16]. In fact, as the pressure increases, there are increasing interactions between the adsorbate molecules which ultimately form clusters. Figure V.13 displays the probability distribution of forming clusters of different sizes for the three gases.

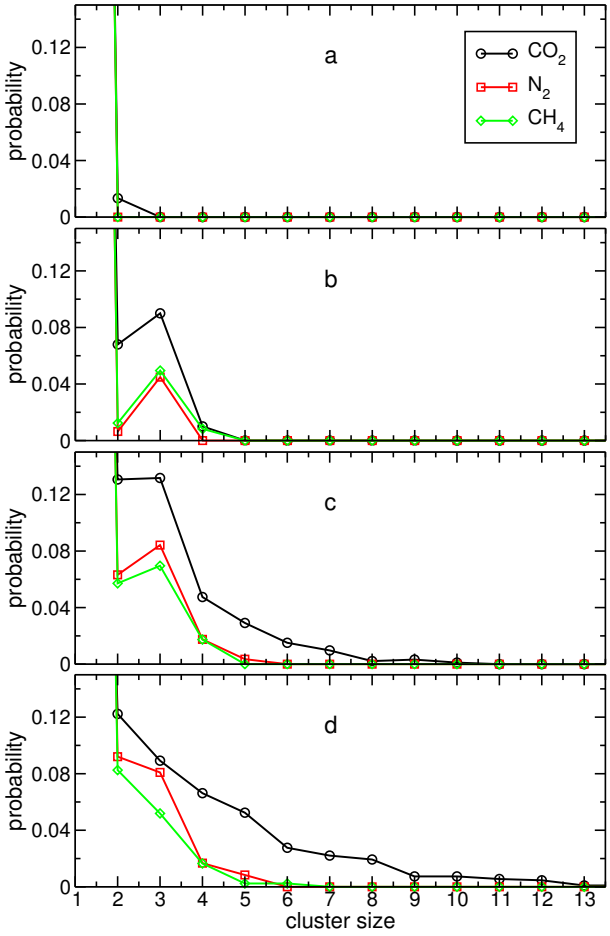

Figure V.13: Normalized distributions of the size of clusters formed by gas molecules adsorbed on graphene (for the simulations with bare-graphene) at four different bulk gas densities, spanning the whole range of pressures. More specifically, the analysis was performed for the simulations with (a) 200, (b) 1400, (c) 3500, and (d) 7000, molecules of each gas (see Tables A III.14–A III.16 in Appendix III). Two molecules are considered bound to each other if their distance between their centers of mass is smaller than 0.5 nm (which is around the first minimum in the corresponding radial distribution functions). Note that at low densities, the majority of the molecules do not form clusters (cluster-size=1).

CO_2 has the highest probabilities to form clusters and it also forms clusters with sizes much larger than N_2 and CH_4. A snapshot representing this behavior of carbon dioxide on bare-graphene for the system with the densest gas is shown in Figure V.14. We argue, that the reason adsorbed CO_2 molecules

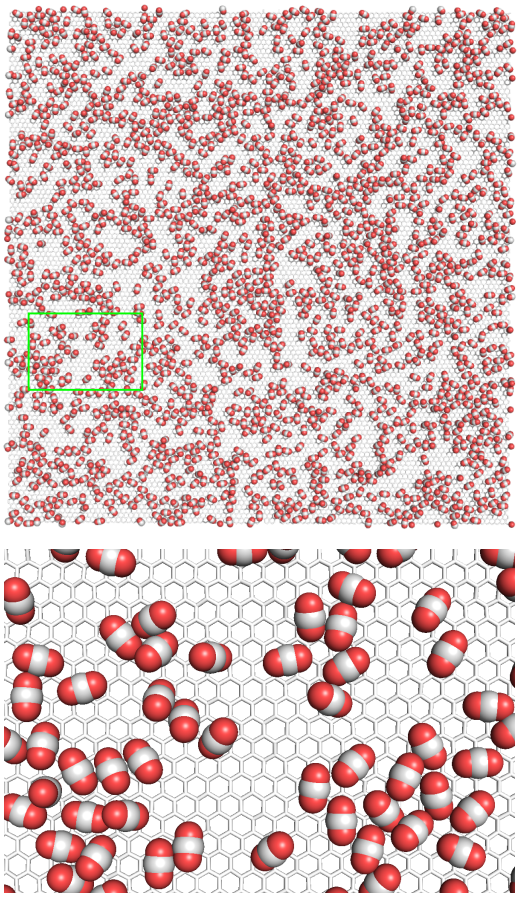

Figure V.14: Upper panel: a snapshot of the arrangement of CO_2 molecules adsorbed on one of the graphene sheets for the simulation of bare-graphene at the highest partial pressure of CO_2 (7000 gas molecules). Lower panel: magnification of the green boxed-area above. For clarity, nitrogen and methane molecules are now shown.

display extensive clustering relative to the other two gases is because they are characterized by a large quadrupole moment and with a proper arrangement on a two-dimensional surface, they can interact favorably with one another via electrostatic interactions. Note that the electric quadrupole moment for methane is zero and for nitrogen is about a third of that of carbon dioxide [17].

Figure V.12 indicates that the preferential adsorption of CO_2 relative to N_2 is much larger than that relative to CH_4. We calculated u_{GP-i} by energy minimizing a single gas molecule on the graphene sheet and found it to be, 25.1, 13.3, and 16.5 kJ/mol for i=CO_2, N_2, and CH_4, respectively. Thus qualitatively, the preferential adsorption correlate with the binding energies. We can then calculate the undetermined term $\beta\left(\mu^0_{CO_2} - \mu^0_x\right) \ln \frac{\mathcal{Z}'_{CO_2,ads}}{\mathcal{Z}'_{x,ads}}$ in Equation V.2 and obtain -2.3 and -2.0 for the relations involving N_2, and CH_4, which are very similar values. Thus for these gases on bare-graphene, the changes in preferential adsorption is predominantly determined by the different binding energies. For the systems with the polymers, the binding energies and the molecular partition functions of the adsorbed gas need to be calculated for each adsorption mode (Figure V.5) separately, thereby, impeding easy evaluation of the preferential adsorption.

V.4 Conclusions

Three-dimensional porous material made by self-assembly of graphene sheet can be a very good adsorbent for the capture of CO_2. However, improved mechanical properties of this porous structure require the presence of polymer latex generating a graphene-polymer composite material. In this Chapter we investigated several polymers to generate such composite systems that maximize the capacity to adsorb CO_2 molecules. Furthermore, the ability of the composite materials to discriminate against the binding of potentially competing gases, N_2 and CH_4, is examined as well. We address these questions by all-atom molecular dynamic simulations in the canonical ensemble. In this case, the composite material is in direct equilibrium with the gas mixture which consist of equal number of CO_2, N_2 and CH_4 molecules. Obviously, a strong binding energy between the polymer and CO_2 will favor the adsorption. For this reason, we consider the incorporation of a protic groups into the polymer such as amines and amides. In addition, a benzene ring can interact favorably with CO_2 due to dispersion interactions and therefore its incorporation into the proposed polymers was tested as well. The performance of the graphene-polymer systems was compared with those of bare-graphene which actually exhibited the best capacity to adsorb CO_2 molecules. Nevertheless, the graphene-polymer system that performed the best was only slightly below that of bare-graphene.

Despite the fact that for all systems, the ratio between the mass of the polymer to that of the graphene sheet was constant, the different polymers considered adsorbed onto the graphene sheet with different morphologies. The main factor determining the assembled structure was the number of protic groups of the polymer. The larger the number of these groups, the stronger the cohesive forces (due to intra-polymer hydrogen bonds) and the stronger the aggregation.

As a consequence, there is a partial exposure of graphene on which the gas can adsorb. Such behavior of the graphene-polymer system induce three type of adsorption modes, whose relative populations depend on the properties of the polymer.

We find that the aprotic polymers captured the lowest amount of CO_2. This is because these polymers 'wet' very well the surface of graphene and their dispersion interaction with CO_2 is relatively weak. Contrarily, composites with protic polymers perform better and the adsorption of CO_2 increases with the number of protic groups in the polymer. The contribution of hydrogen bond interactions to the binding of CO_2 to the polymer is very high at low pressures and decreases with increasing the gas pressure while nonspecific interactions become increasingly more abundant. For all the systems considered in the simulation, CO_2 bind to the adsorbent in excess relative to N_2 and CH_4. Above a critical gas pressure in the bare-graphene system, the adsorption of CO_2 involved formation of clusters whose size and population are increased with the pressure.

References

[1] Luzar, A.; Chandler, D. Structure and hydrogen bond dynamics of water-dimethyl sulfoxide mixtures by computer simulations, *J. Chem. Phys.* 1993, *98*, 8160–8173.

[2] Hess, B.; Kutzner, C.; Van Der Spoel, D.; Lindahl, E. Gromacs 4: algorithms for highly efficient, load-balanced, and scalable molecular simulation, *J. Chem. Theory Comput.* 2008, *4*, 435–447.

[3] Bussi, G.; Donadio, D.; Parrinello, M. Canonical Sampling through Velocity Rescaling, *J. Chem. Phys.* 2007, *126*, 014101.

[4] Potoff, J. J.; Siepmann, J. I. Vapor-liquid equilibria of mixtures containing alkanes, carbon dioxide, and nitrogen, *AIChE J.* 2001, *47*, 1676–1682.

[5] Yang, J.; Ren, Y.; Tian, A.-m.; Sun, H. COMPASS Force Field for 14 Inorganic Molecules, He, Ne, Ar, Kr, Xe, H_2, O_2, N_2, NO, CO, CO_2, NO_2, CS_2, and SO_2, in Liquid Phases, *J. Phys. Chem. B* 2000, *104*, 4951–4957.

[6] Harris, J. G.; Yung, K. H. Carbon Dioxide's Liquid-Vapor Coexistence Curve And Critical Properties as Predicted by a Simple Molecular Model, *J. Phys. Chem.* 1995, *99*, 12021–12024.

[7] Murthy, C.; Singer, K.; Klein, M.; McDonald, I. Pairwise Additive Effective Potentials for Nitrogen, *Mol. Phys.* 1980, *41*, 1387–1399.

[8] Atkins, P. W.; de Paula, J. *Physical Chemistry;* Oxford University Press: Oxford, UK, seventh edition ed., 2002.

[9] Jorgensen, W. L.; Maxwell, D. S.; Tirado-Rives, J. Development and testing of the opls all-atom force field on conformational energetics and properties of organic liquids, *J. Am. Chem. Soc.* 1996, *118*(45), 11225–11236.

[10] Zangi, R.; Roccatano, D. Strings-to-Rings Transition and Antiparallel Dipole Alignment in Two-Dimensional Methanols, *Nano Lett.* 2016, *16*, 3142–3147.

[11] Walther, J. H.; Jaffe, R.; Halicioglu, T.; Koumoutsakos, P. Carbon Nanotubes in Water: Structural Characteristics and Energetics, *J. Phys. Chem. B* 2001, *105*, 9980–9987.

[12] Meconi, G. M.; Ballard, N.; Asua, J. M.; Zangi, R. Adsorption and Desorption Behavior of Ionic and Nonionic Surfactants on Polymer Surfaces, *Soft Matter* 2016, *12*, 9692–9704.

[13] Meconi, G. M.; Ballard, N.; Asua, J. M.; Zangi, R. Shedding light on the different behavior of ionic and nonionic surfactants in emulsion polymerization: from atomistic simulations to experimental observations, *Phys. Chem. Chem. Phys.* 2017, *19*, 31692–31705.

[14] Tanford, C. Extension of the theory of linked functions to incorporate the effects of protein hydration, *J. Mol. Biol.* 1969, *39*, 539–544.

[15] Zangi, R.; Zhou, R.; Berne, B. J. Urea's Action on Hydrophobic Interactions, *J. Am. Chem. Soc.* 2009, *131*, 1535–1541.

[16] Bae, J. H.; Lim, Y. R.; Sung, J. Statistical Mechanics of Molecular Adsorption: Effects of Adsorbate Interaction on Isotherms, *Langmuir* 2008, *24*, 2569–2572.

[17] Graham, C.; Pierrus, J.; Raab, R. Measurement of the electric quadrupole moments of CO_2, CO and N_2, *Mol. Phys.* 1989, *67*, 939–955.

Chapter VI

Conclusions

In this thesis, we aimed at elucidating different aspects of adsorption phenomena in emulsion polymerization and gas separation processes by performing atomistic Molecular Dynamics simulations. The use of computational studies was particularly useful in that they provided an insight into fundamental behavior at the molecular level which is not possible experimentally.

As described in the Introduction, surfactants play a vital role in emulsion polymerization, which serve both to nucleate particles and also to prevent the coagulation of the latex during synthesis and storage. However, in many applications the use of ionic and nonionic surfactants is poorly understood, causing significant problems. In fact, the difference in the behavior of ionic surfactants compared with that of nonionic surfactants, as encountered in the process of emulsion polymerization, is where our interest arised.

In **Chapter III**, we combined experimental and computational studies aiming to elucidate the adsorption properties of ionic and nonionic surfactant at hydrophobic polymer surface such as poly(styrene). To represent these two types of surfactants, we choose sodium dodecyl sulfate and poly(ethylene glycol)–poly(ethylene) block copolymers, both commonly utilized in emulsion polymerization. By applying quartz crystal microbalance with dissipation monitoring we find that the non-ionic surfactants are desorbed from the poly(styrene) surface slower, and at low surfactant concentrations they adsorb with stronger energy, than the ionic surfactants. If fact, from molecular dynamics simulations we obtain that the effective attractive force of these nonionic surfactants to the surface increases with the decrease of their concentration, whereas, the ionic surfactant exhibits mildly the opposite trend. We argue that the difference in this contrasting behavior stems from the physio-chemical properties of the head group. Ionic surfactants characterized by small and strongly hydrophilic head groups form an ordered self-assembled structure at the interface whereas,

non-ionic surfactants with large and weakly hydrophilic head groups generate a disordered layer. Consequently, upon an increase in concentration, the layer formed by the nonionic surfactants prevents the aprotic poly(ethylene glycol) head groups to satisfy all their hydrogen bonds capabilities. As a response, water molecules intrude this surfactant layer and partially compensate for the missing interactions, however, at the expense of their ability to form hydrogen bonds as in bulk. This loss of hydrogen bonds, either of the head groups or of the intruding water molecules, is the reason the nonionic surfactants weaken their effective attraction to the interface with the increase in concentration.

For the ionic surfactant we have not observed this behavior; however, further analyzes were hampered by the large fluctuations in the electrostatic forces which compensate each other and lead to large variations in the energy.

Nevertheless, further research is incited to understand the thermodynamic results of adsorption for ionic surfactants better. By the use of other methods for free energy calculations (such as metadynamics [1, 2] sampling calculations), it may be possible to determine the free-energies of binding states, defined by the ion coordination to surfactants and water molecules at different concentrations of ionic active agents at the polymer surface. The result can help us to explain the drastic changes of the electrostatic interactions for the SDS systems.

Since the particle nucleation behavior of nonionic surfactants shows deviations from the fundamental kinetic theory, in **Chapter IV** we performed experimental measurement of emulsion polymerization of styrene together with MD simulations to clarify the behavior of surfactants at monomer/polymer-water interface. In a batch emulsion polymerization of styrene, the nonionic surfactant Disponil AFX 1080 leads to two nucleation periods, in contrast to the behavior observed for the ionic surfactant SDS.

This can be explained by the absorption of the nonionic surfactant into the

organic phase at the early stages of the polymerization reaction which is then released as the reaction progresses. Indeed, we found that the partition coefficient of the surfactant between the organic phase and water increases with the amount of monomer in the former, and preferential partitioning is detected to organic phases containing at least 55% styrene.

The simulations results presented in this thesis confirmed that spontaneous dissolution of the non-ionic surfactant into a styrene-rich organic phase occurs above a critical concentration of the surfactant adsorbed at the interface. Above this critical concentration, a linear correlation between the amount of surfactant adsorbed at the interface and that absorbed inside the organic phase is observed. To facilitate this absorption into a completely hydrophobic medium, water molecules accompany the intruding surfactants.

Similar simulations but with the ionic surfactant instead did not result in any absorption of the surfactant into a neat styrene phase, likely because of its strongly hydrophilic head group.

The unusual partitioning behavior of nonionic surfactants explains a number of observable features of emulsion polymerization reactions which use nonionic surfactants and should help with future development of processes for improved control over polymerization.

A continued increase in energy demand and the urgency in reducing CO_2 emission require rapid development of alternative and clean energy technologies. Efficient ways of storing and capturing CO_2 are key challenges in the development of carbon capture systems. Among the different methods, gas sorption and storage by physical adsorption in porous media is considered a promising approach due to the high accessible surface area and pore structure of the material. Many efforts have been made to synthetize a wide variety of tailor-made porous ma-

terials, such as zeolites, carbons, polymers, metal–organic frameworks(MOFs), and covalent organic frameworks (COFs) as adsorbents for carbon capture and separation from the flue gas.

Three-dimensional graphene-polymer porous materials have been proposed recently as potential adsorbents for carbon dioxide capture. Owing to their mechanical stability and ease of regeneration they can potentially alleviate shortcomings encountered by other sorbents.

In **Chapter V**, we report results from molecular dynamics simulations on the adsorption of CO_2 gas molecules by these graphene-polymer composite systems. The performance of each composite as a function of the gas pressure is quantified, and analyzed relative to the adsorption of nitrogen and methane which are also present, in equal amounts, in the simulation gas mixture.

Six types of polymers adsorbed on graphene surfaces, with a constant polymer-to-graphene mass-ratio of 1.02, were tested and compared to results obtained from a bare-graphene sheet. In particular we examined the abilities of hydrogen-bond donor groups, amines and amides, as well as aromatic rings to promote and discriminate CO_2 capture.

We find that bare-graphene displays the highest capacity to adsorb CO_2. Nevertheless, increasing the number of amine/amide protic groups of the polymer augments the adsorption. In fact, the best performing polymer in our study, which contains three protic groups per monomer, exhibits capture of CO_2 almost as good as bare-graphene. Incorporation of aromatic rings into the polymers did not improve the performance. However, when the amines were attached to phenyl groups instead of alkanes, larger CO_2 adsorptions were observed.

Furthermore, these protic polymers form substantial intra-polymer hydrogen bonds and consequently exhibit cohesive behavior. In these cases, the aggregation of the polymer resulted in partial exposure of the graphene sheet on which

the gas molecules can adsorb as well. Thus, the enhanced CO_2 adsorption of the protic polymers composite systems is due to the direct interactions of the protic groups with the gas as well as the ability to adsorb on the exposed segments of graphene.

In contrast aprotic polymers, such as poly(styrene) or poly(methyl methacrylate), extensively spread on graphene and are characterized by small capacities to adsorb CO_2.

For all system studied, CO_2 is adsorbed preferentially relative to N_2 and CH_4. This preferential adsorption is almost constant as a function of the gas pressure with values ranging from 2 to 12.

The results emerged from the analysis of the adsorption of CO_2 by the graphene-polymer composites investigated may be useful for the design and synthesis of novel composite materials with a better sorption capacity relative to the bare graphene. The presence of numerous protic groups and the chemical structure of the polymer are important features to take in account for the developing of the new composites because determining the self-organization of the polymer at the graphene sheets and consequently the capture ability of the final composite material. The graphene oxide (GO) is an oxidized form of graphene, showing a high density of oxygen functional groups (carboxyl, hydroxyl, carbonyl, and epoxy) in the carbon lattice. Since the presence of these functional groups and its lower production cost by chemical oxidation of graphite to graphite oxide, GO is considered a promising option for carbon dioxide capture. Therefore a further investigation is encouraged for the modeling of new GO-polymer composites with an improved CO_2 uptake.

List of pubblications and conference presentations

One part of this thesis has been published, another is planned to be published. Additionally, parts of the work described in the thesis have been presented at conferences or in a summer school both as oral or poster presentation. Here, a list of (planned) publications is presented as well as an overview of the oral and poster presentations that were given regarding the thesis.

Publications

"Adsorption and Desorption Behavior of Ionic and Nonionic Surfactants on Polymer Surfaces" by Giulia Magi Meconi, Nicholas Ballard, José M. Asua and Ronen Zangi. *Soft Matter* **2016**, 12, 9692-9704.

"Shedding Light on the Different Behavior of Ionic and Nonionic Surfactants in Emulsion Polymerization: From Atomistic Simulations to Experimental Observations" by Giulia Magi Meconi, Nicholas Ballard, José M. Asua and Ronen Zangi. *Phys. Chem. Chem. Phys.* **2017**, 00, 1-14.

"Adsorption of CO_2 Gas on Graphene-Polymer Composites" by Giulia Magi Meconi, Radmila Tomovska and Ronen Zangi. Manuscript submitted.

Oral presentations

"Adsorption and Desorption Behavior of Ionic and Nonionic Surfactants on Polymer Surfaces" by Giulia Magi Meconi, Nicholas Ballard, José M. Asua and Ronen Zangi. Frontiers in Water Biophysics (FWB2017) Conference. Erice, Italy, 2017.

"Adsorption and Desorption Behavior of Ionic and Nonionic Surfactants on Polymer Surfaces" by Giulia Magi Meconi, Nicholas Ballard, José M. Asua and Ronen Zangi. 16^{th} European Student Colloid Conference (ESC2017). Florence, Italy, 2017.

Poster presentations

"Adsorption and Desorption Behavior of Ionic and Nonionic Surfactants on Polymer Surfaces" by Giulia Magi Meconi, Nicholas Ballard, José M. Asua and Ronen Zangi. Dynapeutics Summer School. San Sebastián, Spain, 2016.

Resumen y conclusiones

El principal objetivo de este trabajo de investigación, es el estudio de diferentes aspectos que tienen lugar en los fenómenos de adsorción, en los procesos de polimerización en emulsión y de separación de gases. Como herramienta fundamental para conseguir este objetivo, se empleó la dinámica molecular atomística. Estos estudios computacionales, fueron particularmente útiles ya que proporcionaron una visión del comportamiento fundamental a nivel molecular, diferente al punto de vista experimental, pudiendo estudiar y observar comportamientos que son difíciles de explicar experimentalmente.

En la introducción de esta tesis, se describe como los surfactantes desempeñan un papel crucial en la polimerización por emulsiones. Éstos están implicados tanto en procesos de nucleación de las partículas, como en la prevención de los fenómenos de coagulación del látex durante la síntesis y el almacenamiento. A pesar de las múltiples aplicaciónes de los surfactantes, tanto iónicos y no iónicos, se conoce poco acerca de su verdadero funcionamiento en estos procesos. Este hecho, y en particular, la diferencia en el comportamiento de los tensioactivos iónicos en comparación con la de los tensioactivos no iónicos en el proceso de polimerización en emulsión, es donde hemos centrado el foco de atención de nuestro trabajo de investigación.

En el **Capítulo III**, combinamos estudios experimentales y computacionales con el objetivo de contrastar las propiedades de adsorción del surfactante iónico y no iónico en la superficie de polímero hidrofóbico, como el poli(estireno), obtenidas mediantes métodos experimentales y teóricos. Como modelo de estos dos tipos de surfactantes, elegimos dodecilsulfato de sodio y copolimeros

de poli(etilenglicol)–poli(etileno) ambos comúnmente utilizados en la polimerización en emulsión. Al estudiar estos compuestos mediante diferentes técnicas analíticas como puede ser la microbalanza de cristal de cuarzo (QCM) con monitoreo de disipación, la cual mide la masa mediante los cambios de frecuencia de un cristal de cuarzo piezoeléctrico y es capaz determinar masas muy pequeñas; encontramos que los surfactantes no iónicos, en comparación con los iónicos, se desorben de la superficie de poli(estireno) más lentamente a concentraciones elevadas. A baja concentración se adsorben con mayor fuerza los surfactantes no iónicos frente a los iónicos. Por otro lado a partir de simulaciones de dinámica molecular, hemos sido capaces de determinar que la fuerza de atracción efectiva de estos surfactantes no iónicos en la superficie tiende a aumentar con la disminución de su concentración, mientras que el surfactante iónico presenta una tendencia opuesta. La explicación a este comportamiento, podría encontrarse en las propiedades fisicoquímicas del grupo hidrofílico. Los surfactantes iónicos caracterizados de un tamaño de grupo hidrofílico más pequeño, que resultan ser fuertemente hidrófilas, forman una estructura autoensamblada ordenada en la interfase, mientras que, los surfactantes no iónicos con grupos hidrofílicos grandes, pero débilmente hidrófilas, generan también una capa autoensanblada pero desordenada. En consecuencia, al aumentar la concentración de tensioactivos o surfactantes no iónicos, la capa formada por éstos, impide que las cabezas de poli(etilenglicol) apróticas, formen puentes de hidrógeno con facilidad. Como consecuencia a este comportamiento, las moléculas de agua invaden esta capa de surfactante, dando lugar a nuevas interacciones de hidrogeno que sustituyente a las que se formaría con el surfactante. Sin embargo, a expensas de su capacidad para formar enlaces de hidrógeno como en el bulk . La disminución en la formación de puentes o interacciones de hidrógeno, ya sea debido a los grupos principales o de las moléculas de agua que se intercalan

entre el surfactante y la superficie del polímero, es la razón por la cual los tensioactivos o surfactantes no iónicos pierden su capacidad de atracción efectiva a la interfase con el aumento de la concentración. Para el surfactante iónico no hemos observado este comportamiento; sin embargo, las grandes fluctuaciones en las fuerzas electrostáticas generadas en el medio y que tienden a compensarse, conducen a grandes variaciones en la energía, lo cual deriva en dificultades para la realización de diferentes análisis. No obstante, este hecho, nos invita a investigar más para alcanzar una mayor comprensión de los resultados termodinámicos de la adsorción de surfactantes iónicos. Mediante el uso de otros métodos (como por ejemplo metadinámicos [1, 2] cálculos de muestreo) para cálculos de energía libre, es posible determinar las energías libres de los estados de unión, definidas por la coordinación iónica con surfactantes y moléculas de agua en diferentes concentraciones de agentes activos iónicos, en la superficie del polímero. El resultado puede ayudarnos a entender los cambios drásticos de las interacciones electrostáticas para los sistemas SDS.

Dado que el comportamiento de nucleación de partículas de los surfactantes no iónicos muestra desviaciones de la teoría cinética fundamental, en el **Capítulo IV** realizamos una medición experimental de la polimerización en emulsión de estireno junto con simulaciones de MD para aclarar y explicar, el comportamiento de los surfactantes en la interfase generada entre monómero/polímero-agua. En una polimerización de estireno en emulsión por lotes de estireno, el agente tensioactivo no iónico Disponil AFX 1080 conduce a dos períodos diferentes de nucleación. El comportamiento opuesto se ha observado cuando se hace uso del agente tensioactivo iónico SDS. Esto se puede explicar por la absorción del surfactante no iónico en la fase orgánica en las primeras etapas de la reacción de polimerización, liberándose progresivamente a medida que tiene lugar la reacción. De hecho, se pudo determinar que el valor del coeficiente de

reparto del surfactante entre la fase orgánica y acuosa, aumenta con la cantidad de monómero en el primero, y la partición preferencial se detecta a las fases orgánicas que contienen al menos 55% de estireno. Los resultados de las simulaciones realizadas confirmaron que la disolución espontánea del surfactante no iónico en una fase orgánica rica en estireno ocurre por encima de una concentración crítica del surfactante adsorbido en la interfase. Por encima de esta concentración crítica, se observa una correlación lineal entre la cantidad de coadyuvante adsorbido en la interfase y la absorbida en la fase orgánica. Para facilitar esta absorción en un medio completamente hidrófobo, las moléculas de agua acompañan a los surfactantes que entran en la fase orgánica. Las simulaciones realizadas para el surfactante iónico, no dieron como resultado ninguna absorción del surfactante en una fase de estireno puro, probablemente debido al fuerte carácter hidrofílico de componente hidrofílico. El comportamiento inusual de partición de los surfactantes no iónicos son útiles para explicar una serie de aspectos que se pueden encontrar cuando se realizan reacciones de polimerización en emulsión y además debería ayudar al desarrollo futuro de procesos que tengan como objetivo final, el control total sobre la polimerización.

El continuo aumento de la demanda de energía por parte de la población mundial y la urgencia de reducir la emisión de CO_2, requieren un rápido desarrollo de tecnologías de energía alternativa y limpia. Las formas eficientes de almacenar y capturar CH_4 son desafíos clave en el desarrollo de sistemas de captura de carbono. Entre los diferentes métodos desarrollados hasta la fecha, la absorción y el almacenamiento de gases por adsorción física en medios porosos se considera un campo de investigación prometedor debido a la alta área de superficie accesible y a la estructura de poros que posee el material. En las últimas décadas se e han realizado muchos estudios cuya principal finalidad consistió en sintetizar una amplia variedad de materiales porosos hechos a medida, como pueden ser

zeolitas, polímeros, MOF (de sus siglas en inglés Metallic organic Framework) y COF, (de sus siglas en inglés, Covalent Organic Framework) como adsorbentes para la captura y separación de carbono proveniente de los gases de combustión. Actualmente, los materiales poliméricos porosos, sintetizados a partir de grafeno tridimensional, son los mejores candidatos como posibles adsorbentes para la captura de dióxido de carbono. Su estabilidad mecánica y facilidad de regeneración, les sitúan en una posición ventajosa frente a otros sorbentes que posee otra seríe de deficiencias.

Debido a este creciente interés en los sistemas preparados a partir de grafeno, en el **Capítulo V**, presentamos los resultados obtenidos de simulaciones de dinámica molecular, consistentes en medir la adsorción de moléculas de gas CO_2 sobre estos sistemas compuestos de grafeno-polímero. El rendimiento de cada compuesto en función de la presión del gas se cuantifica y se analiza en relación con la adsorción de nitrógeno y metano que también están presentes, en cantidades iguales, en la mezcla de gases de simulación. Se probaron seis tipos de polímeros adsorbidos sobre grafeno, con una relación de masa constante de polímero a grafeno de 1.02, y se compararon con los resultados obtenidos de una lámina de grafenosin modificar. En particular, se estudiaron las capacidades de los grupos capaces de generar enlaces de hidrógeno, como, aminas y amidas, así como los anillos aromáticos para promover y discriminar la captura de CO_2. Del análisis de los resultados, podemos deducir que el grafeno sin modificar, muestra una gran capacidad de adsorción de CO_2 per se. Cuanto el grafeno está combinado con polímeros que contienen un elevado número de grupos próticos, como pueden ser amina/amida, la adsorción aumenta considerablemente. El polímero que mostró un mejor rendimiento en nuestro estudio contiene tres grupos próticos por monómero y muestra una captura de CO_2 al menos similar a la del grafeno sin modificar. La incorporación de anillos aromáticos no

mejoró el rendimiento de CO_2 capaturado. Sin embargo, cuando en el estudio se introdujeron derivados de benceno funcionalizados con grupos amina, se observaron adsorciones más elevadas de CO_2. Además, estos polímeros próticos, son capaces de dar lugar a interacciones de hidrógeno dentro del polímero y, dando lugar a un comportamiento cohesivo. En estos casos, la agregación del polímero resultó en una exposición parcial de la hoja de grafeno en la cual las moléculas de gas también pueden adsorber. Por lo tanto, la mayor adsorción de CO_2 de los sistemas compuestos de polímeros próticos se debe a las interacciones directas de los grupos próticos con el gas, así como a la capacidad de adsorción de las áreas libres de grapheno expuestas al gas. En contraste, los polímeros apróticos, como el poli(estireno) o el poli(metacrilato de metilo), se extienden ampliamente sobre el grafeno y se caracterizan por pequeñas capacidades para adsorber el CO_2. Para todos los sistemas estudiados, el CO_2 se adsorbe preferentemente en relación con N_2 y CH_4. Esta adsorción preferencial es casi constante en función de la presión del gas con valores comprendidos entre 2 y 12. Los resultados obtenidos del análisis de la adsorción de CO_2 por los compuestos de grafeno-polímero investigados, pueden ser útiles para el diseño y la síntesis de nuevos materiales con una mejor capacidad de adsorción en relación con el grafeno sin modificar. La presencia de numerosos grupos próticos y la estructura química del polímero son características importantes a tener en cuenta para el desarrollo de los nuevos compuestos, ya que determinan la auto organización del polímero sobre las laminas de grafeno y, en consecuencia, la capacidad de captura del material final. El óxido de grafeno (GO) es una forma oxidada de grafeno, que muestra una alta densidad de grupos funcionales de oxígeno (carboxilo, hidroxilo, carbonilo y epoxi) en la red de carbono. Debido a la presencia de estos grupos funcionales y su menor costo de producción por la oxidación química del grafito al óxido de grafito, GO se considera una opción

prometedora para la captura de dióxido de carbono. Por lo tanto, se recomienda una investigación adicional para el modelado de nuevos compuestos de polímero GO con una mejor absorción de CO_2.

References

[1] Laio, A.; VandeVondele, J.; Rothlisberger, U. A Hamiltonian electrostatic coupling scheme for hybrid Car-Parrinello molecular dynamics simulations, *J. Chem. Phys.* 2002, *116*, 6941–6947.

[2] Barducci, A.; Bonomi, M.; Parrinello, M. Metadynamics, *Wiley Interdiscip. Rev. Comput. Mol. Sci.* 2011, *1*(5), 826–843.

Appendices

Appendix I

Supplementary Information Chapter III

Table A I.1: Details of the simulation setups for the three surfactants studied. For each surfactant we considered four concentrations reported as two-dimensional densities, ρ_{2D}. The molecule, 16-mer PS, composing the surface is defined in Fig. A II.14. The average length of the simulation box along each axis is also shown.

	# Surfactants	ρ_{2D} [mg/m^2]	# 16-mer PS	# Waters	$\langle X \rangle / \langle Y \rangle$ [nm]	$\langle Z \rangle$ [nm]
SDS	1 / 12 / 24 / 48	0.0365 – 1.71	20	2853 – 2973	3.62 – 3.67	10.71 – 12.11
7PEO4PE	1 / 8 / 12 / 24	0.0551 – 1.34	20	3491 – 6560	3.58 – 3.64	12.10 – 20.07
10PEO6PE	1 / 8 / 12 / 24	0.0545 – 1.38	22	3949 – 11417	4.25 – 4.37	9.37 – 22.05

A Model for Poly(styrene)

A PS chain is modeled as a 16-mer unit. Because the stereochemistry of each unit is randomly generated during polymerization, we chose to model each chain with alternating C_α chiral centers (R followed by S). The bonded and non-bonded parameters of PS were taken from the OPLS-AA model of ethylbenzene. [1, 2] However, in order to allow the connectivity between the subunits and simultaneously maintain zero charge for each of these subunits, we made the following changes. The partial charge of C_β of the first residue was changed from -0.180 to -0.120, that of C_γ of the last residue was changed from -0.115 to -0.055, and both changes were applied to the repeating residues. The resulting model is shown in Fig. A II.14 and the non-bonded interactions are specified in Table A II.9. Using this model, we obtained a value of 1.02 kg/m^3 for the density of amorphous PS which is close to its experimental value [3] of 1.04–1.06 kg/m^3. Furthermore, the calculated values of the radius of gyration, 9.8 Å, and the weight-normalized end-to-end distance squared, 0.42 Å$^2\cdot$ mol/g, are also in a very good agreement with their experimentally determined values of 10.0 Å and 0.43 Å$^2\cdot$ mol/g, respectively, as well as with other models for PS. [4–6]

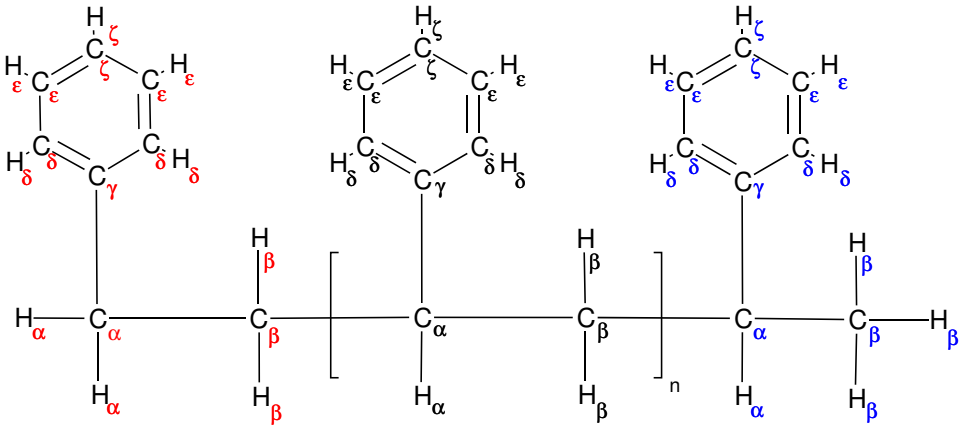

Figure A I.1: The model for poly(styrene) based on the OPLS-AA force-field. The partial charge and LJ parameters describing each atom is detailed in Table A II.9. Note that the C_α of the repeating and last residues are chirals, nevertheless, the parameters for the R and S configurations are the same.

Table A I.2: Partial charges and LJ parameters for the poly(styrene) model. The values refer to all residue types (first, repeating, and last) unless otherwise indicated.

	q [e]	σ [nm]	ϵ [kJ/mol]
C_α	-0.005	0.350	0.276
C_β	-0.120	0.350	0.276
$C_{\beta,\text{last}}$	-0.180	0.350	0.276
C_γ	-0.055	0.355	0.293
$C_{\gamma,\text{first}}$	-0.115	0.355	0.293
H_α, H_β	+0.060	0.250	0.126
C_δ, C_ϵ, C_ζ	-0.115	0.355	0.293
H_δ, H_ϵ, H_ζ	+0.115	0.242	0.126

A Model for Sodium Dodecyl Sulfate

Bonded and nonbonded parameters for SDS were adopted from the model of Shelley et al. [7, 8] However, because this model integrates the hydrogens of the methyl and methylene groups into the carbons to which they are connected, we performed quantum calculations, following the RESP (Restrained Electrostatic Potential) charge fitting procedure, [9] to determine the partial charges in these groups. Bonded interactions that were missing for the all-atom description were taken from the corresponding interactions of the OPLS-AA force-field. The resulting model is displayed in Fig. A I.2 and the non-bonded parameters in Table A I.3 The LJ parameters of the sodium counterion, σ=0.333 nm and ϵ=0.0116 kJ/mol, were taken from the OPLS-AA force-field.

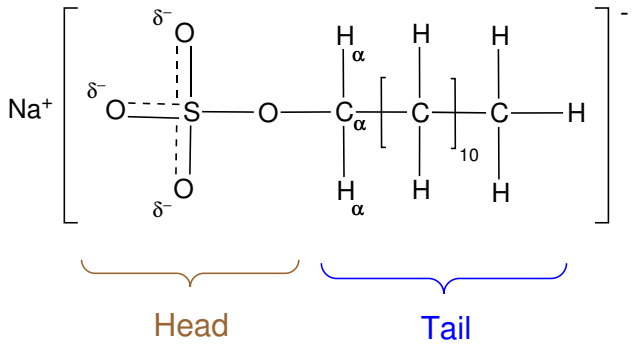

Figure A I.2: The model for SDS surfactant. The partial charge and LJ parameters describing each atom is detailed in Table A I.3.

Table A I.3: Partial charges and LJ parameters for the SDS model. The atoms are divided according to their association to the head or tail groups.

	q [e]	σ [nm]	ϵ [kJ/mol]
Head			
S	+1.284	0.355	1.046
O	-0.654	0.315	0.837
O_{ester}	-0.459	0.300	0.711
Tail			
C_α	+0.077	0.350	0.276
H_α	+0.030	0.242	0.063
C	-0.120	0.350	0.276
C_{last}	-0.180	0.350	0.276
H	+0.060	0.250	0.126

A Model for poly(ethylene oxide)-poly(ethylene)

For the PEO-PE surfactant, we considered molecules with two different lengths. The shorter surfactant, labeled as 7PEO4PE, is $HO-(CH_2CH_2O)_7-(CH_2)_7-CH_3$. The longer surfactant, labeled as 10PEO6PE, is $HO-(CH_2CH_2O)_{10}-(CH_2)_{11}-CH_3$ to which Disponil AFX1080 was compared experimentally. Results from a self-consistent field theory predicts that the head size of the surfactant influences the adsorption significantly. [10] Parameters for the PE and PEO segments of the surfactant were taken from the OPLS-AA force-field. [11] For the latter, the values were derived from dimethyl ether group. The model for this surfactant is given in Fig. A I.3 and Table A I.4.

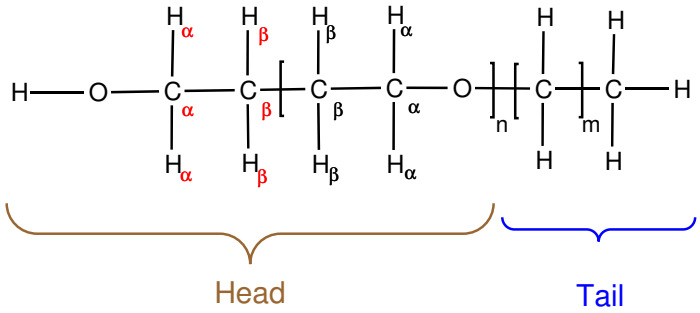

Figure A I.3: The model for PEO-PE surfactant. The partial charge and LJ parameters describing each atom is detailed in Table A I.4.

Table A I.4: Partial charges and LJ parameters for the PEO-PE surfactant model. The atoms are divided according to their association to the head or tail groups.

	q [e]	σ [nm]	ϵ [kJ/mol]
Head			
$C_{\alpha,\beta}$	+0.140	0.350	0.276
$C_{\alpha,\text{first}}$	-0.015	0.350	0.276
$H_{\alpha,\beta}$	+0.030	0.250	0.126
$H_{\alpha,\text{first}}$	+0.040	0.250	0.126
O	-0.400	0.290	0.586
O_{first}	-0.683	0.312	0.711
H_{first}	+0.418	0.000	0.000
Tail			
C	-0.120	0.350	0.276
C_{last}	-0.180	0.350	0.276
H	+0.060	0.250	0.126

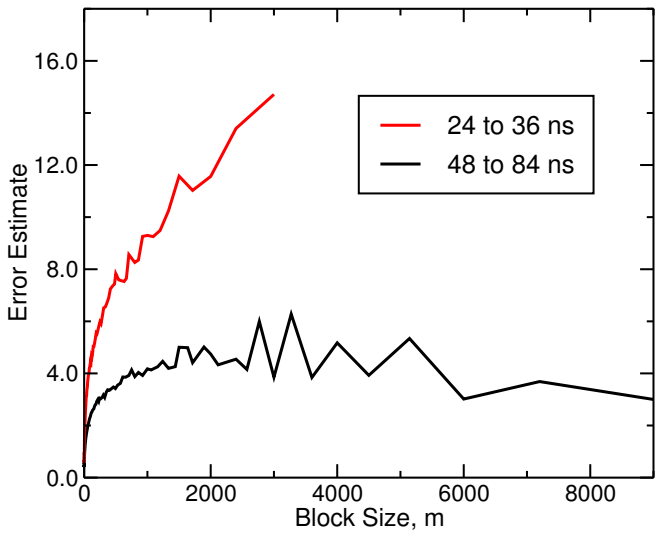

Figure A I.4: Analysis of the convergence of the constrained force along different segments of the trajectory for 10PEO6PE with 24 surfactants at d_c=0.103 nm. This point is in the vicinity of the equilibrium adsorbed state and convergence required longer simulation. In order to obtain an estimate for the error we used the block averaging method. The trajectory is divided into *n* number of blocks of equal size *m* and averages are calculated for each block. The error for the total average is calculated from the variance between the averages of the *n* blocks. The curves show this error estimate as a function of the block size *m*. The plot for the earlier and shorter segment of the trajectory (24–36 ns) continues to increase as the block size increases (or the number of blocks decreases) whereas the last and longer segment of the trajectory (48–84 ns) exhibits a plateau (and even a slight decrease due to sufficient number of blocks which are large enough) which signifies convergence.

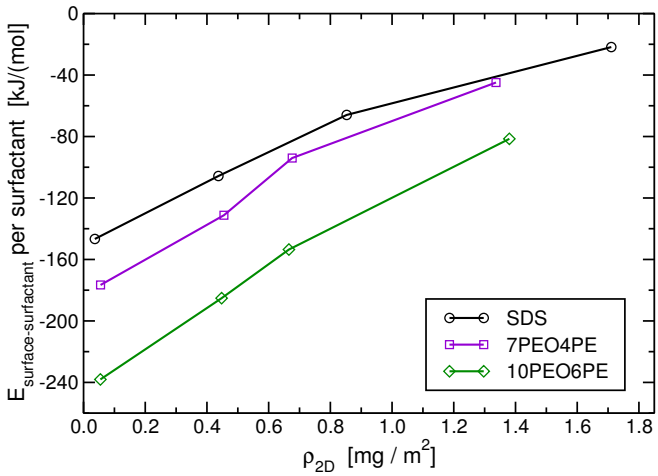

Figure A I.5: The surface-surfactant energy per surfactant as a function of the 2D-density.

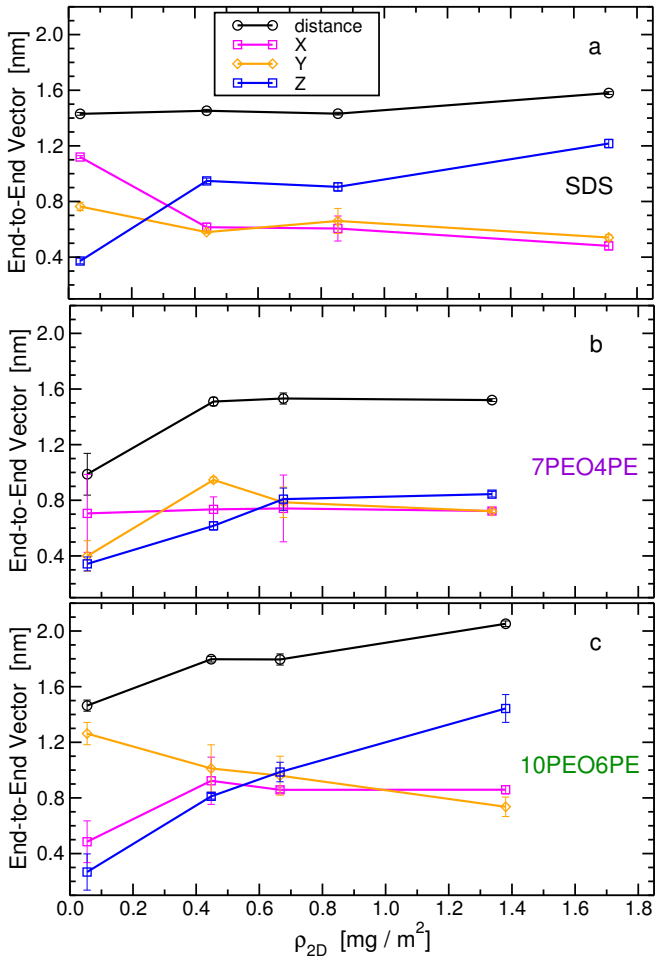

Figure A I.6: The end-to-end vector of the surfactant (between the heavy atoms at both ends) as a function of the 2D-density. The plots show the scalar distance as well as the projections parallel (x and y) and normal (z) to the interface plane. This analysis is performed for the equilibrium points (adsorbed state) of the pulling processes shown in Fig. III.5 averaged over the last 36 ns of the trajectories. Error bars are displayed, however, in some cases their size is comparable to the size of the symbols.

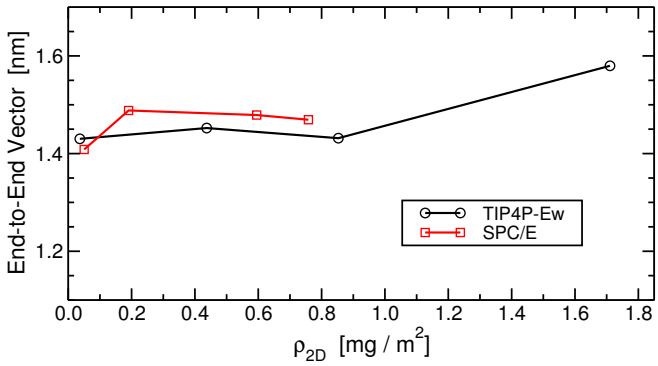

Figure A I.7: Comparison of the end-to-end distance (between the heavy atoms at both ends) of the SDS surfactants from simulations in which the water molecules were described by the TIP4P-Ew and SPC/E water models.

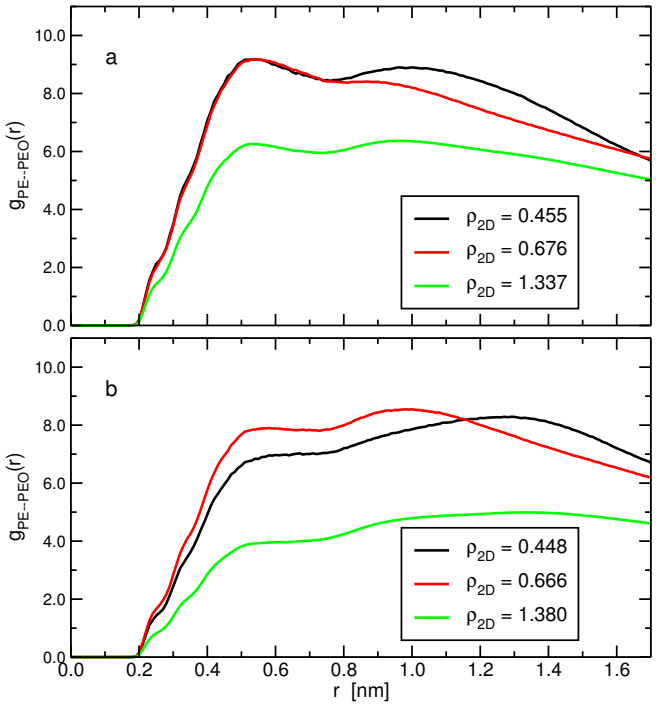

Figure A I.8: The radial distribution functions between the tail atoms (the PE segment) and head atoms (the PEO segment excluding the connecting –CH_2CH_2O– group) of different surfactants for different 2D-densities for the (a) 7PEO4PE and (b) 10PEO6PE systems. The analyzes are computed for the equilibrium points of the pulling processes shown in Fig. III.5 averaged over the last 36 ns of the trajectories.

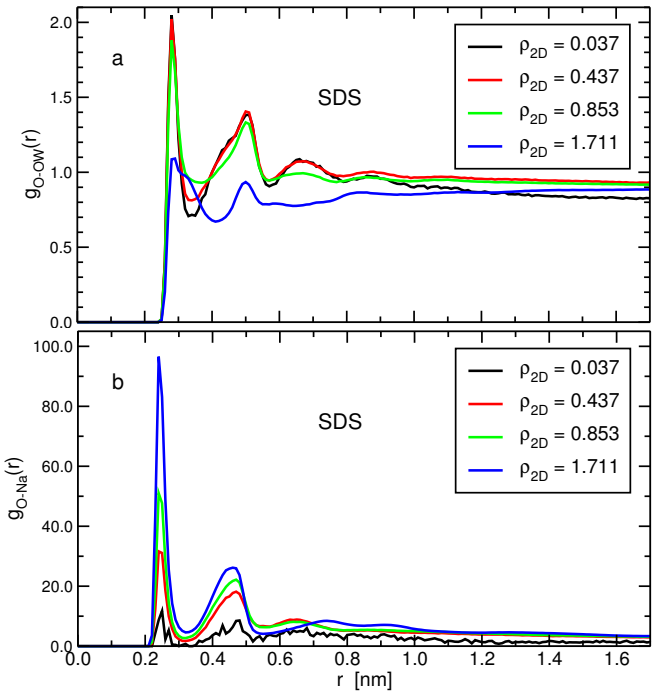

Figure A I.9: The radial distribution functions between the oxygen atoms of SDS and (a) the oxygen atoms of water, (b) the sodium cations, at different two-dimensional densities. The analyzes are computed for the equilibrium points (adsorbed state) of the pulling processes shown in Fig. III.5 averaged over the last 36 ns of the trajectories.

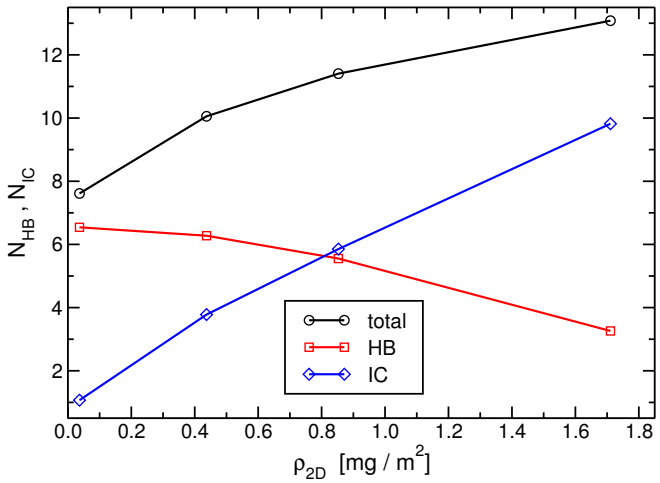

Figure A I.10: The number of hydrogen bonds and the number of ion contacts, per surfactant, between SDS molecules and the solvent as a function of the 2D-density. The analysis is performed in the adsorbed state.

The Effect of the Chain Stiffness

In order to investigate the effect of the stiffness of the nonionic surfactants on the structure of the adsorbed layer at the interface with the PS surface, we performed additional simulations for the long and short surfactants in which their dihedral angles were characterized by a much stiffer potentials ($V_d = k_\phi [1 + \cos(n\phi)]$ with k_ϕ=10 kJ/mol, ϕ=180 °, and n=3). For each system we considered 12 surfactants in exactly the same conditions as with the unperturbed systems except for the number of water molecules which were 4300 and 10500 for the 7PEO4PE and 10PEO6PE surfactants, respectively. The resulting 2D-densities were ρ_{2D}=0.681 and 0.702 mg/m^2 which are to be compared with the ρ_{2D}=0.666 and 0.676 mg/m^2 of the unperturbed OPLS-AA force-field for the short and long surfactants, respectively. The simulations were run in the adsorbed state for 100 ns and data were collected for 36 ns.

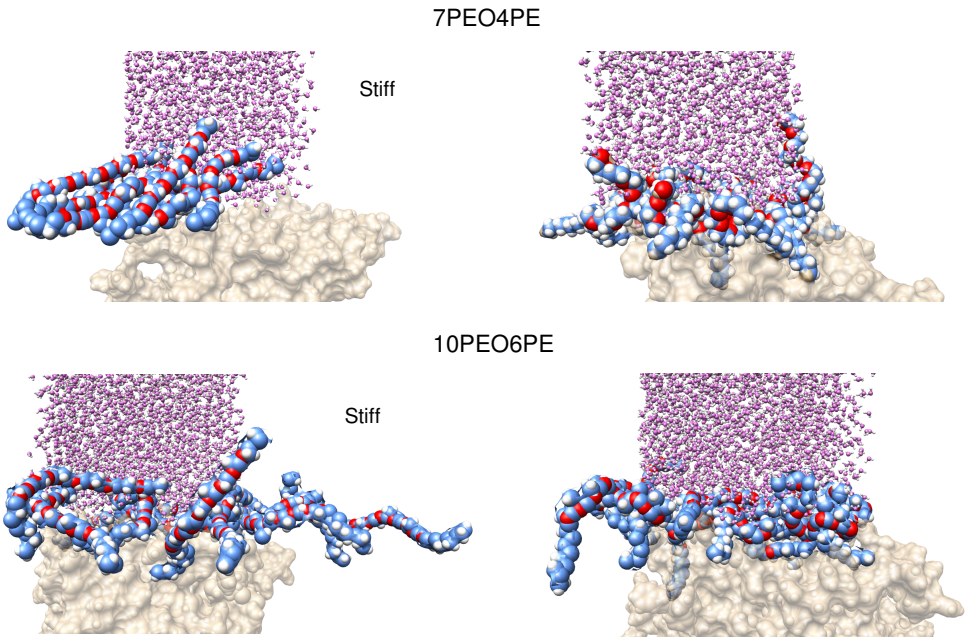

Figure A I.11: Snapshots from the simulations with the stiff nonionic surfactants described above (left panel) compared with those with unperturbed OPLSAA force field (right panel).

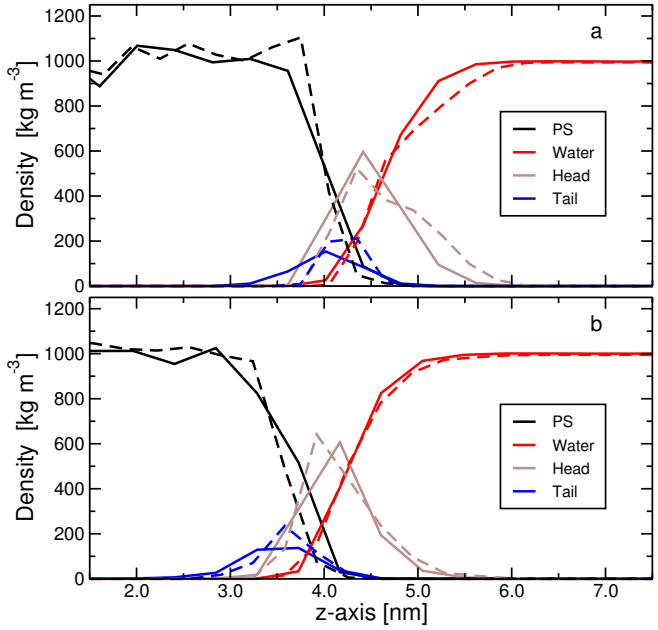

Figure A I.12: The density profiles of the system with the stiff (dashed lines) nonionic surfactants compared with those with the unperturbed OPLSAA force-field (solid lines) for the (a) 7PEO4PE and (b) 10PEO6PE systems. The profiles were superimposed on top of each other in such a way to maximize the overlap of the curves for the water phase.

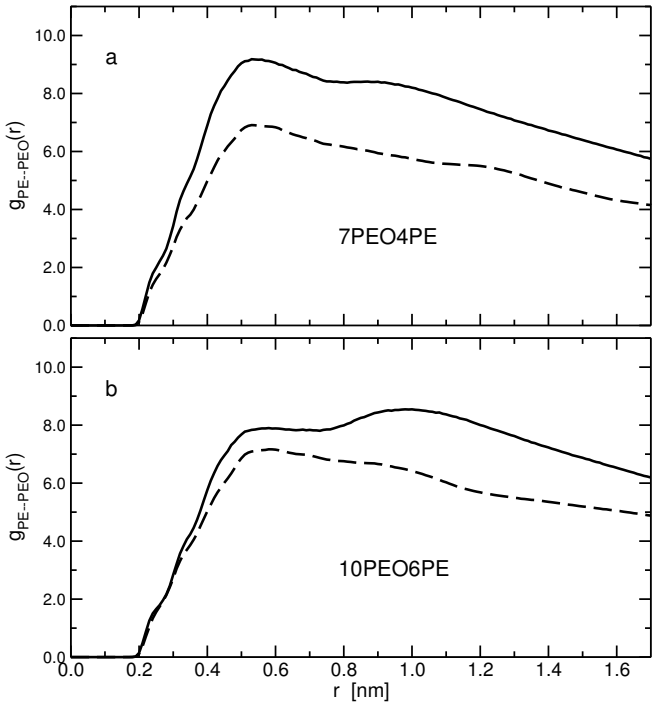

Figure A I.13: The radial distribution functions between the tail atoms (the PE segment) and head atoms (the PEO segment excluding the connecting –CH_2CH_2O– group) of different surfactants for the system with stiff (dashed lines) nonionic surfactants compared with those with unperturbed OPLSAA force-field (solid lines) for the (a) 7PEO4PE and (b) 10PEO6PE systems.

Table A I.5: The end-to-end distance, as well as its three components, of the surfactants with the stiff dihedral angles compared to those with the unperturbed dihedrals. In the last row we provide the number of hydrogen bonds, per surfactant, between the surfactants (head groups) and the water molecules.

	7PEO4PE		10PEO6PE	
End-to-End	stiff	unperturbed	stiff	unperturbed
distance	2.03	1.53	2.33	1.80
X	1.10	0.74	1.43	0.86
Y	1.23	0.79	1.34	0.96
Z	0.99	0.81	1.02	0.99
HB	5.0	6.1	6.2	7.9

References

[1] Jorgensen, W. L.; Severance, D. L. Aromatic-Aromatic Interactions: Free Energy Profiles for the Benzene Dimer in Water, Chloroform and Liquid Benzene, *J. Am. Chem. Soc.* 1990, *112*, 4768–4774.

[2] Price, M. L. P.; Ostrovsky, D.; Jorgensen, W. L. Gas-Phase and Liquid-State Properties of Esters, Nitriles, and Nitro Compounds with the OPLS-AA Force Field, *J. Comp. Chem.* 2001, *22*, 1340–1352.

[3] Brandrup, J.; Immergut, E. H.; Grulke, E. A. *Polymer Handbook;* Wiley: New York, fourth ed., 2003.

[4] Fetters, L. J.; Lohse, D. J.; Richter, D.; Witten, T. A.; Zirkel, A. Connection between Polymer Molecular Weight, Density, Chain Dimensions, and Melt Viscoelastic Properties, *Macromolecules* 1994, *27*, 4639–4647.

[5] Harmandaris, V. A.; Adhikari, N. P.; van der Vegt, N. F. A.; Kremer, K. Hierarchical Modeling of Polystyrene: From Atomistic to Coarse-Grained Simulations, *Macromolecules* 2006, *39*, 6708–6719.

[6] Spyriouni, T.; Tzoumanekas, C.; Theodorou, D.; Müller-Plathe, F.; Milano, G. Coarse-Grained and Reverse-Mapped United-Atom Simulations of Long-Chain Atactic Polystyrene Melts: Structure, Thermodynamic Prop-

erties, Chain Conformation, and Entanglements, *Macromolecules* 2007, *40*, 3876–3885.

[7] Shelley, J.; Watanabe, K.; Klein, M. L. Simulation of a sodium dodecylsulfate micelle in aqueous solution, *Int. J. Quant. Chem.* 1990, *38*, 103–117.

[8] Schweighofer, K. J.; Essmann, U.; Berkowitz, M. Simulation of Sodium Dodecyl Sulfate at the Water-Vapor and Water-Carbon Tetrachloride Interfaces at Low Surface Coverage, *J. Phys. Chem. B* 1997, *101*, 3793–3799.

[9] Bayly, C. I.; Cieplak, P.; Cornell, W.; Kollman, P. A. A well-behaved electrostatic potential based method using charge restraints for deriving atomic charges: the RESP model, *J. Phys. Chem.* 1993, *97*, 10269–10280.

[10] Jódar-Reyes, A. B.; Ortega-Vinuesa, J. L.; Martín-Rodríguez, A.; Leermakers, F. A. M. Self-Consistent Field Model of Inhomogeneous Adsorption of Nonionic Surfactants onto Polystyrene Latex, *Langmuir* 2003, *19*, 878–887.

[11] Jorgensen, W. L.; Maxwell, D. S.; Tirado-Rives, J. Development and testing of the opls all-atom force field on conformational energetics and properties of organic liquids, *J. Am. Chem. Soc.* 1996, *118*(45), 11225–11236.

Appendix II

Supplementary Information Chapter IV

Table A II.6: Details of the simulations for the five organic phases (different composition of PS and styrene) studied. For each organic phase, we considered four concentrations (eleven for 100% S) of 10PEO6PE surfactants. The average lengths of the simulation box along each axis are indicated (the interfaces between water and the organic phase are normal to the z-axis). The values of the 2D-densities, ρ_{2D}, are initial values which do not take into consideration absorption into the organic phase at equilibrium. For the system with 100% S the box lengths in the x- and y-axes are the same.

	# 16-mer PS	# S	# 10PEO6PE	ρ_{2D} [mg/m^2]	# Waters	$\langle X \rangle$ [nm]	$\langle Y \rangle$	$\langle Z \rangle$ [nm]
100% S	0	2304	0	0	8170	5.17	5.17	25.00
	0	2304	2	0.0405	8170	5.18	5.18	25.00
	0	2304	6	0.121	8170	5.20	5.20	25.00
	0	2304	8	0.161	8170	5.20	5.20	25.00
	0	2304	12	0.240	8170	5.22	5.22	25.00
	0	2304	18	0.378	8604	5.09	5.09	27.00
	0	2304	20	0.419	8604	5.10	5.10	27.00
	0	2304	30	0.619	8604	5.13	5.13	27.00
	0	2304	40	0.814	8604	5.17	5.17	27.00
	0	2304	80	1.53	11630	5.33	5.33	30.00
	0	2304	120	2.20	11630	5.45	5.45	30.00

Continued on next page

Table A II.6 – continued from previous page

	# 16-mer PS	# S	# 10PEO6PE	ρ_{2D} [mg/m^2]	# Waters	⟨X⟩ [nm]	⟨Y⟩	⟨Z⟩ [nm]
25% PS / 75% S	36	1728	0	0	14208	5.64	6.74	22.00
	36	1728	18	0.244	15130	5.79	6.92	22.00
	36	1728	62	0.826	14208	5.84	6.99	22.00
	36	1728	122	1.66	11628	5.79	6.92	22.00
50% PS / 50% S	72	1152	0	0	13036	6.66	5.65	21.00
	72	1152	18	0.255	13036	6.73	5.71	21.00
	72	1152	56	0.767	12678	6.84	5.81	21.00
	72	1152	114	1.56	13308	6.83	5.80	23.00
75% PS / 25% S	108	576	0	0	14392	6.79	5.50	22.00
	108	576	18	0.256	14392	6.87	5.56	22.00
	108	576	62	0.875	13138	6.90	5.59	22.00
	108	576	124	1.70	11892	7.00	5.67	22.00
100% PS	144	0	0	0	13238	6.35	5.94	21.00
	144	0	18	0.252	13238	6.45	6.03	20.84
	144	0	56	0.779	12148	6.47	6.04	20.86
	144	0	112	1.56	10404	6.45	6.03	21.00

Table A II.7: Details of the simulation setups for the SDS surfactants studied at two different 2D-densities with 100% S as the organic phase. The data collection time was 20 ns, and the equilibration time was 80 and 100 ns for the systems with 146 and 200 SDSs, respectively. The box lengths in the x- and y-axes are the same.

# SDS	ρ_{2D} [mg/m^2]	# S	# Waters	$\langle X \rangle / \langle Y \rangle$ [nm]	$\langle Z \rangle$ [nm]
146	1.24	2304	5286	5.31	22.80
200	1.65	2304	5203	5.39	22.80

Table A II.8: Details of the simulation setups for the calculations of the potential of mean force of pulling one 10PEO6PE surfactant adsorbed at the interface to the water phase. The different densities, reported as ρ_{2D}, correspond to different numbers of surfactants initially placed at the interface.

# 10PEO6PE	ρ_{2D} [mg/m^2]	# S	# Waters	$\langle X \rangle / \langle Y \rangle$ [nm]	$\langle Z \rangle$ [nm]
1	0.0538	384	4113	4.50	9.70
8	0.453	384	11452	4.38	22.04
12	0.686	384	8006	4.36	17.05

Models for Styrene and Poly(styrene)

The bonded and non-bonded parameters for styrene and PS were taken from the OPLS-AA force-field of ethylbenzene and ethylene molecules. [1–3] However for PS, in order to allow the connectivity between the subunits and simultaneously maintain zero charge for each of these subunits, we made the following changes. The partial charge of C_β of the first residue was changed from -0.180 to -0.120, that of C_γ of the last residue was changed from -0.115 to -0.055, and both changes were applied to the repeating residues. The chain of PS is modeled as a 16-mer unit. Because the stereochemistry of each unit is randomly generated during polymerization, we chose to model each chain with alternating C_α chiral centers (R followed by S). The resulting model is shown in Figure A II.14 and the non-bonded interactions are specified in Table A II.9. Using this model, we obtained a value of 1.02 kg/m^3 for the density of amorphous PS which is close to its experimental value [4] of 1.04–1.06 kg/m^3. Furthermore, the calculated values of the radius of gyration, 9.8 Å, and the weight-normalized end-to-end distance squared, 0.42 Å$^2\cdot$ mol/g, are also in a very good agreement with their experimentally determined values of 10.0 Å and 0.43 Å$^2\cdot$ mol/g, respectively.

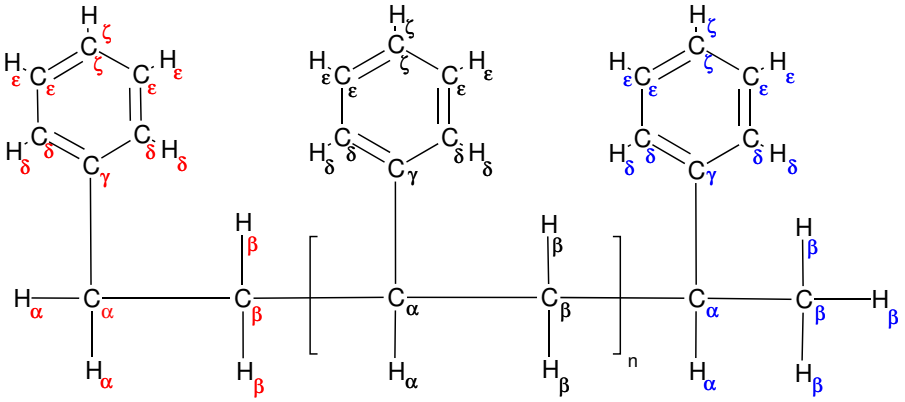

Figure A II.14: The model for PS based on the OPLS-AA force-field. The partial charge and LJ parameters describing each atom are detailed in Table A II.9. Note that the C_α of the repeating and last residues are chirals, nevertheless, the parameters for the R and S configurations are the same.

Table A II.9: Partial charges and LJ parameters for the PS model. The values refer to all residue types (first, repeating, and last) unless otherwise indicated.

	q [e]	σ [nm]	ϵ [kJ/mol]
C_α	-0.005	0.350	0.276
C_β	-0.120	0.350	0.276
$C_{\beta,\text{last}}$	-0.180	0.350	0.276
C_γ	-0.055	0.355	0.293
$C_{\gamma,\text{first}}$	-0.115	0.355	0.293
H_α, H_β	+0.060	0.250	0.126
C_δ, C_ϵ, C_ζ	-0.115	0.355	0.293
H_δ, H_ϵ, H_ζ	+0.115	0.242	0.126

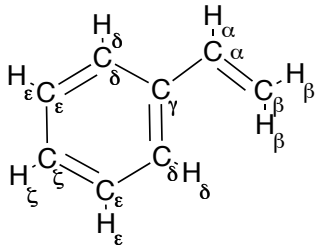

Figure A II.15: The model for a styrene molecule. The OPLS-AA partial charges and LJ parameters are detailed in Table A II.10.

Table A II.10: Partial charges and LJ parameters for styrene.

	q [e]	σ [nm]	ϵ [kJ/mol]
C_α	-0.115	0.355	0.318
C_β	-0.230	0.355	0.318
C_γ	-0.115	0.355	0.293
H_α	+0.23	0.242	0.126
H_β	+0.115	0.242	0.126
C_δ, C_ϵ, C_ζ	-0.115	0.355	0.293
H_δ, H_ϵ, H_ζ	+0.115	0.242	0.126

A Model for poly(ethylene oxide)-poly(ethylene)

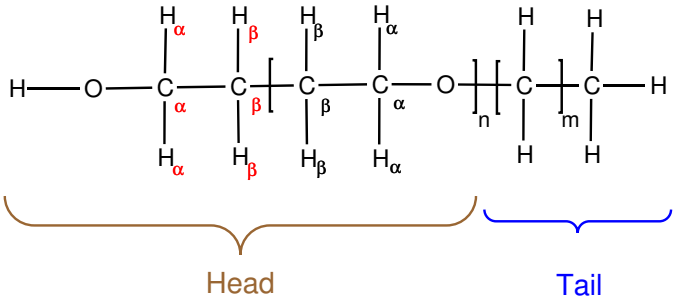

Figure A II.16: The model for 10PEO6PE surfactant (n=10 and m=11). The partial charges and LJ parameters, taken from the OPLS-AA force-field, are detailed in Table A II.11. For PEO, the values were based on a dimethyl ether.

Table A II.11: Partial charges and LJ parameters for the PEO-PE surfactant model. The atoms are divided according to their association to the head or tail groups.

	q [e]	σ [nm]	ϵ [kJ/mol]
Head			
$C_{\alpha,\beta}$	+0.140	0.350	0.276
$C_{\alpha,\text{first}}$	-0.015	0.350	0.276
$H_{\alpha,\beta}$	+0.030	0.250	0.126
$H_{\alpha,\text{first}}$	+0.040	0.250	0.126
O	-0.400	0.290	0.586
O_{first}	-0.683	0.312	0.711
H_{first}	+0.418	0.000	0.000
Tail			
C	-0.120	0.350	0.276
C_{last}	-0.180	0.350	0.276
H	+0.060	0.250	0.126

A Model for Sodium Dodecyl Sulfate

Partial charges, bonded and nonbonded parameters for SDS were adopted from the model of Shelley et al. [5, 6]. Note that this model integrates the hydrogens of the methyl and methylene groups into the carbons to which they are connected. To obtain an all-atom representation, we represented the atom-types and partial charges of methyl and methylene groups by the OPLS-AA force-field for hydrocarbons. The sum of the charges for each of these groups is zero, therefore, in order to determine the partial charges of the first methylene group (which has a total charge of $+0.137$ e), we performed quantum calculations (using the Gaussian09 software [7] at the MP2/6-31++G**) and followed the RESP (Restrained Electrostatic Potential) charge fitting procedure [8]. Bonded interactions that were missing for the all-atom description were taken from the corresponding interactions of the OPLS-AA force-field. The resulting model is displayed in Figure A II.17 and the non-bonded parameters in Table A II.12 The LJ parameters of the sodium counterion, σ=0.333 nm and ϵ=0.0116 kJ/mol, were taken from the OPLS-AA force-field. Note that the charges obtained by RESP reproduce the, quantum mechanically determined, electrostatic potential at large number of grid points around the optimized geometry of the molecule. Thus, their values can differ substantially from the atomic charges determined quantum mechanically (e.g, as defined by Mulliken) for the same optimized molecular structrure (see Figure A II.18).

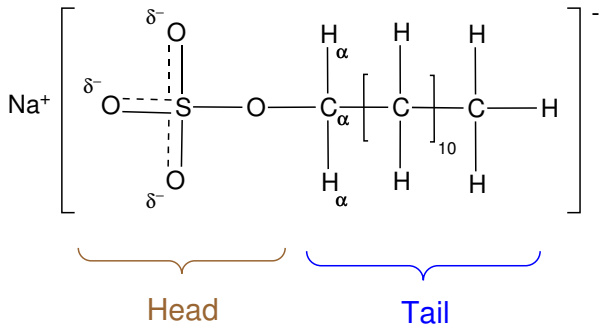

Figure A II.17: The model for SDS surfactant. The partial charge and LJ parameters describing each atom are detailed in Table A II.12.

Table A II.12: Partial charges and LJ parameters for the SDS model. The atoms are divided according to their association to the head or tail groups.

	q [e]	σ [nm]	ϵ [kJ/mol]
Head			
S	+1.284	0.355	1.046
O	-0.654	0.315	0.837
O_{ester}	-0.459	0.300	0.711
Tail			
C_α	+0.077	0.350	0.276
H_α	+0.030	0.242	0.063
C	-0.120	0.350	0.276
C_{last}	-0.180	0.350	0.276
H	+0.060	0.250	0.126

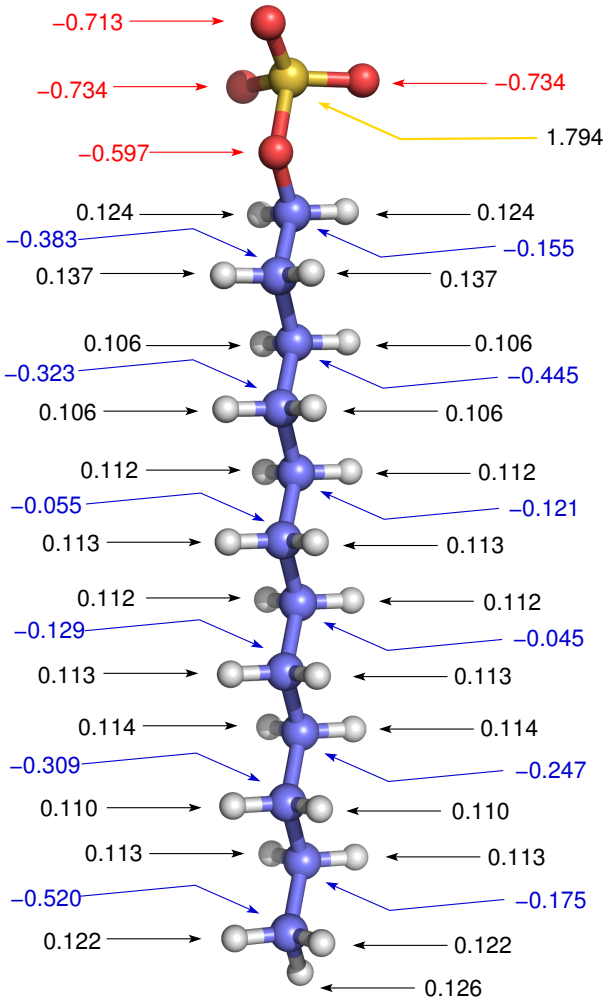

Figure A II.18: Atomic (Mulliken) charges (in elementary charge units, e) for the dodecyl sulfate anion optimized quantum mechanically at the MP2/6-31++G** level. These charges were *not* used in the classical simulations.

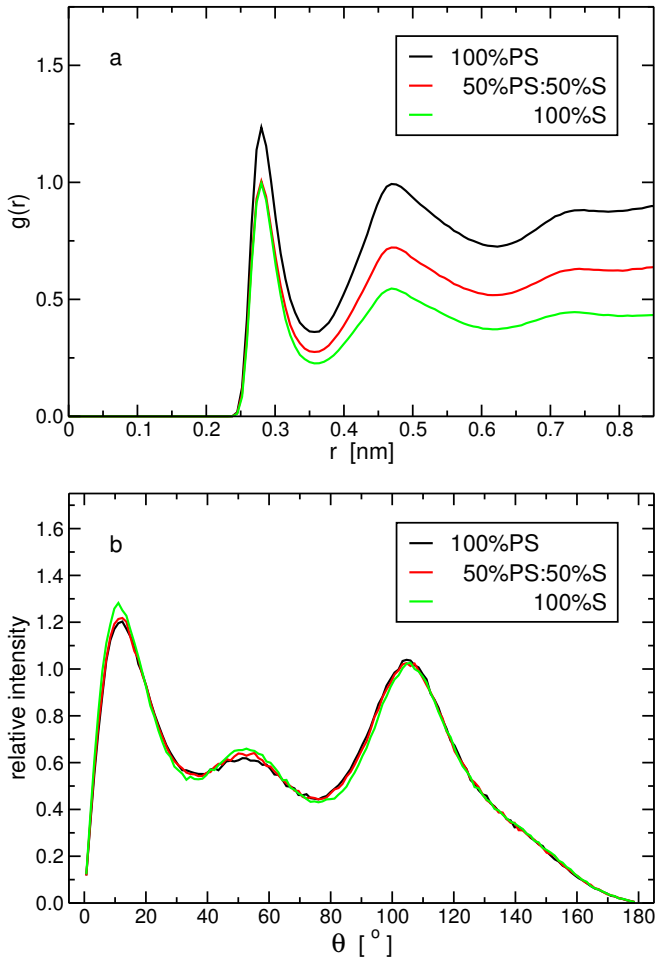

Figure A II.19: (a) The radial distribution function between the oxygen atoms of the nonionic surfactant and the oxygen atoms of the water molecules. (b) The distribution of the angle formed by the hydrogen–oxygen(water)–oxygen(surfactant) atomic sites for donor–acceptor distances smaller than 0.35 nm. For both plots, the corresponding distributions were calculated for three different chemical compositions of the organic phase.

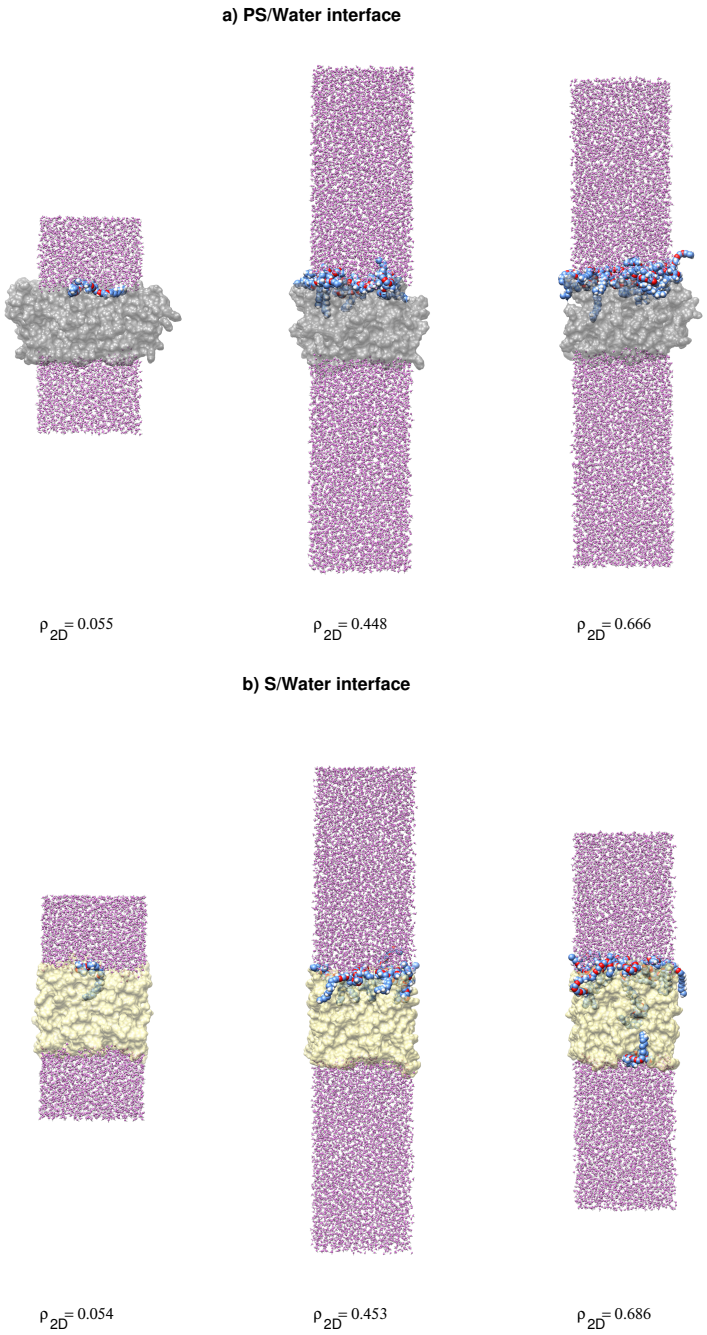

Figure A II.20: Same as Figure IV.10, however here, the entire length of the simulation box along the z-axis (normal to the interface) is shown for all snapshots.

Relation between the Surfactant Densities at the Interface and inside the Organic Phase

The chemical potential of the surfactant in the organic phase is given by,

$$\mu_{op} = \mu^{\circ}_{op} + RT \ln a_{op} = \mu^{\circ}_{op} + RT \ln \left[\gamma_{op} \frac{\rho_{op}}{\rho^{\circ}_{op}} \right] \quad , \tag{1}$$

where μ°_{op} is the chemical potential in the organic phase under standard conditions of temperature, pressure, and density. The term a_{op} is the activity of the surfactants relative to the standard state, which can be written in terms of the activity coefficient, γ_{op}, and the surfactant density relative to that chosen for the standard state. A corresponding term holds at the interface,

$$\mu_{int} = \mu^{\circ}_{int} + RT \ln \left[\gamma_{int} \frac{\rho_{int}}{\rho^{\circ}_{int}} \right] \quad . \tag{2}$$

At equilibrium, $\mu_{op} = \mu_{int}$, from which we get,

$$\rho_{op} = \frac{\gamma_{int}}{\gamma_{op}} \cdot \frac{\rho^{\circ}_{op}}{\rho^{\circ}_{int}} \exp \left[- \left(\mu^{\circ}_{op} - \mu^{\circ}_{int} \right) / RT \right] \rho_{int} \quad . \tag{3}$$

The terms associated with the standard states and the activity coefficients are constants with respect to the concentration of the surfactant, and therefore, a plot of ρ_{op} as a function of ρ_{int} should yield a straight line as obtained in Figure IV.12a in Chapter IV. Note that the lines do not pass through the origin, because below the critical density the surfactant does not absorb into the organic phase and the there is no equality between the chemical potentials (i.e., Equation 3 does not hold). In fact in this case, the chemical potential of the surfactant in the organic phase is larger than that in that at the interface.

Taking the derivative of Equation 3 with respect to ρ_{int} on both sides of Equation 3 yields,

$$\frac{d\rho_{op}}{d\rho_{int}} = \frac{\gamma_{int}}{\gamma_{op}} \cdot \frac{\rho^{\circ}_{op}}{\rho^{\circ}_{int}} \exp \left[- \left(\mu^{\circ}_{op} - \mu^{\circ}_{int} \right) / RT \right] \quad , \tag{4}$$

which can also be written as,

$$\ln\left[\frac{d\rho_{op}}{d\rho_{int}}\right] = \mu^{\circ}_{int}/RT + \ln\left[\frac{\gamma_{int}}{\gamma_{op}} \cdot \frac{\rho^{\circ}_{op}}{\rho^{\circ}_{int}}\right] - \mu^{\circ}_{op}/RT \quad . \tag{5}$$

Note that, in principle, for different organic phases μ°_{int} is different. Nevertheless in our systems for which the surfactant exhibits non-zero density inside the organic phase, it is almost exclusively styrene that is found at the interface with water (see Figure IV.11 in Chapter IV for 100% S, 75% S, and 50% S). Because of this observation we consider that μ°_{int} and γ_{int} are independent of these three organic phases. In addition, we also make the assumption that the value of γ_{op}, which represents the degree of deviation from an ideal behavior, is the same for these systems.

Under these two assumptions, Equation 5 indicates that the natural logarithm of the slopes of the lines in Figure IV.12a in Chapter IV, for different chemical compositions of the organic phase, are only a function of μ°_{op} where all other terms enter as constant parameters. For an organic phase composed of styrene and PS, one may naively try to relate μ°_{op} to the chemical potential of styrene in the standard state, μ°_{str}, and that of PS, μ°_{ps}, weighted linearly by the corresponding fractions in the organic phase, χ_{str} and 1 - χ_{str}, respectively.

$$\mu^{\circ}_{op} \simeq \chi_{str}\mu^{\circ}_{str} + (1 - \chi_{str})\mu^{\circ}_{ps} \tag{6}$$

In such a case, Equation 5 becomes,

$$\ln\left[\frac{d\rho_{op}}{d\rho_{int}}\right] = \left(\mu^{\circ}_{int} - \mu^{\circ}_{ps}\right)/RT + \ln\left[\frac{\gamma_{int}}{\gamma_{op}} \cdot \frac{\rho^{\circ}_{op}}{\rho^{\circ}_{int}}\right] - \left(\mu^{\circ}_{str} - \mu^{\circ}_{ps}\right)/RT \cdot \chi_{str} \quad . \tag{7}$$

Thus, plotting $\ln\left[\frac{d\rho_{op}}{d\rho_{int}}\right]$ as a function of χ_{str} should yield a straight line with a slope equals -$\left(\mu^{\circ}_{str} - \mu^{\circ}_{ps}\right)/RT$. This is plotted in Figure A II.21 for the three organic phases containing non-zero surfactant density.

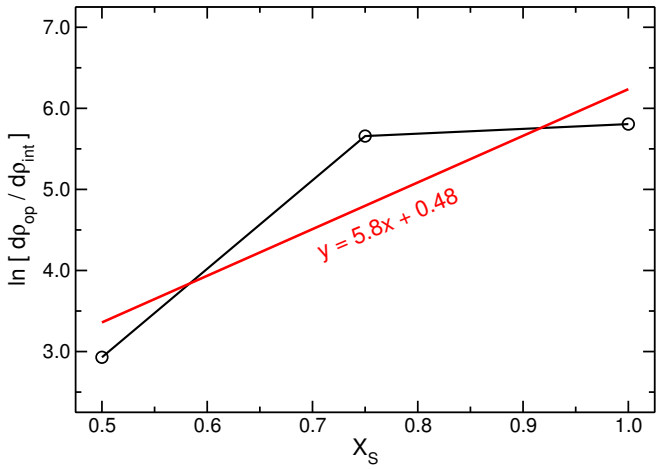

Figure A II.21: The natural logarithm of the slopes of the lines shown in Figure IV.12a (for 100% S, 75% S, and 50% S) as a function of the mass fraction of styrene in the organic phase (see Equation 7). Only points surrounded by orange circles in Figure IV.12a are used for the calculations of the slopes. The red line is a linear regression obtained with a correlation coefficient of 0.888.

The slope of 5.8 of the linear regression means that μ°_{str} is smaller by 5.8 RT than μ°_{ps}, which is in agreement with the observation that the surfactant absorbs significantly more in the styrene phase relative to the PS phase. Nevertheless, the relatively small correlation coefficient for the linear fitting suggests that μ°_{op} deviates from the simplistic expression we assumed, and/or the value of γ_{op} varies for the three organic phases. In particular, for 75% S the organic phase resembles 100% S more than expected based on linear interpolation of the mass fractions of the two components, whereas for 50% S, it resembles less.

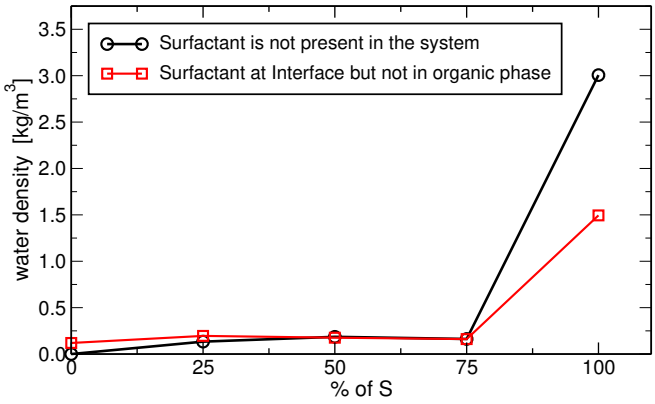

Figure A II.22: The density of the water molecules inside the organic phase as a function of the percentage of styrene composing the organic phase. The data are plotted for cases in which no surfactant (10PEO6PE) is either present at all in the system or absorbed inside the organic phase (but adsorb at the interface). For the latter, we chose the system with the highest density of surfactant at the interface that does not support absorbance into the organic phase.

References

[1] Jorgensen, W. L.; Severance, D. L. Aromatic-Aromatic Interactions: Free Energy Profiles for the Benzene Dimer in Water, Chloroform and Liquid Benzene, *J. Am. Chem. Soc.* 1990, *112*, 4768–4774.

[2] Jorgensen, W. L.; Maxwell, D. S.; Tirado-Rives, J. Development and testing of the opls all-atom force field on conformational energetics and properties of organic liquids, *J. Am. Chem. Soc.* 1996, *118*(45), 11225–11236.

[3] Price, M. L. P.; Ostrovsky, D.; Jorgensen, W. L. Gas-Phase and Liquid-State Properties of Esters, Nitriles, and Nitro Compounds with the OPLS-AA Force Field, *J. Comp. Chem.* 2001, *22*, 1340–1352.

[4] Brandrup, J.; Immergut, E. H.; Grulke, E. A. *Polymer Handbook;* Wiley: New York, fourth ed., 2003.

[5] Shelley, J.; Watanabe, K.; Klein, M. L. Simulation of a sodium dodecylsulfate micelle in aqueous solution, *Int. J. Quant. Chem.* 1990, *38*, 103–117.

[6] Schweighofer, K. J.; Essmann, U.; Berkowitz, M. Simulation of Sodium Dodecyl Sulfate at the Water-Vapor and Water-Carbon Tetrachloride Interfaces at Low Surface Coverage, *J. Phys. Chem. B* 1997, *101*, 3793–3799.

[7] Gaussian 09 Revision A.02. Frisch, M. J.; Trucks, G. W.; Schlegel, H. B.; Scuseria, G. E.; Robb, M. A.; Cheeseman, J. R.; Scalmani, G.; Barone,

V.; Mennucci, B.; Petersson, G. A.; Nakatsuji, H.; Caricato, M.; Li, X.; Hratchian, H. P.; Izmaylov, A. F.; Bloino, J.; Zheng, G.; Sonnenberg, J. L.; Hada, M.; Ehara, M.; Toyota, K.; Fukuda, R.; Hasegawa, J.; Ishida, M.; Nakajima, T.; Honda, Y.; Kitao, O.; Nakai, H.; Vreven, T.; Montgomery, Jr., J. A.; Peralta, J. E.; Ogliaro, F.; Bearpark, M.; Heyd, J. J.; Brothers, E.; Kudin, K. N.; Staroverov, V. N.; Kobayashi, R.; Normand, J.; Raghavachari, K.; Rendell, A.; Burant, J. C.; Iyengar, S. S.; Tomasi, J.; Cossi, M.; Rega, N.; Millam, J. M.; Klene, M.; Knox, J. E.; Cross, J. B.; Bakken, V.; Adamo, C.; Jaramillo, J.; Gomperts, R.; Stratmann, R. E.; Yazyev, O.; Austin, A. J.; Cammi, R.; Pomelli, C.; Ochterski, J. W.; Martin, R. L.; Morokuma, K.; Zakrzewski, V. G.; Voth, G. A.; Salvador, P.; Dannenberg, J. J.; Dapprich, S.; Daniels, A. D.; Farkas, Ö.; Foresman, J. B.; Ortiz, J. V.; Cioslowski, J.; Fox, D. J.; Gaussian, Inc., Wallingford, CT, 2009.

[8] Bayly, C. I.; Cieplak, P.; Cornell, W.; Kollman, P. A. A well-behaved electrostatic potential based method using charge restraints for deriving atomic charges: the RESP model, *J. Phys. Chem.* 1993, *97*, 10269–10280.

Appendix III

Supplementary Information Chapter V

Table A III.13: The number of chains of each polymer (each chain contains seven monomer units), their total mass, m_p, and the polymer/graphene mass ratio, m_p/m_G, which is designed to be constant for all systems. In all simulations, including those with bare graphene, the number of carbon atoms of the two graphene sheets is 45472 corresponding to a mass of $9.070 \cdot 10^{-19}$ g.

polymer	N_{chains}	m_p [10^{-19} g]	m_p / m_G
PMMA	808	9.242	1.019
PEAM	624	9.244	1.019
DAPM	492	9.264	1.021
PAAM	480	9.257	1.021
PDAFMA	420	9.252	1.020
PS	760	9.234	1.018

Table A III.14: The density of CO_2 gas, in kg/m^3, in the bulk region of the simulation box for the different polymer-graphene composite systems as well as for bare graphene. $N°_{CO_2}$ is the total number of carbon dioxide molecules in the simulation box.

$N°_{CO_2}$	G	G-PMMA	G-PEAM	G-DAPM	G-PAAM	G-PDAFMA	G-PS
200	0.097	0.158	0.128	0.095	0.092	0.071	0.532
400	0.179	0.382	0.269	0.214	0.185	0.152	0.769
700	0.323	0.702	0.494	0.396	0.356	0.300	1.346
1400	0.722	1.945	1.120	1.009	0.937	0.792	2.352
2100	1.170	3.076	1.928	1.683	1.592	1.294	4.039
2700	1.663	3.926	2.789	2.470	2.399	1.875	5.194
3500	2.423	5.111	3.903	3.360	3.365	3.228	6.732
5250	4.547	8.199	6.526	6.186	5.578	5.065	9.171
7000	7.078	11.272	9.152	8.601	8.267	8.161	12.389

Table A III.15: The density of N_2 gas, in kg/m^3, in the bulk region of the simulation box for the different polymer-graphene composite systems as well as for bare graphene. $N°_{N_2}$ is the total number of nitrogen molecules in the simulation box.

$N°_{N_2}$	G	G-PMMA	G-PEAM	G-DAPM	G-PAAM	G-PDAFMA	G-PS
200	0.204	0.205	0.189	0.175	0.139	0.130	0.127
400	0.404	0.429	0.377	0.367	0.292	0.277	0.490
700	0.706	0.760	0.686	0.648	0.537	0.522	0.857
1400	1.416	1.599	1.425	1.359	1.157	0.744	1.754
2100	2.146	2.435	2.193	2.103	1.883	1.849	2.571
2700	2.796	3.139	2.876	2.798	2.492	2.465	3.305
3500	3.718	4.086	3.816	3.690	3.395	3.533	4.285
5250	5.801	6.216	5.814	5.655	5.216	5.164	6.616
7000	7.956	8.322	7.871	7.738	7.298	7.631	8.810

Table A III.16: The density of CH_4 gas, in kg/m^3, in the bulk region of the simulation box for the different polymer-graphene composite systems as well as for bare graphene. $N°_{CH_4}$ is the total number of methane molecules in the simulation box.

$N°_{CH_4}$	G	G-PMMA	G-PEAM	G-DAPM	G-PAAM	G-PDAFMA	G-PS
200	0.097	0.117	0.108	0.096	0.098	0.090	0.065
400	0.179	0.249	0.213	0.200	0.178	0.176	0.280
700	0.323	0.445	0.375	0.367	0.359	0.330	0.491
1400	0.722	0.993	0.812	0.815	0.792	0.744	0.982
2100	1.170	1.502	1.320	1.280	1.277	1.171	1.473
2700	1.420	1.923	1.771	1.733	1.741	1.555	1.893
3500	2.423	2.507	2.342	2.273	2.303	2.408	2.454
5250	4.547	3.816	3.669	3.646	3.582	3.489	3.846
7000	7.078	5.112	4.945	4.901	4.868	5.072	5.154

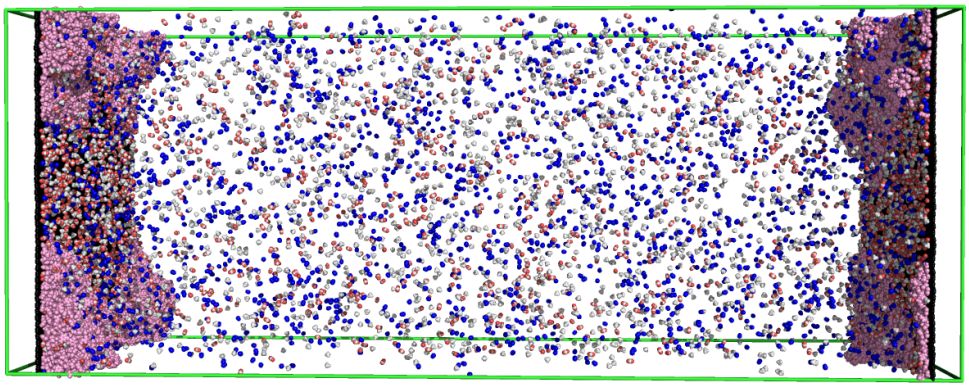

Figure A III.23: A snapshot of the last configuration of the G-PDAFMA composite system with $\frac{1}{3}N^{o}_{gas}$=2700. Graphene is shown as black sticks, the polymer is colored in magenta with a sphere representation. Gas molecules are displayed as spheres, where hydrogens are colored in white, oxygens in red, nitrogens in blue and carbons in gray.

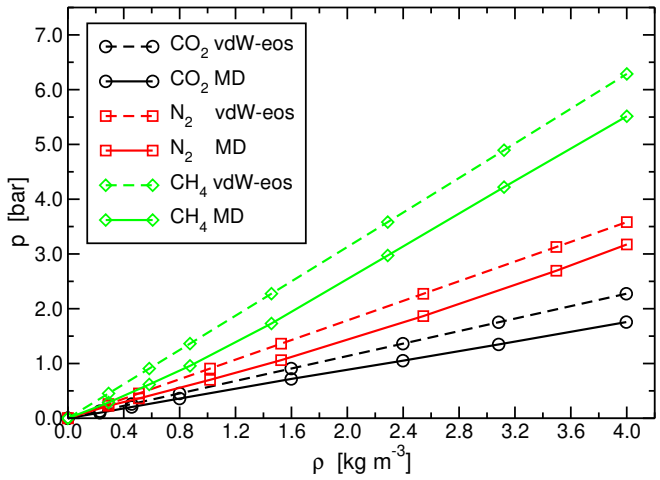

Figure A III.24: Pressure-density curves from simulations at 300 K of a homogeneous one-component bulk gas system for the CO_2, N_2, and CH_4 models employed in this study. The corresponding van der Waals equations of state, in which the a and b parameters were fitted to experimental results (see Table A III.17), are plotted for comparison. The NVT simulations were performed with a cubic box of 40.0 nm length for all densities. The random starting positions of the gas molecules were equilibrated for a time period of 30 ns with an additional 10 ns of data collection step. Other simulation details were the same as those described for the graphene-polymer composite systems.

Table A III.17: The experimentally determined coefficients [1][:ms-ref] of the van der Waals equation of state, $p = nRT/(V - nb) - an^2/V^2$, for CO_2, N_2, CH_4. In this equation, p, V, T, n, and R, are the pressure, volume, temperature, number of moles, and the gas constant, respectively.

	a [atm·L^2·mol^{-2}]	b [10^{-2}·L·mol^{-1}]
CO_2	3.610	4.290
N_2	1.352	3.870
CH_4	2.273	4.310

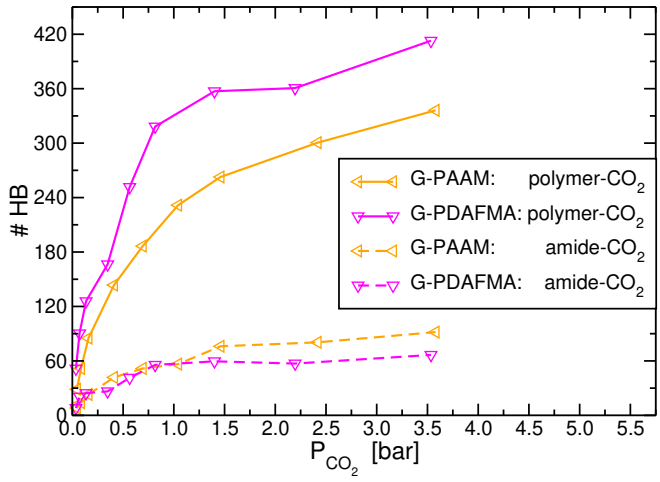

Figure A III.25: The contribution of the amide group in PAAM and PDAFMA (the group connecting the backbone to the aromatic rings) to the formation of hydrogen bonds between the polymer and CO_2. Solid-lines exhibit the total number of hydrogen bonds between the polymer and CO_2 (same as those shown in Fig. V.9) whereas the dashed-lines the values only due the amide groups.

Force-Fields of the Polymers Considered in this Study

Adopting the OPLS-AA force field, the different energetic terms take the following functional forms,

Bond stretching:

$$E_{bond} = \sum_{bonds} K_b(r - r_0)^2$$

Bond angle bending:

$$E_{angle} = \sum_{angles} K_\theta(\theta - \theta_0)^2$$

Torsion angle twisting:

$$E_{torsion}(\phi_{ijkl}) = \sum_{torsions} \frac{1}{2}[C_1(1 + \cos(\phi)) + C_2(1 - \cos(2\phi)) + C_3(1 + \cos(3\phi)) + C_4(1 + \cos(4\phi))]$$

Ryckaert-Bellemans dihedral energy function

Improper dihedrals angle:

$$E_{improper}(\phi_{ijkl}) = k_\phi(1 + \cos(n\phi - \phi_s))$$

Non-bonded:

$$E_{non-bonded} = \sum_i \sum_{j>i} \left\{ 4\epsilon_{ij} \left[\left(\frac{\sigma_{ij}}{r_{ij}} \right)^{12} - \left(\frac{\sigma_{ij}}{r_{ij}} \right)^{6} \right] + \frac{q_i q_j e^2}{r_{ij}} \right\}$$

combination rule:

$$\sigma_{ij} = \frac{\sigma_{ii} + \sigma_{jj}}{2} \qquad \epsilon_{ij} = \sqrt{\epsilon_{ii}\epsilon_{jj}}$$

A Model for poly(methyl methacrylate) (PMMA)

The PMMA model is taken from OPLS-AA force field, although the partial charges and bonded parameters for PMMA were adopted from the model proposed by Maranas. [2] To allow the connectivity between the subunits and simultaneously maintain zero charge for each of these subunits, we made the following change. The partial charge of Cα of the first and last residue was changed from 0.00 to -0.045. No variations were applied to the partial charges of the repeating residues. The resulting model is displayed in Figure A III.26 and the non-bonded interactions are specified in Table A III.18. The LJ parameters were taken from the OPLS-AA force field. Bond, angle and dihedral parameters, proposed by Maranas [2] are employed in this study and are shown in the Table A III.19, A III.20 and A III.21, respectively.

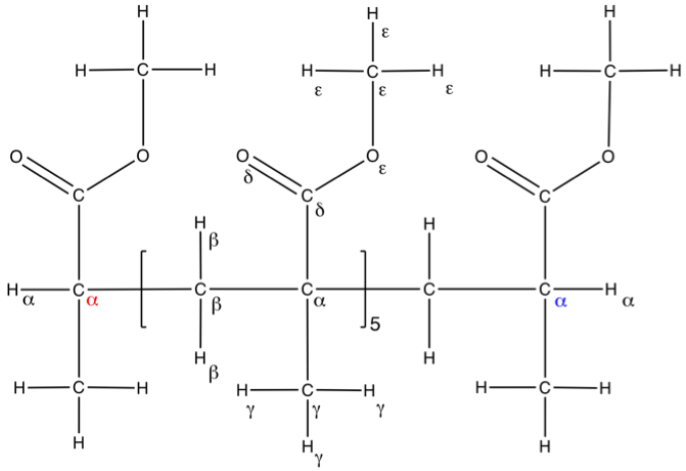

Figure A III.26: The chemical structure of PMMA polymer with the different atom types.

Atom Type	q [e]	σ [nm]	ε [kJ mol^{-1}]
Cγ	-0.135	0.350	0.276
Cα, Cα, terminal	-0.045	0.350	0.276
Cα	0.000	0.350	0.276
Cβ	-0.090	0.350	0.276
Cδ	0.510	0.375	0.439
Oδ	-0.430	0.296	0.879
Oε	-0.330	0.300	0.711
Cε	0.160	0.350	0.276
Hγ, Hα, Hβ	0.045	0.250	0.126
Hε	0.030	0.250	0.126

Table A III.18: Partial charges and LJ parameters for PMMA model.

Bond Type	r_o [nm]	K_{bond} [kJ mol^{-1}nm^{-2}]
Cγ-Hγ	0.10900	138490.4
Cγ-Cα	0.15390	153971.2
Cα-Hα	0.10900	138490.4
Cα-Cβ	0.15491	125520.0
Cβ-Hβ	0.10900	138490.4
Cα-Cδ	0.15710	136398.4
Cδ-Oδ	0.12290	405011.2
Cδ-Oε	0.13600	197066.4
Cε-Oε	0.14460	143092.8
Cε-Hε	0.10900	138490.4

Table A III.19: Bond vibration parameters of PMMA polymer.

Angle Type	θ_0 [deg]	K_{angle} [kJ mol^{-1} rad^{-2}]
Hγ-Cγ-Hγ	109.50	146.4400
Hγ-Cγ-Cα	109.50	146.4400
Cγ-Cα-Cβ	109.47	367.7736
Cγ-Cα-Cδ	109.47	367.7736
Cα-Cδ-Oδ	125.60	264.8472
Cα-Cδ-Oε	111.40	311.7080
Hβ-Cβ-Cα	109.50	146.4400
Hβ-Cβ-Hβ	109.50	146.4400
Oδ-Cδ-Oε	123.00	529.2760
Cδ-Oε-Cε	116.40	354.8032
Hε-Cε-Oε	110.10	243.3040
Hε-Cε-Hε	109.50	146.4400
Cα-Cβ-Cα	113.30	374.4680

Table A III.20: Angle bending parameters of PMMA.

Dihedral Type	C_0 [kJ mol^{-1}]	C_1 [kJ mol^{-1}]	C_2 [kJ mol^{-1}]	C_3 [kJ mol^{-1}]	C_4 [kJ mol^{-1}]	C_5 [kJ mol^{-1}]
Cγ-Cα-Cδ-Oδ	0.31380	-21.4430	-0.20920	21.3384	0.00000	0.00000
Cβ-Cα-Cδ-Oδ	0.31380	-21.4430	-0.20920	21.3384	0.00000	0.00000
Cγ-Cα-Cδ-Oε	1.69000	-1.69000	-13.52001	0.00000	13.52001	0.00000
Cβ-Cα-Cδ-Oε	1.69000	-1.69000	-13.52001	0.00000	13.52001	0.00000
Cε-Oε-Cδ-Cα	1.50624	0.16736	-1.17152	-5.85760	5.35552	0.00000
Cγ-Cα-Cβ-Cα	0.58141	-0.58141	-4.65127	0.00000	4.65127	0.00000
Cδ-Cα-Cβ-Cα	0.58141	-0.58141	-4.65127	0.00000	4.65127	0.00000

Table A III.21: Ryckaert-Bellemans dihedral angle parameters of PMMA.

A Model for poly(2-aminoethyl methacrylate) (PEAM)

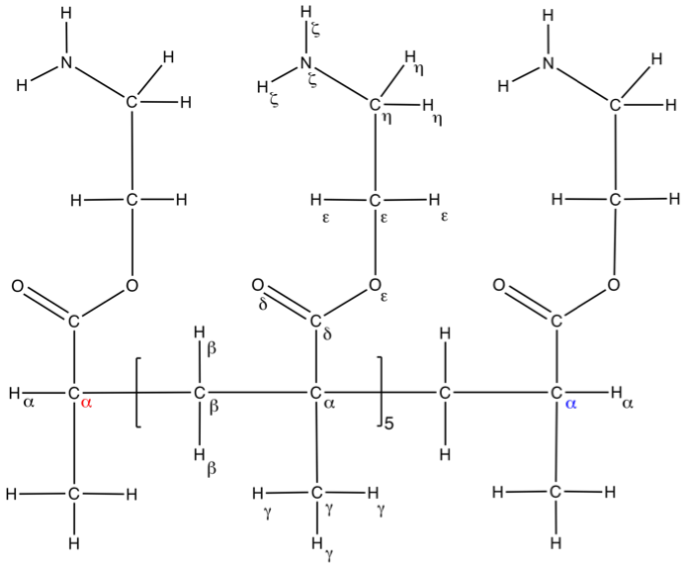

Figure A III.27: The model for PEAM polymer is based on the OPLS-AA force field. The partial charges and bonded parameters for the atoms which are part of the methylene methacrylate group, are taken from the PMMA Maranas [2] model. These interaction terms are detailed in Table A III.22, A III.23, A III.24 and A III.25. Bonded interactions that were not included for all-atom description were adopted from the corresponding interactions of the OPLS-AA force field.

Atom Type	q [e]	σ [nm]	ε [kJ mol^{-1}]
Cγ	-0.135	0.350	0.276
Cα, Cα, terminal	-0.045	0.350	0.276
Cα	0.000	0.350	0.276
Cβ	-0.090	0.350	0.276
Cδ	0.510	0.375	0.439
Oδ	-0.430	0.296	0.879
Oε	-0.330	0.300	0.711
Cε	0.190	0.350	0.276
Cη	0.060	0.350	0.276
Nζ	-0.900	0.330	0.711
Hγ, Hα, Hβ	0.045	0.250	0.126
Hε	0.030	0.250	0.126
Hη	0.060	0.250	0.628
Hζ	0.360	0.000	0.000

Table A III.22: Partial charges and LJ parameters for PEAM. To maintain zero charge in each subunit, the partial charge of C_ε was changed from 0.160 to 0.190, and that of C_α of the first and last residue was changed from 0.00 to -0.045.

Bond Type	r_0 [nm]	K_{bond} [kJ mol^{-1}nm^{-2}]
Cγ-Hγ	0.10900	138490.4
Cγ-Cα	0.15390	153971.2
Cα-Hα	0.10900	138490.4
Cα-Cβ	0.15491	125520.0
Cβ-Hβ	0.10900	138490.4
Cα-Cδ	0.15710	136398.4
Cδ-Oδ	0.12290	405011.2
Cδ-Oε	0.13600	197066.4
Cε-Oε	0.14460	143092.8
Cε-Hε	0.10900	138490.4

Table A III.23: Bond vibration parameters of PEAM polymer.

Angle Type	θ_0 [deg]	K_{angle} [kJ mol^{-1} rad^{-2}]
Hγ-Cγ-Hγ	109.50	146.4400
Hγ-Cγ-Cα	109.50	146.4400
Cγ-Cα-Cβ	109.47	367.7736
Cγ-Cα-Cδ	109.47	367.7736
Cα-Cδ-Oδ	125.60	264.8472
Cα-Cδ-Oε	111.40	311.7080
Hβ-Cβ-Cα	109.50	146.4400
Hβ-Cβ-Hβ	109.50	146.4400
Oδ-Cδ-Oε	123.00	529.2760
Cδ-Oε-Cε	116.40	354.8032
Hε-Cε-Oε	110.10	243.3040
Hε-Cε-Hε	109.50	146.4400
Cα-Cβ-Cα	113.30	374.4680

Table A III.24: Angle bending parameters of PEAM.

Dihedral Type	C_0 [kJ mol^{-1}]	C_1 [kJ mol^{-1}]	C_2 [kJ mol^{-1}]	C_3 [kJ mol^{-1}]	C_4 [kJ mol^{-1}]	C_5 [kJ mol^{-1}]
Cγ-Cα-Cδ-Oδ	0.31380	-21.4430	-0.20920	21.3384	0.00000	0.00000
Cβ-Cα-Cδ-Oδ	0.31380	-21.4430	-0.20920	21.3384	0.00000	0.00000
Cγ-Cα-Cδ-Oε	1.69000	-1.69000	-13.52001	0.00000	13.52001	0.00000
Cβ-Cα-Cδ-Oε	1.69000	-1.69000	-13.52001	0.00000	13.52001	0.00000
Cε-Oε-Cδ-Cα	1.50624	0.16736	-1.17152	-5.85760	5.35552	0.00000
Cγ-Cα-Cβ-Cα	0.58141	-0.58141	-4.65127	0.00000	4.65127	0.00000
Cδ-Cα-Cβ-Cα	0.58141	-0.58141	-4.65127	0.00000	4.65127	0.00000
Nλ-Cη-Cε-Oε	16.73600	-16.73600	0.00000	0.00000	0.00000	0.00000

Table A III.25: Dihedral angles of PEAM polymer.

A Model for poly(3-diamin-(aminomethyl)propyl methacrylate) (DAPM)

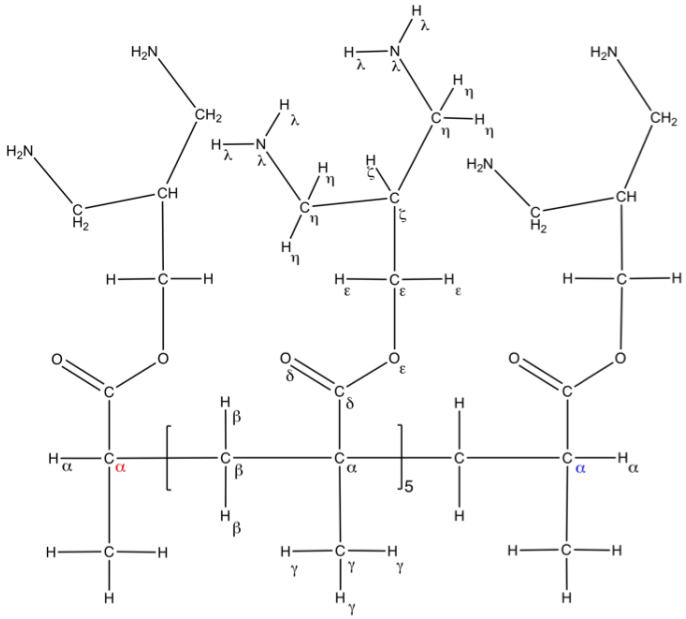

Figure A III.28: The model for DAPM polymer based on the OPLS-AA force field. The partial charges and bonded parameters for the atoms of the methylene methacrylate group are taken from the model of Maranas. [2] These parameters are shown in Table A III.26, A III.27, A III.28 and A III.29. Bonded interactions not present for all-atom description were taken from the corresponding interactions of the OPLS-AA force field.

Atom Type	q [e]	σ [nm]	ε [kJ mol^{-1}]
Cγ	-0.135	0.350	0.276
Cα, Cα, terminal	-0.045	0.350	0.276
Cα	0.000	0.350	0.276
Cβ	-0.090	0.350	0.276
Cδ	0.510	0.375	0.439
Oδ	-0.430	0.296	0.879
Oε	-0.330	0.300	0.711
Cε	0.190	0.350	0.276
Cζ	-0.060	0.350	0.276
Cη	0.060	0.350	0.276
Nλ	-0.900	0.330	0.711
Hγ, Hα, Hβ	0.045	0.250	0.126
Hε	0.030	0.250	0.126
Hζ	0.060	0.250	0.126
Hη	0.060	0.250	0.063
Hλ	0.360	0.000	0.000

Table A III.26: Partial charges and LJ parameters for DAPM. To maintain zero charge in each subunit, the partial charge of C_ε was changed from 0.160 to 0.190, and that of C_α of the first and last residue was changed from 0.00 to -0.045. Nonbonded parameters are taken from OPLS-AA force field.

Bond Type	r_0 [nm]	K_{bond} [kJ $mol^{-1}nm^{-2}$]
Cγ-Hγ	0.10900	138490.4
Cγ-Cα	0.15390	153971.2
Cα-Hα	0.10900	138490.4
Cα-Cβ	0.15491	125520.0
Cβ-Hβ	0.10900	138490.4
Cα-Cδ	0.15710	136398.4
Cδ-Oδ	0.12290	405011.2
Cδ-Oε	0.13600	197066.4
Cε-Oε	0.14460	143092.8
Cε-Hε	0.10900	138490.4

Table A III.27: Bond vibration parameters of DAPM polymer.

Angle Type	θ_0 [deg]	K_{angle} [kJ mol^{-1} rad^{-2}]
Hγ-Cγ-Hγ	109.50	146.4400
Hγ-Cγ-Cα	109.50	146.4400
Cγ-Cα-Cβ	109.47	367.7736
Cγ-Cα-Cδ	109.47	367.7736
Cα-Cδ-Oδ	125.60	264.8472
Cα-Cδ-Oε	111.40	311.7080
Hβ-Cβ-Cα	109.50	146.4400
Hβ-Cβ-Hβ	109.50	146.4400
Oδ-Cδ-Oε	123.00	529.2760
Cδ-Oε-Cε	116.40	354.8032
Hε-Cε-Oε	110.10	243.3040
Hε-Cε-Hε	109.50	146.4400
Cα-Cβ-Cα	113.30	374.4680

Table A III.28: Angle bending parameters of DAPM polymer.

Dihedral Type	**C_0** [kJ mol^{-1}]	**C_1** [kJ mol^{-1}]	**C_2** [kJ mol^{-1}]	**C_3** [kJ mol^{-1}]	**C_4** [kJ mol^{-1}]	**C_5** [kJ mol^{-1}]
Cγ-Cα-Cδ-Oδ	0.31380	-21.4430	-0.20920	21.3384	0.00000	0.00000
Cβ-Cα-Cδ-Oδ	0.31380	-21.4430	-0.20920	21.3384	0.00000	0.00000
Cγ-Cα-Cδ-Oε	1.69000	-1.69000	-13.52001	0.00000	13.52001	0.00000
Cβ-Cα-Cδ-Oε	1.69000	-1.69000	-13.52001	0.00000	13.52001	0.00000
Cε-Oε-Cδ-Cα	1.50624	0.16736	-1.17152	-5.85760	5.35552	0.00000
Cγ-Cα-Cβ-Cα	0.58141	-0.58141	-4.65127	0.00000	4.65127	0.00000
Cδ-Cα-Cβ-Cα	0.58141	-0.58141	-4.65127	0.00000	4.65127	0.00000

Table A III.29: Dihedral angle parameters of DAPM polymer.

A Model for poly(aniline methacrylamide) (PAAM)

The PAAM model was taken from OPLS-AA force field. The partial charges and bonded parameters for C_γ, C_α, C_β, and H_γ, H_α, H_β were adopted from the model proposed for PMMA [2] polymer, as well as for the bonded parameters for C_δ-O_δ atom types. The LJ parameters were taken from the OPLS-AA force field. Dihedral parameters for C_δ-N_ε-C_ζ-C_η, C_η-C_ζ-N_ε-H_ε, C_λ-C_μ-N_υ-H_υ angles are taken from Jorgensen et al. [3] parametrization. The Improper dihedrals terms derived from OPLS-AA force field. The sum of the charges for each subunit is zero; therefore, the partial charge of C_α of the first and last residue was changed from 0.00 to -0.045. Bonded interactions that were not detailed for all-atom description were taken from the corresponding interactions of the OPLS-AA force field. The resulting model is displayed in Figure A III.29. The partial charge and nonbonded parameters are shown in Table A III.30. Bond, angle, dihedral and improper dihedral parameters, are detailed in the Table A III.31, A III.32, A III.33, A III.34, respectively.

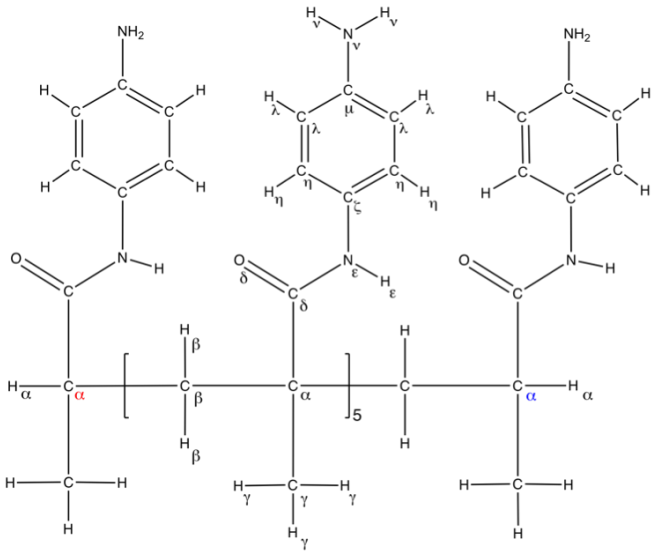

Figure A III.29: The chemical structure of PAAM polymer with the different atom types.

Atom Type	**q** [e]	**σ** [nm]	**ε** [kJ mol^{-1}]
Cγ	-0.135	0.350	0.276
Cα, Cα, terminal	-0.045	0.350	0.276
Cα	0.000	0.350	0.276
Cβ	-0.090	0.350	0.276
Cδ	0.500	0.375	0.439
Oδ	-0.500	0.296	0.879
Nε	-0.500	0.325	0.711
Cζ	0.200	0.355	0.293
Cη	-0.115	0.355	0.293
Cλ	-0.115	0.355	0.293
Cμ	0.180	0.355	0.293
Nν	-0.900	0.330	0.711
Hγ, Hα, Hβ	0.045	0.250	0.126
Hε	0.300	0.000	0.000
Hη, Hλ	0.115	0.355	0.293
Hν	0.360	0.000	0.000

Table A III.30: Partial charges and LJ parameters of PAAM polymer.

Bond Type	**r_0** [nm]	**K_{bond}** [kJ mol^{-1}nm^{-2}]
Cγ-Hγ	0.10900	138490.4
Cγ-Cα	0.15390	153971.2
Cα-Hα	0.10900	138490.4
Cα-Cβ	0.15491	125520.0
Cβ-Hβ	0.10900	138490.4
Cα-Cδ	0.15710	136398.4
Cδ-Oδ	0.12290	405011.2

Table A III.31: Bond vibration parameters of PAAM polymer.

Angle Type	θ_0 [deg]	K_{angle} [kJ mol^{-1} rad^{-2}]
Hγ-Cγ-Hγ	109.50	146.4400
Hγ-Cγ-Cα	109.50	146.4400
Cγ-Cα-Cβ	109.47	367.7736
Cγ-Cα-Cδ	109.47	367.7736
Cα-Cδ-Oδ	125.60	264.8472
Hβ-Cβ-Cα	109.50	146.4400
Hβ-Cβ-Hβ	109.50	146.4400
Cα-Cβ-Cα	113.30	374.4680

Table A III.32: Angle bending parameters of PAAM polymer.

Dihedral Type	C_0 [kJ mol^{-1}]	C_1 [kJ mol^{-1}]	C_2 [kJ mol^{-1}]	C_3 [kJ mol^{-1}]	C_4 [kJ mol^{-1}]	C_5 [kJ mol^{-1}]
Cγ-Cα-Cδ-Oδ	0.31380	-21.4430	-0.20920	21.3384	0.00000	0.00000
Cβ-Cα-Cδ-Oδ	0.31380	-21.4430	-0.20920	21.3384	0.00000	0.00000
Cγ-Cα-Cβ-Cα	0.58141	-0.58141	-4.65127	0.00000	4.65127	0.00000
Cδ-Cα-Cβ-Cα	0.58141	-0.58141	-4.65127	0.00000	4.65127	0.00000
Cδ-Nε-Cζ-Cη	1.23900	8.58800	-3.43100	-6.39600	0.00000	0.00000
Cη-Cζ-Nε-Hε	2.03000	0.00000	-2.03000	0.00000	0.00000	0.00000
Cλ-Cμ-Nν-Hν	2.03000	0.00000	-2.03000	0.00000	0.00000	0.00000

Table A III.33: Dihedral angle parameters of PAAM polymer.

Improper Type	ϕ_s [deg]	K_ϕ [kJ mol^{-1}]
Cη-Cζ-Cη-Nε	180.0	4.60240
Cζ-Cη-Cλ-Hη	180.0	4.60240
Cη-Cλ-Cμ-Nλ	180.0	4.60240
Cλ-Cμ-Cλ-Hμ	180.0	4.60240
Cμ-Cλ-Cη-Nλ	180.0	4.60240
Cλ-Cη-Cζ-Hη	180.0	4.60240

Table A III.34: Improper dihedral angle parameters of PAAM polymer.

A Model for poly(N-(3,5-diaminophenyl)methacrylamide) (PDAFMA)

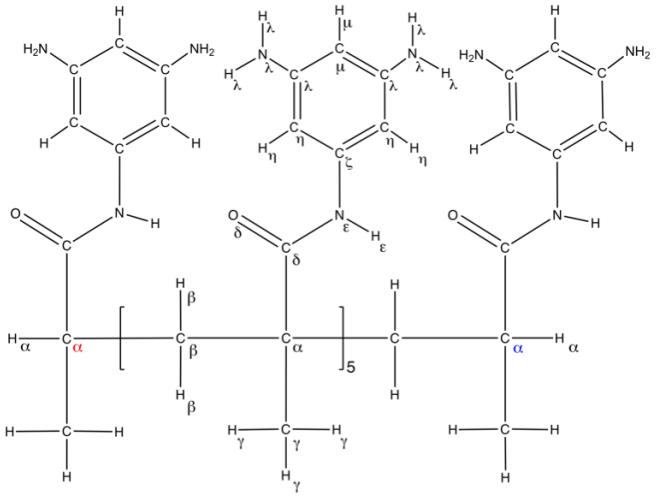

Figure A III.30: The chemical structure of PDAFMA polymer with the different atom types. The PDAFMA model was taken from OPLS-AA force field.

Atom Type	**q** [e]	**σ** [nm]	**ε** [kJ mol^{-1}]
Cγ	-0.135	0.350	0.276
Cα, Cα, terminal	-0.045	0.350	0.276
Cα	0.000	0.350	0.276
Cβ	-0.090	0.350	0.276
Cδ	0.500	0.375	0.439
Oδ	-0.500	0.296	0.879
Nε	-0.500	0.325	0.711
Cζ	0.200	0.355	0.293
Cη	-0.115	0.355	0.293
Cλ	0.180	0.355	0.293
Nλ	-0.900	0.330	0.711
Cμ	-0.115	0.355	0.293
Hγ, Hα, Hβ	0.045	0.250	0.126
Hε	0.300	0.000	0.000
Hη, Hμ	0.115	0.242	0.126
Hλ	0.360	0.000	0.000

Table A III.35: Partial charges and LJ parameters of PDAFMA polymer. The partial charges and bonded parameters for C_γ, C_α, C_β, and H_γ, H_α, C_β were adopted from the model proposed by Maranas. [2] This model was also used to define the bonded parameters for C_δ and $O_\delta$atoms. To maintain zero charges for each subunit, the partial charge of C_α of the first and last residue was changed from 0.00 to -0.045. The LJ parameters were taken from the OPLS-AA force field.

Bonded interactions that were not specified for all-atom description were taken from the corresponding interactions of the OPLS-AA force field.

Bond Type	r_0 [nm]	K_{bond} [kJ $mol^{-1}nm^{-2}$]
Cγ-Hγ	0.10900	138490.4
Cγ-Cα	0.15390	153971.2
Cα-Hα	0.10900	138490.4
Cα-Cβ	0.15491	125520.0
Cβ-Hβ	0.10900	138490.4
Cα-Cδ	0.15710	136398.4
Cδ-Oδ	0.12290	405011.2

Table A III.36: Bond vibration parameters of PDAFMA polymer.

Angle Type	θ_0 [deg]	K_{angle} [kJ mol^{-1} rad^{-2}]
Hγ-Cγ-Hγ	109.50	146.4400
Hγ-Cγ-Cα	109.50	146.4400
Cγ-Cα-Cβ	109.47	367.7736
Cγ-Cα-Cδ	109.47	367.7736
Cα-Cδ-Oδ	125.60	264.8472
Hβ-Cβ-Cα	109.50	146.4400
Hβ-Cβ-Hβ	109.50	146.4400
Cα-Cβ-Cα	113.30	374.4680

Table A III.37: Angle bending parameters of PDAFMA polymer.

Dihedral Type	C_0 [kJ mol^{-1}]	C_1 [kJ mol^{-1}]	C_2 [kJ mol^{-1}]	C_3 [kJ mol^{-1}]	C_4 [kJ mol^{-1}]	C_5 [kJ mol^{-1}]
Cγ-Cα-Cδ-Oδ	0.31380	-21.4430	-0.20920	21.3384	0.00000	0.00000
Cβ-Cα-Cδ-Oδ	0.31380	-21.4430	-0.20920	21.3384	0.00000	0.00000
Cγ-Cα-Cβ-Cα	0.58141	-0.58141	-4.65127	0.00000	4.65127	0.00000
Cδ-Cα-Cβ-Cα	0.58141	-0.58141	-4.65127	0.00000	4.65127	0.00000
Cδ-Nε-Cζ-Cη	1.23900	8.58800	-3.43100	-6.39600	0.00000	0.00000
Cη-Cζ-Nε-Hε	2.03000	0.00000	-2.03000	0.00000	0.00000	0.00000
Cμ-Cλ-Nλ-Hλ	2.03000	0.00000	-2.03000	0.00000	0.00000	0.00000
Cη-Cλ-Nλ-Hλ	2.03000	0.00000	-2.03000	0.00000	0.00000	0.00000

Table A III.38: Dihedral angle parameters of PDAFMA polymer. The parameters for C_δ-N_ε-C_ζ-C_η, C_η-C_ζ-N_ε-H_ε, C_μ-C_λ-N_λ-H_λ and C_η-C_λ-N_λ-H_λ angle, are taken from Jorgensen et al. [3] parametrization.

Improper Type	ϕ_s [deg]	K_ϕ [kJ mol^{-1}]
Cη-Cζ-Cη-Nε	180.0	4.60240
Cζ-Cη-Cλ-Hη	180.0	4.60240
Cη-Cλ-Cμ-Hλ	180.0	4.60240
Cλ-Cμ-Cλ-Nv	180.0	4.60240
Cμ-Cλ-Cη-Hλ	180.0	4.60240

Table A III.39: Improper dihedral angle parameters of PDAFMA polymer. The terms derive from OPLS-AA force field.

References

[1] Atkins, P. W.; de Paula, J. *Physical Chemistry;* Oxford University Press: Oxford, UK, seventh edition ed., 2002.

[2] Chen, C.; Maranas, J. K.; García-Sakai, V. Local dynamics of syndiotactic poly (methyl methacrylate) using molecular dynamics simulation, *Macromolecules* 2006, *39*(26), 9630–9640.

[3] Rizzo, R. C.; Jorgensen, W. L. OPLS All-Atom Model for Amines:Resolution of the Amine Hydration Problem, *J. Am. Chem. Soc.* 1999, *121*, 4827–4836.

List of Abbreviations and acronyms

- **^{1}H-NMR** proton-Nuclear Magnetic Resonance
- **2D** Two-Dimensional
- **3D** Three-Dimensional
- **CCS** CO_2 Capture and Storage
- **CMC** Critical Micelle Concentration
- **COFs** Covalent organic frameworks
- **DAPM** poly(3-Diamin-(Aminomethyl)Propyl Methacrylate)
- **EP** Emulsion Polymerization
- **G** Graphene
- **GP** Graphene-Polymer
- **GROMACS** GROningen MAchine for Chemical Simulations
- **HB** Hydrogen Bond
- **LINCS** Linear Constraint Solver
- **MD** Molecular Dynamics

- **MOFs** Metal-Organic Frameworks
- **NC** Coordination Number
- **NPT** Isothermal-isobaric (ensemble)
- **NVE** Microcanonical (ensemble)
- **NVT** Canonical (ensemble)
- **OCA** Optical Contact Angle
- **OPLS-AA** Optimized Potentials for Liquid Simulations (All Atoms)
- **PAAM** Poly(Anline) MethacrylAmide
- **PBC** Periodic Boundary Condition
- **PDAFMA** Poly(N-(3,5-Diaminophenyl)MethacrylAmide
- **PE** Poly(Ethylene)
- **PEAM** Poly(2-AminoEthyl Methacrylatre)
- **PEO** Poly(Ethylene-Oxide)
- **PEO-PE** Poly(Ethylene-Oxide)-Poly(Ethylene)
- **PME** Particle Mesh Ewald
- **PMF** Potential of Mean Force
- **PMMA** Poly(Methyl Methacrylate)
- **PS** Poly(Styrene)
- **QCM-D** Quartz Crystal Microbalance with Dissipation monitoring

- **RDF** Radial Distribution Function
- **RDF** Radial Distribution Functions
- **S** Styrene
- **SDS** Sodium Dodecyl Sulfate
- **SEM** Scanning Electron Microscopy
- **com** center of mass
- **o/w** oil in water
- **o/w/o** oil/water/oil
- **w/o** water in oil
- **w/o/w** water/oil/water